Dissertation
submitted to the
Combined Faculties for the Natural Sciences and for Mathematics
of the Ruperto-Carola University of Heidelberg, Germany
for the degree of
Doctor of Natural Sciences

presented by

Oana-Daniela Toader, M.Sc.
born in Târnăveni, Romania

Oral-examination:

Genetic approaches to probe spatial coding in the medial entorhinal cortex

Referees: Prof. Dr. Hannah Monyer
Prof. Dr. Stephan Frings

Declarations according to § 8 (3) b) and c) of the doctoral degree regulations: a) I hereby declare that I have written the submitted dissertation myself and in this process have used no other sources or materials than those expressly indicated, b) I hereby declare that I have not applied to be examined at any other institution, nor have I used the dissertation in this or any other form at any other institution as an examination paper, nor submitted it to any other faculty as a dissertation.

Heidelberg, _____

Contents

Summary

The medial entorhinal cortex is a key component of the brain's spatial navigation and memory system. It is the site where grid cells were discovered, i.e. neurons that are active at several locations in an environment, thus giving rise to a hexagonal 'grid'-like firing pattern. Experimental evidence suggests that inputs from the hippocampus, medial septum, and other brain regions, together with specific local connectivity are factors that contribute to the emergence of the grid cell pattern.

To date, it is not clear how the hippocampus, which is also involved in spatial behaviors and projects to the MEC, contributes to grid cell function. I addressed this question by recording grid cells in mice with impaired hippocampal function. My results suggest that impaired spatial hippocampal coding does not disrupt grid cell firing. Furthermore, I gathered evidence that the MEC, as opposed to the hippocampus, is required for path integration.

To probe how specific MEC neurons support spatial behavior, we need tools to manipulate them selectively. To this end, molecular markers must be identified and assigned to functional cell types. Two promising candidates are reelin (RE) and calbindin (CB). These proteins are expressed in anatomically distinct cell types. While *in vitro* these neurons are distinct with respect to their electrophysiological properties, it is still unclear how these differences correlate to *in vivo* firing patterns. I addressed this question by using two mouse lines to optogenetically tag RE^+ and CB^+ neurons. I find no major difference between the two populations, except for the pattern of projections to other brain regions. Also, I reveal the existence of a previously unknown projection from the parasubiculum to the contralateral MEC, that, along with pyramidal CB^+ neuron projections, appear to inhibit the contralateral MEC. These results suggest that the firing patterns of RE^+ and CB^+ cells are surprisingly similar, and that these markers may be valuable tools for studying components of cross-hemispheric connections.

Zusammenfassung

Der mediale entorhinale Kortex (MEC) ist eine Gehirnstruktur welche eine Schlüsselrolle für die räumliche Wahrnehmung und das Gedächtnis spielt. Hier wurden Gitterzellen entdeckt, Neurone die an multiplen Positionen im Raum aktiviert werden und deren Aktivität ein hexagonales Muster bildet. Experimente deuten darauf hin, dass afferente Signale aus dem Hippokampus (HP), Medialen Septum und anderen Hirnregionen, zusammen mit lokaler Konnektivität, Faktoren sind, welche in die Entstehung des Gittermusters involviert sind.

Bislang ist es nicht bekannt wie der HP, welcher eine Rolle beim räumlichem Verhalten spielt, die Funktion der Gitterzellen beeinflusst. Ich habe diese Fragestellung bearbeitet, indem ich die Gitterzellaktivität in Mäusen mit gestörter HP Funktion untersucht habe. Meine Daten verdeutlichen, dass eine verminderte räumliche hippokampale Kodierung die Aktivität der Gitterzellen nicht beeinträchtigt. Meine Daten zeigen außerdem, dass der MEC, im Gegensatz zu dem HP, für *path integration* notwendig ist.

Um die Funktion bestimmter MEC Zellen manipulieren zu können, brauchen wir Marker die spezifische funktionalen Zellklassen angehören. Zwei solche Marker sind reelin (RE) und calbindin (CB). Diese sind in anatomisch unterschiedlichen Neuronen exprimiert und lassen sich anhand ihrer elektrophysiologischen Eigenschaften in mehrere Klassen aufteilen. Dennoch, ist es bisher nicht bekannt wie diese Eigenschaften der *in vivo* Funktion entsprechen. Um diese Fragestellung zu beantworten, habe ich zwei gefloxte Mauslinien verwendet, bei welchen die RE^+ und CB^+ Neurone anhand Laser-Aktivierung identifiziert werden können. In meiner Arbeit kann ich keine nennenswerte Unterschiede zwischen den beiden Populationen feststellen, obgleich ihre jeweiligen Projektionen divergieren. Außerdem, habe ich eine bislang unbekannte Projektion zum kontralateralem MEC entdeckt, welche, zusammen mit der bereits untersuchten CB^+ Projektion, die Neurone in der kontralateralen Hirnhemisphäre inhibiert.

Chapter I - Cellular substrates of spatial orientation and memory

Animals belonging to various phyla need to navigate through space in a purposeful manner. Tasks like returning to the nest or borrow after foraging require them to either use landmarks as reference points, like tall buildings or trees, or integrate the movements of their own body to calculate a virtual return vector. These actions are not trivial, since they possibly require switching between different strategies of orientation depending on the availability of external cues. Path integration is the navigational strategy which is used preferentially when external cues are scarce or unreliable (Mittelstaedt and Mittelstaedt, 1980; Etienne and Jeffery, 2004), and is probably particularly important for nocturnal animals like rodents.

For a long time, it was not clear how and where the brain encodes information regarding spatial navigation. In desert ants it was shown, for example, that path integration relies on processing signals from proprioceptors in the leg joints. These insects are capable of returning to their nest in an almost perfectly straight line after traveling long circuitous distances of tens of meters through the desert (thus lacking landmarks and olfactory cues, due to constant wind) in darkness, and even after being under narcosis for several hours (therefore not relying on polarized light either) (Sommer and Wehner, 2004). The experimenters managed to disturb the return path by adding stilts or shortening the ants' legs (Wittlinger et al., 2007). In mammals, a similar ability relies on a complex of systems, including the proprioceptive, vestibular and visual system. The information provided by these sensory modalities is thought to be integrated in the hippocampal formation and adjacent brain regions and translated into an internal map of the environment (Navratilova and McNaughton, 2014).

Key observations regarding the function of the hippocampus were made in the second half of the 20th century. The sustained effort of surgeons and psychologists who carefully mapped lesions of patients with partial or total lobectomy

(used at the time as a last resort treatment for intractable epilepsy, schizophrenia or depression), and injured subjects (from work accidents or war wounds) led to new insights into the function of specific brain regions. Anatomical findings were correlated with a wide range of behavioral test results (Milner, 1965). Humans with a damaged hippocampus had various degrees of memory deficits, with the degree of impairment proportional to the size of the lesion (Scoville and Milner, 1957; Petrides, 1985). The dramatic case of Henry Molaison (the famous H.M. patient) who displayed very unexpected symptoms after a bilateral resection of both hippocampi in order to treat his epilepsy, showed that new memories could not be acquired without this part of the brain (anterograde amnesia), and recent episodic memories were largely lost (retrograde amnesia). Also, the patient was confused and could not find his way around the house or in the town where he lived. These findings led scientists to hypothesize that spatial and declarative memory rely on the function of the hippocampus (Cohen and Squire, 1980; O'Keefe and Nadel, 1987). Recent postmortem histological analysis of Henry Molaison's brain showed that in fact the posterior hippocampus was spared by the resection, and in turn the entorhinal cortex was almost completely excised (Annese et al., 2014).

1 Place cells

In the search for functional neural correlates of spatial memory and orientation, O'Keefe and Dostrovsky (O'Keefe and Dostrovsky, 1971) adapted a recording technique previously used to record in the spinal cord. They inserted electrodes in the hippocampus of behaving rats and found neurons in the Cornu Ammonis region 1 (CA1) that became active when the animal was at a specific place in the recording environment, and were otherwise silent. These neurons were termed 'place cells' (Figure 1 A, B). Each place cell had its specific region where it became active and therefore the population activity in a given environment could aid in identifying the position of the rat with high precision (O'Keefe and Speakman, 1987; Muller et al., 1987). In a new environment a given place cell might change place field position, its firing rate or stay silent (Lu et al., 2013). The cell populations that fire in different environments are orthogonal to (independent of) each other, i.e. it is impossible to predict if and where a certain place cell will be active in a new environment (Leutgeb et al., 2004). The fact that a unique set of cells

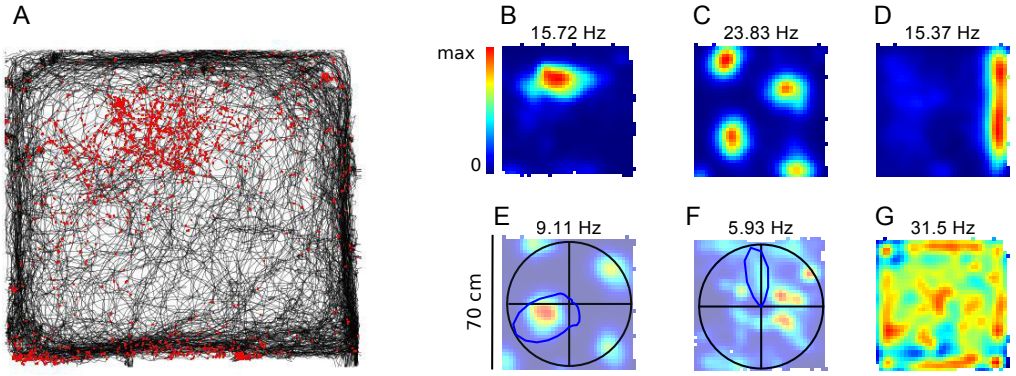

Figure 1. Functional cell types in the hippocampus and MEC. A, Running path (black line) of a mouse foraging for food in a square (70x70x30 cm) box and superimposed spikes (red dots) of a place cell. Color-coded firing rate maps of the same place cell shown in **A** (**B**),and of a grid cell (**C**), border cell (**D**), conjunctive cell (**E**), HD cell (**F**) and interneuron (**G**) recorded in the MEC. Numbers on top of each map indicate the maximum firing rate of that cell. Polar plots in **E** and **F** depict the firing rate as a function of the head direction in respect to box. Unpublished data.

with a unique set of place field locations is active in each environment led some scientists to theorize that the hippocampus creates and stores a 'cognitive map' of the outside world (O'Keefe and Nadel, 1987; Muller et al., 1987; Bostock et al., 1991; Colgin et al., 2008; Buzsáki and Moser, 2013). It is thought that this orthogonalization is essential for retaining distinct memories of environments even when the differences between them are minimal.

2 Head direction cells

Another breakthrough in the field of spatially tuned neurons was the discovery of cells that encode head direction (Figure 1 F), first in the postsubiculum (Taube et al., 1990b,a), and later in the anterior thalamus (Blair and Sharp, 1995), parasubiculum (Boccara et al., 2010), MEC (Sargolini et al., 2006) and many other brain regions (Chen et al., 1994; Stackman and Taube, 1998; Blair et al., 1998; Cho and Sharp, 2001; Sharp et al., 2001; Tsanov et al., 2011). These neurons become highly active when the animal faces a particular direction (measured on an imaginary circle, whose center is the animal's head). Head direction cells can be disturbed by damaging the inner ear (Valerio and Taube, 2016). They have a striking population property: in whatever environment the animal is placed, the

relative phases of HD cells remains unchanged.

3 Grid cells

Path integration is thought to contribute to the place field code, but it appears that some path integration tasks can be performed by hippocampectomized rats, while others not (Maaswinkel et al., 1999; Alyan and McNaughton, 1999). These findings suggest that the hippocampus could be required for integrating external cues and path integration information originating from another region. A path integrating system should be capable of computing direction and distance traveled. The direction is provided by the head direction system, but apparently the hippocampus is dispensable in some homing tasks. Therefore, it was anticipated that path integration is either performed outside the hippocampus, or it is dependent on several brain regions, including the hippocampus (Touretzky and Redish, 1996). By combining theoretical predictions and anatomical analysis, the group of Edvard and May-Britt Moser decided to study the function of the MEC, a region that receives spatial inputs and is the origin of the major projection to the hippocampus, i.e. the perforant path (van Strien et al., 2009). Their finding was striking: a small proportion (10-20%) of MEC neurons have multiple firing fields that are arranged in an equilateral triangle lattice spanning the entire recording environment (Fyhn et al., 2004; Hafting et al., 2005). Later, these neurons were also found in the pre- and parasubiculum (Boccara et al., 2010) (Figure 1 C). This pattern is highly symmetrical and regular and is expressed quickly in a new environment (Hafting et al., 2005; Barry et al., 2012). It is characterized by several parameters, among which grid score (a number that describes the 60° rotational symmetry), phase (the absolute position in space of the firing fields), orientation (the angle made by a line drawn through 2 firing fields and a reference axis), and spacing (the average distance between firing field centers). Grid cells that are very close to one another (i.e. are recorded on the same tetrode) generally have the same spacing and orientation, but differ in their phase (Hafting et al., 2005). Although the absolute parameter values may vary from one environment to the next, the phase relationships between grid cells remain generally unchanged, similarly to HD neurons. Furthermore, the spacing and size of the fields increases from dorsal to ventral MEC (Stensola et al., 2012), similar to hippocampal place cells (Jung et al., 1994; Maurer et al., 2005; Kjelstrup et al., 2008), and do so in

a discrete manner. There appear to be four or five groups of spacings, ranging from approximately 30 cm to 3 m in rats. The presence of grid cells was so far demonstrated in rats (Hafting et al., 2005), mice (Fyhn et al., 2008), and bats (Yartsev et al., 2011).

4 Other spatially and non-spatially selective neurons

For the purpose of brevity, I will only briefly summarize the additional functional cell types in the MEC. One of these are border cells, neurons that fire along the edges of an environment (Figure 1 D) (Solstad et al., 2008). Detecting the borders of an environment is thought to be crucial for the anchoring of spatial representations to the external world, in the absence of visual cues (Hardcastle et al., 2015). For rodents this is particularly important, since they are nocturnal animals. Conjunctive cells have a combined grid and head-direction phenotype (Figure 1 E). Sparse spatially selective cells fire in confined regions of the recording environment, without displaying any periodical pattern. And last, but not least, a conspicuous neuronal type often found in the MEC are fast-spiking interneurons. They have a low spatial selectivity, fire throughout the recording environment (Figure 1 G), and receive input from many low firing, spatially selective neurons (Couey et al., 2013; Buetfering et al., 2014). Interneurons are thought to be essential for the generation of the grid cell firing pattern, as predicted by computational modeling studies and as suggested by the local connectivity in the MEC (Burak and Fiete, 2009; Pastoll et al., 2012; Couey et al., 2013; Bonnevie et al., 2013; Solanka et al., 2015; Fuchs et al., 2016).

5 Importance of spatially selective neurons

Forty-five years after the discovery of place cells and eleven years after grid cells were found, scientists still do not agree on what the function of these neurons is. It was proposed that MEC grid cells like an empty system of coordinates that can be superimposed on any environment to provide a frame for estimating distance and direction. This information is then combined with other sensory cues in the hippocampus to obtain contextual information and form meaningful

memories (Touretzky and Redish, 1996). An alternative hypothesis is that grid cells are better position estimators than place cells due to their periodic firing fields and modular organization (Mathis et al., 2012), which brings in question the role of place cells. As mentioned before, the hippocampus is indispensable for acquiring episodic memories. One finding that correlates with this feature (in addition to already mentioned patient data) is a phenomenon called replay, that takes place in the hippocampus during periods of rest or sleep (Skaggs and McNaughton, 1996). Essentially, sequences of activated cells observed during locomotion reactivate in the same order during sleep or immobility, but roughly ten times faster (Carr et al., 2011). This phenomenon is thought to be involved in memory consolidation, and is based on the assumption that a place cell does not only encode where the animal is in space at the present moment, but also the memory of that place. Such processes are much more difficult to detect in the MEC, since neurons are not as densely packed as place cells in the hippocampus (i.e. it is difficult to record from a large number of neurons simultaneously, which is a prerequisite for studying population activity). While it is clear that the MEC and the hippocampus are important for a number of spatial behaviors (Morris et al., 1990; Steffenach et al., 2005; Parron et al., 2006; Yasuda and Mayford, 2006; Hales et al., 2014), the role of individual cell types has remained elusive.

6 Inputs relevant for grid cell formation

The striking geometry of the grid pattern made researchers wonder what the mechanisms behind this neuronal activity are. To this aim, two lines of research have emerged: one looking at the influence of other brain areas on grid cell activity, and the other investigating local connectivity between MEC neurons and the intrinsic neuronal properties of neurons. The former, while relying on predictions made by computational studies, can be also successfully investigated in behaving animals, by using pharmacological manipulations and specific lesions. Several studies have shown that disturbing the activity of one in a number of brain regions leads to various alterations in grid cell firing, ranging from a mild decrease in firing field stability to a complete loss of the grid pattern. Among these, the best investigated so far are the hippocampus (Fyhn et al., 2004; Bonnevie et al., 2013), the anterior thalamic nuclei (ATN) (Winter et al., 2015) and the medial septum (MS) (Brandon et al., 2011; Koenig et al., 2011). The second strategy is,

due to the lack of a specific marker for grid cells, mostly possible *in vitro* (Dhillon and Jones, 2000; Kumar et al., 2007; Beed et al., 2010; Quilichini et al., 2010; Varga et al., 2010; Couey et al., 2013; Fuchs et al., 2016) or via computational modeling (Burak and Fiete, 2009; Pastoll et al., 2013), with a few studies using *in vivo* patch-clamping or juxtacellular recordings to identify anatomical and functional characteristics of individual neurons (Burgalossi et al., 2011; Domnisoru et al., 2013; Schmidt-Hieber and Häusser, 2013; Ebbesen et al., 2016). However, optogenetics and calcium indicators are opening up new and exciting possibilities, combining the specificity of mutant mouse lines with the high-throughput capabilities of tetrode or calcium imaging recordings (Zhang et al., 2013; Kitamura et al., 2014; Buetfering et al., 2014; Sun et al., 2015). These data are essential for testing and challenging predictions of computational studies that try to model grid cell pattern emergence (Burak and Fiete, 2009; Couey et al., 2013; Bonnevie et al., 2013).

7 Aim of the study

In the work presented in this dissertation I used both aforementioned strategies to study grid cells and other neurons present in the MEC. In the first project I investigated the activity of grid cells in a mouse model with impaired hippocampal function (*Cx36*$^{-/-}$ mice). I show that hippocampal input with a lower information content does not affect the generation of the hexagonal firing pattern of grid cells. This result extends previous findings that showed that excitatory hippocampal input was necessary for grid cell firing (Bonnevie et al., 2013). In the second project I investigated two major neuronal populations in the MEC, expressing the protein markers CB and RE, respectively (Fujimaru and Kosaka, 1996; Varga et al., 2010). I set out to test differences in the spatio-temporal activity of these two neuronal types, as well as discover the functional identity of post synaptic targets in the ipsi- and contralateral brain hemisphere. I did not find any major difference in the spatial properties of RE^{+} and CB^{+} neurons. Additional details regarding the research background of each project will be provided in the respective introductions.

Chapter II - Materials and Methods

8 Animals

Animals were handled in accordance to procedures approved by the Governmental Supervisory Panel on Animal Experiments of Baden-Württemberg in Karlsruhe (license G-113/10 and G-50/14). Mice were housed in cages with up to 3 animals per cage and had free access to water and food before the beginning of the experiment. Animals for *in vitro* experiments were 4-5 weeks old. Animals for *in vivo* experiments were 3-5 months old and were housed alone over the course of the experiment. The following mouse lines were used: wild-type C57BL/6, $Cx36^{-/-}$ (Hormuzdi et al., 2001), $GAD67^{EGFP}$ (Tamamaki et al., 2003), $Cx36^{EGFP}$, CB^{Cre} (purchased from Taconic Bioscience), and $UchlI^{Cre}$ (obtained from the Mutant Mouse Regional Resource Center).

9 In vitro electrophysiology (performed by Dr. Angela Neitz)

9.1 Preparation of acute brain slices

Mice (4-5 weeks old) were deeply anesthetized by isoflurane inhalation, then decapitated and brains were removed. The control experiments were done using a $GAD67^{EGFP}$ mouse line, that facilitated visual identification of inhibitory neurons. Using a *Slicer HR 2* vibratome (Sigmann Elektronik, Germany), sagital sections 250-300 µm thick were cut in ice-cold sucrose solution containing (in mM) 212 sucrose, 26 mM $NaHCO_3$, 1.25 mM NaH_2PO_4, 3 mM KCl, 0.2 mM $CaCl_2$, 7 mM $MgCl_2$ and 10 mM glucose, oxygenated with carbogen gas (95% O2/5% CO_2, pH 7.4) and stored for 1 hour at room temperature in oxygenated, glucose-based

extracellular solution containing (in mM) 125 NaCl, 25 mM $NaHCO_3$, 1.25 mM NaH_2PO_4, 2.5 mM KCl, 2 mM $CaCl_2$, 1 mM $MgCl_2$ and 25 mM glucose.

9.2 Electrophysiological recordings

Individual sections were placed in a submerged recording chamber mounted onto an upright microscope (Olympus BW-X51) and continuously perfused with oxygenated extracellular solution at 32-34°C. Layer II (LII) fast-spiking (FS) interneurons in the MEC were identified with differential interference contrast (DIC) optics and epifluorescence. Cell pairs with less than 100 µm interneuron distance were patched. Pipettes were pulled from borosilicate glass capillaries and had tip resistances of 3-8 MΩ A high Cl^- containing intracellular solution was used, containing (in mM) 127.5 KCl, 11 EGTA, 10 Hepes, 1 $CaCl_2$, 2 $MgCl_2$ and 2 Mg-ATP (pH 7.3). Cells were discarded if the series resistance changed more than 20% or was higher than 40MΩ . FS interneuron pairs were patched in whole-cell configuration after achieving a Giga-seal and firing patterns were analyzed in current-clamp mode at resting membrane potential by somatic current injection (1s, starting from -150 pA in 20 pA steps until maximal firing frequency was reached). Gap junction coupling was tested in current-clamp mode with hyperpolarizing steps (-400 pA for 300 ms). Recordings were made using either HEKA or PatchMaster EPC 10 amplifier and signals were filtered at 3 kHz and sampled at 20 kHz.

9.3 Analysis of data

Analysis of data was done offline using the HEKA software FitMaster. The coupling coefficient between pairs of FS interneurons was analyzed by using an average of 15 consecutive hyperpolarizing current sweeps and measuring the plateau-phase of the maximal current. The strength of coupling was expressed as the mean coupling coefficient, which was calculated as the ratio between the post- and the pre-synaptic cell response. Both directions of coupling were tested. Two cells were considered coupled if the plateau current exceeded a threshold of 2xsingal/noise. Data are shown as mean ± SEM.

10 In vivo electrophysiology and optogenetics

10.1 Tetrode and optic fiber implantation

Tetrodes were made of 12 µm diameter tungsten wires (H-Formvar insulation with Butyral bond coat; California Fine Wire) and attached to plastic microdrives (Axona Ltd, St. Albans, United Kingdom). Mice aged 3 to 5 months were implanted with 4-5 independently movable tetrodes in the right MEC (7 wild types and 7 *Cx36*$^{-/-}$) or in the right or both MECs (8 *Uchl*^{Cre} and 12 *CB*^{Cre} mice). The latter two mouse lines were always implanted with one or two microdrives (only right or both MECs) containing tetrodes and an optic fiber (100 µm core diameter, NA 0.22, Doric Lenses Inc., Quebec, Canada). To this aim, mice were kept under anesthesia using 1 - 3 % isloflurane. A small craniotomy was made above the posterior sinus, 3.1 mm from the mid-line. Four miniature screws were attached to the skull, two of which served as ground signal and were placed above the cerebellum. Tetrodes were implanted 0.2 mm in front of the posterior sinus, with the tips oriented 6 degrees posterior in the sagital plane, 0.8 mm deep. The microdrive was fixed to the skull with dental cement and the skin around it was sutured. To minimize pain over the next two days, a subcutaneous injection of buprenorphine was administered every 12 hours.

10.2 Virus injections

The manipulation of CB^{+} and RE^{+} neurons was made possible by two mouse lines expressing Cre recombinase specifically in these neuronal types in the MEC, *CB*^{Cre} and *UchlI*^{Cre}, respectively. These mice were handled exactly like the ones implanted only with tetrodes, with one exception: during the surgery for tetrode implantation, before the tetrodes were inserted into the brain, 500 nl of pAAV-double floxed-hChR2(H134R)-mCherry-WPRE-pA (AAV-DIO-Channelrhodopsin-2 (ChR2)-mCherry) vector, obtained from Karl Deisseroth (Cardin et al., 2010), were injected into the right MEC (3.1 mm from the mid-line, 0.1 mm anterior from the posterior sinus, -1.8 mm deep, with the injection pipette oriented 8 degrees anterior in the sagital plane). This virus enabled the expression of the light responsive (~470 nm) bacterial ChR2 only in neurons expressing Cre recombinase. The expression pattern of this enzyme was tested previously (Fuchs et al., 2016).

10.3 Training and recording

Mice were kept on a 12 h light/dark cycle, with the recordings carried out in the light phase. After a 7 - 10 days recovery period, mice were placed on a restricted food diet, to maintain their body mass at 85% of their free feeding weight, with free access to water. The mice underwent a 2 - 3 weeks training period, during which they became accustomed to forage for food pellets in a gray wooden box, called open field (70 x 70 x 30 cm). The tetrodes were slowly lowered into the desired position over several days, until large theta oscillations and theta modulated spikes were observed during running. When mice would cover the entire surface of the box in ~15 minutes, one recording session per mouse was carried out each day for 2 - 4 weeks, while lowering the tetrodes 25 - 50 μm after each session. In the Cx36 study, each recording session consisted of 20 minutes of exploration in the open field, followed by 20 minutes in a rest box (25 x 25 x 30 cm) where no food was delivered, and another 20 minutes in the open field. Recordings were performed in dim light, and the position and head direction were recorded with a camera throughout the recording using 3 light emitting diodes (red, green and blue) attached to the head stage. The local field potential was passed through a unity-gain buffer preamplifier (Axona Ltd). The signal was amplified (1000x), filtered (0.1–10 kHz, Alpha Omega, Sensorium Inc.), digitized at 20 kHz (PCI-6259, National Instruments) and stored on a computer.

10.4 Laser stimulation

In the mice injected with the virus, a recording session consisted of 20 minutes of exploration in the open field with the laser turned off, 10 minutes in the rest box, and 30 minutes in the open field while 2 ms light pulses were delivered in the right MEC through an optic fiber, at a frequency of 2 Hz, and a power of 30 - 300 μWatt (measured at the tip of the fiber). In a subset of mice that showed a reaction to light in the contralateral side to the injection, the third trial was followed by another 20 minutes in the rest box, where stimulation was performed with 5 ms pulses, delivered in the left MEC at 2 Hz and 1 - 10 mWatt power.

10.5 Spike detection and sorting

Spike detection was performed offline. Spikes were extracted and clustered using principal component analysis, as previously described (Csicsvari et al., 1999). Subsequently, they were further refined manually, using a user interface. Only clusters stable throughout the recording session and with a clear refractory period (> 2 ms) in the spike time autocorrelation were included into the analysis. Cells were classified as putative excitatory or inhibitory based on their mean firing frequency (< 10 Hz for excitatory neurons and > 10 Hz for inhibitory neurons).

10.6 Detection of light activated neurons

In order to automatically detect laser activated neurons, spike-time versus laser-onset crosscorrelations were calculated for $\pm$ 25 ms (with zero being the time of the laser pulse onset), for 0.5 ms bins. The mean number of spikes and standard deviation was calculated based on the 25 ms before the laser onset. A z score (number of standard deviations above mean) was calculated per bin for each neuron. A neuron was considered activated if the z score was > 5. For cells in the stimulation site, latency and jitter were calculated from the distribution of the first spike after laser within 5 ms, as the median and the standard deviation of this distribution, respectively. For cells on the side contralateral to the stimulation site, latency was taken as the time point with the maximal z score for that cell. Identification of neurons that were putatively directly activated by laser (as opposed to synaptic activation) was based on a latency and jitter threshold that was set as the 95% percentile of the distribution of jitter and latencies of cells activated by stimulation in the hemisphere contralateral to the injection. Since these parameters have a high overlap for light activated and synaptically activated neurons (Muñoz et al., 2014), I considered this to be a conservative selection procedure.

10.7 Analysis of neuronal spatial firing properties

Analysis was performed using custom-made C++ programs (written by Prof. Dr. Jozsef Csicsvari and Dr. Kevin Allen), shell scripts and R scripts (written by Dr. Kevin Allen, Dr. Christina Buetfering, Patrick Latuske, and myself). Firing rate maps were constructed based on the first recording trial, for periods with running

speed greater than 3 cm/s (first 20 minutes of the recording session) as follows: the environment was divided into 2 x 2 cm bins and the time the mouse spent in each bin was calculated. These data were used to obtain an occupancy map that was smoothed with a Gaussian kernel (SD = 1.5). The total number of spikes per bin was then divided by the time spent in that bin, to obtain the firing rate. The spatial information score (Skaggs et al., 1996) was calculated from the firing rate map using the following formula:

$$I = \sum_{i=1}^{N} p_i \frac{\lambda_i}{\lambda} log_2 \frac{\lambda_i}{\lambda} \ ,$$

where p_i is the occupancy probability of bin i in the firing map, λ_i is the firing rate in bin i, and λ is the mean firing rate of the neuron.

Spatial autocorrelations were calculated using the firing rate maps (Hafting et al., 2005). Spatial autocorrelation matrices comprised of Pearson correlation coefficients between all possible pairs of bins of the firing rate map with a given spatial lag. The spatial lag of a particular bin of the matrix was determined by the location of that bin relative to the matrix center. Pearson correlations were not considered if fewer than 20 pairs of firing rates were available for that particular spatial lag. Peaks in the spatial autocorrelation matrix were defined as a minimum of 10 adjacent bins with a correlation coefficient higher than a peak detection threshold set to 0.2. The grid score was used to estimate the 60° periodicity in the spatial autocorrelation matrix (Sargolini et al., 2006). The six peaks closest to the center of the map defined a circular region (the central peak was excluded). Pearson correlation coefficients (r) were calculated between this region of the matrix and a rotated version of itself (by 30°, 60°, 90°, 120°, and 150°). The grid score was then calculated using the formula:

$$Gridscore = \frac{r60° + r120°}{2} + \frac{r30° + r90° + r150°}{3}.$$

The grid score threshold used to define a grid cell was obtained using a shuffled distribution generated by shifting the spikes of each neuron on the path of the animal by at least 20 s and calculating a grid score. This was repeated 500 times for all cells, for each genotype. Grid cells were defined as excitatory neurons (mean firing frequency < 10 Hz) that had a grid score higher than the 99th percentile of this distribution (> 0.5). The head direction vector length was calculated based on a histogram containing the firing rates as a function of head direction, for 10° bins, smoothed with a kernel with SD = 1.5.

10.8 Analysis of the power spectrum of the local field potential and running speed

The power spectrum of the raw signal was calculated for the first trial in the open field for periods of running speed > 3 cm/s. The peak power between 5 and 10 Hz in the power spectrum was obtained for each session. To analyze how mobile the mice were, a median speed was calculated per session for each mouse, for periods where running speed was > 3 cm/s.

10.9 Analysis of theta oscillations and theta modulation

The raw signal was band-pass filtered at theta (6 - 10 Hz) and delta (2 - 4 Hz) frequencies. The power (root mean square) calculated for these two frequency bands in 500 ms windows. Epochs with a theta/delta power ratio > 2 were defined as theta epochs. Theta cycles were detected on the filtered (5 - 14 Hz) signal and the positive-to-negative zero crossings were detected within theta epochs. The theta phase of spikes was obtained by linear interpolation and the preferred theta phase of a neuron was defined as the circular mean of its spikes. The theta vector length was calculated by computing the circular mean of the unit vectors representing the phases of each spike on a circle.

10.10 Analysis of neuronal rhythmicity and burstiness

The intrinsic oscillation frequency was calculated from the power spectrum of the instantaneous firing rate and was equal to the frequency with maximal power between 6 - 10 Hz. A theta rhythmicity score was calculated from the power spectrum of the instantaneous firing rate, using the formula (baseline-mean)/(baseline+mean), where the baseline was the mean power for frequencies between 2 - 5 Hz and 11 - 13 Hz and the mean was the mean power between between 6 - 10 Hz. The burstiness of excitatory neurons was calculated based on the first 12 ms of the spike-time autocorrelation, as previously reported (Latuske et al., 2015). Principal component analysis was performed on these bins, and a burstiness score was calculated using linear discriminant analysis, taking into account the weights of the first three principal components. The R script for this analysis was kindly provided by Patrick Latuske.

10.11 Analysis of the spike wave form

An average spike wave form was obtained for each neuron, using the first 100 spikes detected in the trial with the laser switched off. Spike duration was measured at 25% spike amplitude. Spike asymmetry was calculated as the ration between the peak before trough minus baseline and the peak after trough minus baseline after trough (Latuske et al., 2015).

10.12 Analysis of speed modulation

The instantaneous firing rate was calculated for each neuron on 100 ms windows. The same was done for the instantaneous speed. The speed score was calculated as the correlation coefficient of the linear correlation of instantaneous firing rate versus instantaneous running speed. The slope of this correlation showed the steepness of the firing rate increase in relation to running speed.

10.13 Statistics

All scores were computed for each single unit (neuron) and pooled by genotype, unless otherwise stated. Statistical analysis was performed using R. Statistical difference between groups was assessed with the Wilcoxon rank sum test, unless otherwise stated.

10.14 Histology

At the end of the recording period, mice were perfused transcardially with phosphate buffered saline (PBS) and subsequently with a 4 % paraformaldehyde (PFA) solution. The head with the microdrive attached was left in PFA overnight. The next day the brain was removed and sliced sagitally in 50 µm sections. Sections from mice with no virus injection were mounted on gelatin covered glass slides and stained with cresyl violet. The position of the tetrode tips was assessed visually on electronic images taken with an automated bright field microscope (Axio Scan.Z1, Zeiss Microscopy, Germany). Sections from mice where neurons were optogenetically manipulated were stained with various antibodies to asses expression of the virus, following the protocol below: a)

sections were preincubated for one hour at room temperature in a PBS solution containing 2% bovine serum albumin (BSA) for blocking and 0.5% Triton X-100 for permeabilization; b) the sections were transferred to a PBS solution containing 0.1% BSA, 0.2% TritonX-100 and primary antibody (AB). One or two of the following ABs were used: monoclonal or polyclonal anti-calbindin (1:5000, Swant, Bellinzona, Switzerland), monoclonal anti-NeuN (1:2000, Millipore, Temecula, CA, USA), monoclonal anti-reelin (1:2000, Millipore,Temecula, CA, USA), polyclonal WFS-1 (1:500, Proteintech Group, Inc. Chicago, IL, USA); sections were left over night on a shaker at 4°C; c) the next day they were rinsed 3-4 times for 10 minutes in PBS; d) the secondary AB solution contained 0.1% BSA, 0.2% TritonX-100 in PBS and one or two of the ABs AlexaFluor488 and Alexa647 secondary antibodies (1:1000; Invitrogen Darmstadt, Germany); e) sections were rinsed 2-3 times in PBS for 10 minutes and then stained with 4',6-diamidin-2-phenylindol (DAPI) for 10 minutes at room temperature. After rinsing twice with PBS, sections were mounted on glass slides and covered with Mowiol 40-88 and glass coverslips. After drying, all brain sections were imaged with an automated epifluorescence microscope (Axio Scan.Z1, Zeiss Microscopy, Germany) and several closeups were taken with a Zeiss LSM 700 confocal microscope (Zeiss).

11 Path integration on the L-maze assay (performed by Dr. Mariana Gil)

The assay was carried out as previously reported (Allen et al., 2014) with slight modifications. Briefly, mice were trained to find one of three hidden platforms in a circular tank with opaque water (through addition of milk), in complete darkness. The location of the mouse was monitored with an infrared camera and potential auditory cues were masked by white noise. After training, the sample and test trials were carried on. The sample trial consisted of swimming in a corridor that was either straight or L-shaped (in 2 configurations: short arm-long arm, or long arm-short arm). At the end of the corridor, the mouse would find the hidden platform. Each test trial was carried on 15 minutes after the sample trial. There, mice had to swim in the open tank to find the platform, with the start and end position being identical to the sample trial. Each mouse underwent 4 - 6 tests per condition. Therefore, it was expected that mice have different headings (0°, 30°, and 60°) depending on where the platform was placed.

The heading of the swimming path was measured during test trials in respect to a reference axis taken along the start box. The heading as a function of distance to the start box was plotted for each mouse, and the observed heading was calculated as the average of the values obtained at increasing distances from the start box (20 - 90 cm). Statistical analysis was performed using Prism 6 (GraphPad Software). Mice were used as experimental units.

Chapter III - MEC spatial coding in *Cx36*$^{-/-}$ mice

As already mentioned in the first chapter of this dissertation, in my first project I investigated the MEC activity in a mouse line lacking neuronal gap junctions (*Cx36*$^{-/-}$), where place cell activity was shown to be altered and working memory impaired (Allen et al., 2011). I performed *in vivo* tetrode recordings to record electrical activity of single units in the superficial layers of the MEC. This study was meant to extend previous findings on the influence of hippocampal activity on the MEC. In the following sections I will summarize some of the studies where MEC inputs were manipulated, and their most important findings. I will then go on to presenting my results.

12 Manipulation of MEC inputs

In order to induce alterations in the activity of a chosen brain region, researchers have several tools at hand, such as: electrical stimulation, pharmacology (using chemicals to alter the function of specific receptors or ion channels), lesions (that can be produced either chemically or physically) and optogenetics (using light to switch a subset of neurons on or off). Apart from using different manipulation techniques, a factor that adds to the difficulty of comparing results coming from different labs or building on previous research is the fact that they are performed in different organisms, with mice and rats being the most widely used. Below I summarized some recent studies addressing this topic.

12.1 Inactivation or lesion of the hippocampus

The first attempt to investigate the contribution of the hippocampus to grid cell and MEC function was reported in the same study where grid cells were discovered (Fyhn et al., 2004), but before their 60° symmetry was defined. Only the presence and coherence of firing fields were investigated after excitotoxic lesions of the hippocampus, and only a mild decrease in firing field coherence was found. In a follow-up study, Hafting and colleagues (Hafting et al., 2008) inactivated the hippocampus using muscimol and studied the spatio-temporal properties of grid cells on a linear track, observing again only a mild increase in firing field size and instability of recorded neurons 30 minutes after muscimol infusion. These findings were extended by a more recent study, where silencing the hippocampus led to a sharp decrease in spatial periodicity and mean firing rate of grid cells, accompanied by an increase in head direction modulation (Bonnevie et al., 2013). The difference in results might be accounted for by the different time frames of the experiments. The experiments in the first study were performed within 30 minutes from inactivation, whereas in the second study, up to two hours elapsed. Thus, it appears that hippocampal drive is necessary for the expression of grid cell pattern. Namely, place cells could provide direct input to grid cells and contribute themselves to the grid pattern. Alternatively, grid cells need constant excitatory drive to express a firing pattern that emerges within the local network. The authors of the last study provide support for the second hypothesis, by using computational modeling.

12.2 Inactivation of the medial septum

The MS is a subcortical region that was long known to be related to attention and motivation, mainly due to its cholinergic output (Mitchell et al., 1982; Givens and Olton, 1994; Klinkenberg et al., 2011). This output appears to be responsible for the strength and frequency of theta oscillations (6-10 Hz, large amplitude) seen in the hippocampus and MEC of animals during locomotion (Alonso and Köhler, 1984; Lawson and Bland, 1993; Vinogradova, 1995; King et al., 1998; Dragoi et al., 1999; Morris et al., 1999). Activation of cholinergic fibers affects hippocampal oscillations but not the spatial selectivity of place cells (Vandecasteele et al., 2014). Inactivation of the MS using muscimol (a γ-aminobutyric acid receptor type A ($GABA_AR$) agonist) induces a strong decrease in theta power in

both the hippocampus and the MEC, but in terms of spatial selectivity, only grid cells are disrupted (Brandon et al., 2011), while place cells remain unaffected (Koenig et al., 2011; Brandon et al., 2014). However, direct lesion of the MEC induces an increase in place field size in the hippocampus (Brun et al., 2008a; Schlesiger et al., 2015). This suggests that the hippocampus and the MEC might perform parallel processing of spatial signals, and rely on each other's activity for improved performance. However, the cross-talk between hippocampus and MEC is far from being understood.

12.3 Genetic mouse models

The use of genetic manipulations is often hindered by the lack of specific markers, i.e. the potential targets are receptors or molecules that are present throughout the brain, and their ablation is sometimes incompatible with life. Nonetheless, so far two constitutive fore-brain knock-out mouse lines were studied in the context of spatial coding: the HCN1 deficient mice (Giocomo and Hasselmo, 2009) and the *GluA1*$^{-/-}$ mice (Zamanillo et al., 1999).

The cationic hyperoplarization activated current (I_h) contributes to membrane potential oscillations and might rely on hyperpolarization-activated cyclic nucleotide-gated (HCN) channels (Gauss and Seifert, 2000). In rats, the expression of HCN1 channels decreases along the dorso-ventral axis of the hippocampus (Notomi and Shigemoto, 2004). This correlates with an increase in the wavelength of membrane potential oscillations, that could be the cause for the increase of place cell field size and grid cell spacing along the same axis (Jung et al., 1994; Maurer et al., 2005; Kjelstrup et al., 2008; Stensola et al., 2012). Mice lacking HCN1 channels were shown to have increased stability and size of place cell fields (Hussaini et al., 2011), and an increase in grid cell spacing, accompanied by a decrease in the frequency of theta oscillations (Giocomo et al., 2011). At a behavioral level, HCN1 KO mice show impaired motor coordination learning, but preserved spatial reference memory (Nolan et al., 2003).

A second model organism where hippocampal and MEC function was thoroughly investigated are mice lacking the glutamate receptor 1 (GluA1) subunit of α-amino-3-hydroxy-5-methyl-4-isoxazolepropionic acid (AMPA) receptors (Zamanillo et al., 1999; Reisel et al., 2002; Resnik et al., 2012; Allen et al., 2014). Here, data regarding their memory impairments preceded *in vivo* electrophysiological record-

ings. Briefly, spatial reference memory is functional, whereas working memory is impaired in these mice (Reisel et al., 2002). At a neuronal functional level, place cells are less spatially selective (Resnik et al., 2012) and grid cell spatial periodicity is greatly reduced (Allen et al., 2014). Still, grid cells encoded residual spatial information, unlike grid cells in a previous study where the hippocampus was pharmacologically inactivated (Bonnevie et al., 2013). Also, the function of head direction and speed modulated neurons was unaffected. Furthermore, these mice were impaired on a path integration task. These findings emphasize the importance of the hippocampal-entorhinal formation for spatial cognition. A still unresolved question regards the specific role of place cells versus grid cells in path integration.

13 $Cx36^{-/-}$ mice, a tool to study hippocampal input to the MEC

A recent study has found impaired place cells in a mouse lacking neuronal gap-junctions (Allen et al., 2011). This results opens up the possibility of investigating the function of the MEC. These mice show similar memory impairments to *GluA1*$^{-/-}$ mice, but had not been tested on any path integration task. Furthermore, it is difficult to dissociate the effect of hippocampal dysfunction from the effect of the GluA1 subunit deletion on grid cell activity. Although *Cx36*$^{-/-}$ mice come with the same caveats, they are an interesting model to either confirm previous findings or make new discoveries. I will summarize key findings related to gap-junctions and *Cx36*$^{-/-}$ mice in the following sections.

13.1 Expression and function of Cx36

Neuronal gap junctions allow direct communication between intracellular compartments of neurons in several brain areas. They consist of two hexameric hemipores that connect the cell membranes of two cells. Functionally, they facilitate the diffusion of small metabolites, as well as the electrical coupling of cells, and rely on the expression of connexins. During development, a number of different connexins are expressed in both neurons and glial cells. These inter-cellular communication channels play an important role in cell proliferation, migration and

neuronal circuit formation (Dermietzel et al., 1989; Nadarajah et al., 1997). While glial cells retain a high expression of gap junctions in adulthood, neuronal electrical coupling declines considerably after birth and remains restricted to specific subsets of neurons (for reviews see (Belousov and Fontes, 2012; Condorelli et al., 2000; Connors and Long, 2004). The main connexin expressed in neurons in rodents and humans is Cx36. In the adult forebrain, Cx36 is mainly found in interneurons (Venance et al., 2000; Condorelli et al., 1998) and is thought to be involved in synchronizing their activity (Hormuzdi et al., 2001; Buhl et al., 2003).

13.2 Behavioural phenotype of *Cx36*$^{-/-}$ mice

Two different groups generated Cx36 knock-out mice (*Cx36*$^{-/-}$) at roughly the same time (Güldenagel et al., 2001; Hormuzdi et al., 2001). Following their characterization, the first important findings were that these mice develop normally and do not show any obvious behavioral deficit. Also, their scotopic (dim light) vision was affected. A more thorough behavioral testing revealed that these mice have an impaired working memory, but preserved spatial reference memory (Allen et al., 2011). This phenotype is similar to what was observed in *GluA1*$^{-/-}$ mice (Reisel et al., 2002) and suggests that although the hippocampus and MEC are necessary for normal performance on a reference memory task (Hales et al., 2014), a certain degree of neuronal impairment is tolerated by the system.

13.3 Electrophysiological findings in *Cx36*$^{-/-}$ mice

It is thought that in adult animals, gap junctions contribute to the synchronization of neurons, which reflects in the occurrence of γ(30-70 Hz) and ultra-fast, ripple (200 Hz) oscillations both *in vitro* and *in vivo* (Draguhn et al., 1998; Hormuzdi et al., 2001; Maier et al., 2002; Traub et al., 2003). γ-oscillations are associated with exploratory behavior (Bragin et al., 1995), while sharp wave ripples with immobility and non-REM sleep (O'Keefe and Dostrovsky, 1971). Therefore, along with impaired signal transmission between the retinal amacrine cells (Güldenagel et al., 2001), it is expected that network oscillations be also affected in *Cx36*$^{-/-}$ mice (Traub et al., 2002). Experimental results in brain slices have been conflicting, from studies finding an almost complete ablation of ultra-fast ripple oscillations (Maier et al., 2002) to no alteration at all, but impaired γ-oscillations

(Hormuzdi et al., 2001). *In vivo*, it was reported by Buhl and colleagues (Buhl et al., 2003) that γ-oscillations are specifically affected and sharp wave ripples spared, while Allen and colleagues (Allen et al., 2011) reported an impairment of theta oscillations, that were slower than in WT litter mates. The discrepancy in results might arise from the different behavioral paradigms used in the two studies, i.e. wheel running versus open field foraging, or from a different placement of tetrodes.

14 Aim of the study

Previous work in a genetically altered mouse line (Allen et al., 2014) showed that grid cells and path integration are impaired in a mouse with altered place cells. Hippocampal impairment and the effect of the GluA1 subunit ablation on grid cell function could not be disentangled. Furthermore, the contribution of the hippocampus and the MEC to path integration abilities could not be established, due to impairment of both. A third issue that is still not clear is the type of hippocampal input to the MEC that is necessary to sustain the function of grid cells (whether it is place cell spatial firing, hippocampal excitatory drive, or something in between). After detecting unaffected grid cell activity in (*Cx36$^{-/-}$*) mice, I decided to adress all these questions using this model.

Chapter IV - MEC spatial coding in *Cx36*$^{-/-}$ mice - Results

15 Cx36 is essential for electrical coupling in the MEC

Whether gap junctions are present between interneurons of the MEC and if they depend on Cx36 expression is still unknown. Therefore, Dr. Angela Neitz assessed the probability and strength of interneuron coupling in the MEC of wild-type (WT) and *Cx36*$^{-/-}$ mice. Electrical coupling was measured in pairs of FS interneurons patched in acute slices containing the LII of the MEC (Figure 2 A, B). In WT mice, 8 out of 9 cell pairs (89%) were bidirectionally electrically coupled. This coupling was abolished in *Cx36*$^{-/-}$ mice where none of the 10 tested pairs showed either uni- or bi-directional coupling (χ^2 test, $\chi^2 = 15.35$, $p < 10^{-4}$). The coupling coefficient was significantly lower in *Cx36*$^{-/-}$ mice (Figure 2 C, Wilcoxon rank sum test, $W = 90$, $p < 10^{-4}$). These results indicate that MEC FS interneurons are electrically coupled, that the coupling depends on Cx36 expression only, and that upon Cx36 ablation there is no compensatory expression of another connexin. The patch-clamping experiments were performed by Dr. Angela Neitz and analyzed by her and myself. In order to visualize the expression of Cx36, I made use of a *Cx36*^{EGFP} mouse line. Since there are no good antibodies for Cx36, the best alternative was to use a line where Cx36 was coupled to the enhanced green fluorescent protein (EGFP), thus enabling the visualization of the neuronal connexin. Figure 2 A and B show brain sections stained for parvalbumin (PV) or somatostatin (SOM) and EGFP, respectively. The vast majority of Cx36/EGFP$^+$ neurons coexpressed one or the other marker.

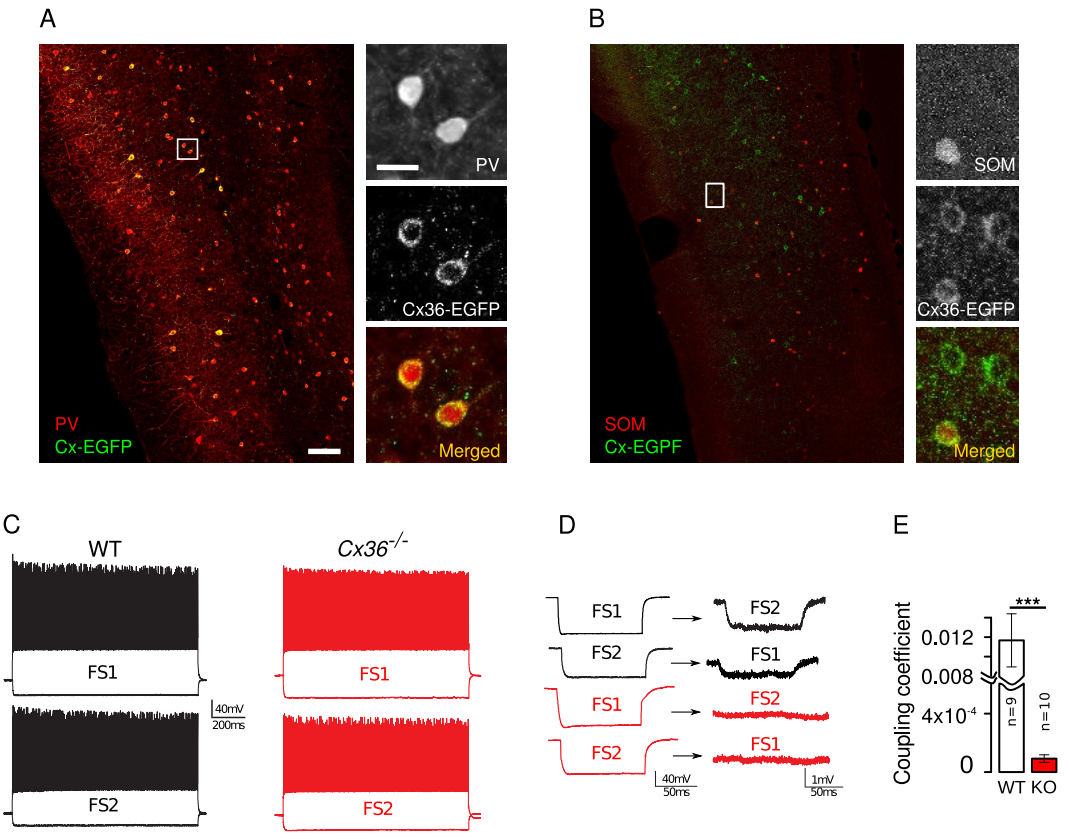

Figure 2. Electrical coupling *in vitro* in the MEC.. **A, B** Immunohistochemical labeling of PV (**A**) and SOM (**B**) in the MEC of Cx36^{EGFP} mice. Images on the right-hand side are higher magnifications of the indicated boxed areas. **C,** Representative firing patterns of fast-spiking (FS) interneurons recorded in MEC LII of wild type (WT, black) and *Cx36*$^{-/-}$ mice (red). **D,** Paired recording of the cells indicated in **C**. Injection of hyperpolarizing current in cell 1 simultaneously induced a deflection of the membrane potential in cell 2 and vice versa in WT mice (black traces), but had no effect in KO mice (red traces). **E,** Mean ($\pm$ SEM) coupling coefficient calculated from both directions. Scale bars in **A** and **B**, 100 and 20 µm, respectively$^{***}p < 0.001$.

16 Grid cell spatial selectivity is not altered in *Cx36*$^{-/-}$ mice

To investigate the activity of grid cells in *Cx36*$^{-/-}$ mice, I performed extracellular tetrode recordings from the MEC of 7 WT and 7 *Cx36*$^{-/-}$ mice. I unilaterally implanted 5 independently movable tetrodes in the MEC, and recorded the neuronal activity as mice ran in a square open field. Overall, 510 and 597 units were recorded in WT and *Cx36*$^{-/-}$ mice, respectively. Tetrode tracks could be observed in the MEC at various dorso-ventral and medio-lateral locations and were similarly distributed in the two groups (Figure 3). In both genotypes, I found neurons

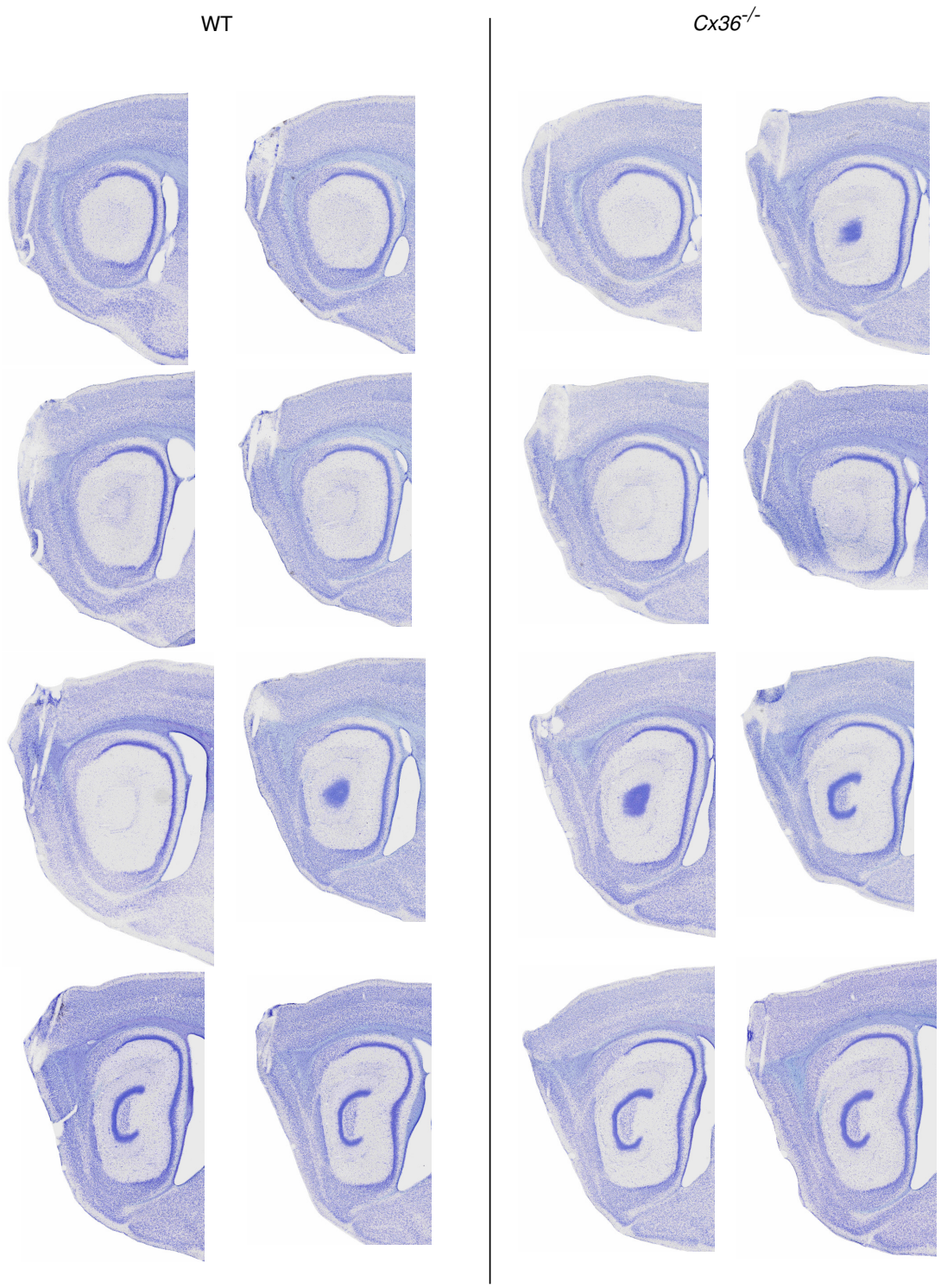

Figure 3. Cresyl violet staining of 50 µthick brain sections. Examples of tetrode traces in WT (left-hand side) and *Cx36*$^{-/-}$ (right-hand side) mice.

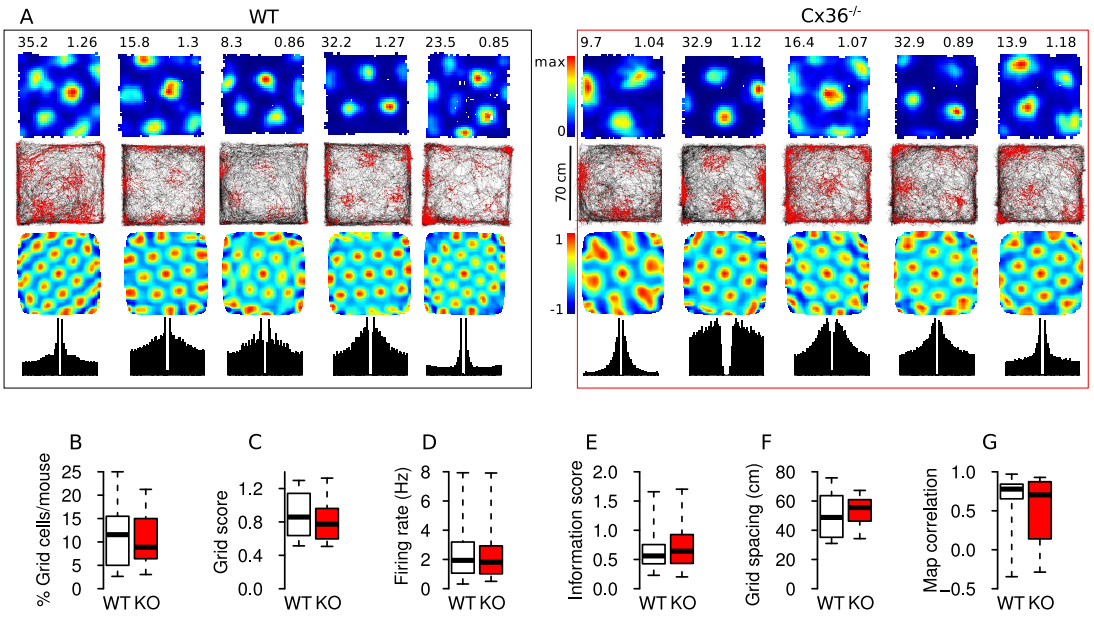

Figure 4. Grid cells of *Cx36*$^{-/-}$ mice exhibit normal grid periodicity and spatial selectivity. A, Top row: color coded firing rate maps of representative grid cells, with the peak firing rate and the grid score (left and right upper corner of each map, respectively); second row: path of the mouse in black with superimposed spikes (red dots); third row: respective spatial autocorrelations; bottom row: the spike time autocorrelations ($\pm$ 50 ms). **B,** Average proportion of grid cells per mouse for WT (n = 7) and *Cx36*$^{-/-}$ (n = 7) mice. **C, D, E and, F** Average grid score, firing rate, information score, and grid spacing for grid cells in WT and *Cx36*$^{-/-}$ mice. **G,** Map correlation of grid cells in the two genotypes. In **C-G**, control: n = 42; *Cx36*$^{-/-}$: n = 63. In **B-G**, the horizontal bar, the box, and the whiskers represent the median, the interquartile range, and the range, respectively. Black = WT, red = *Cx36*$^{-/-}$.

with multiple, well defined, triangularly arranged firing fields that were classified as grid cells (Figure 4 A, grid score > 0.5 and firing rate < 10 Hz). The percentage of grid cells was similar in both genotypes (Figure 4 B, Wilcoxon rank sum test, W = 20, p = 0.81). I then went on to characterize the grid cell populations in both genotypes. I found that grid cells in WT and *Cx36*$^{-/-}$ mice had similar grid score, firing rate, information score and grid spacing (Figure 4 C-F, Wilcoxon rank sum test, grid score: W = 1523, p = 0.19; firing rate: W = 1366, p = 0.78; info score: W = 1164, p = 0.3, grid spacing: W = 1148, p = 0.25). The stability of grid cells, calculated as the firing map correlation in two open field trials recorded 20 minutes apart, was also similar across genotypes (Figure 4 G, Wilcoxon rank sum test, W = 1494, p = 0.26).

17 Theta oscillations are slower in *Cx36*$^{-/-}$ mice

I next characterized theta oscillations and theta modulation of MEC neurons in WT and *Cx36*$^{-/-}$ mice. I found that theta oscillations in *Cx36*$^{-/-}$ mice were significantly slower than in control mice (Figure 5 A, B, Wilcoxon rank sum test, W = 49, $p < 10^{-3}$). This difference in theta frequency could not be explained by differences in the running speed of mice, since animals of both genotypes ran at similar speed in the open field (Figure 5 C, Wilcoxon rank sum test, W = 26, p = 0.9). I next evaluated theta modulation of grid cells and interneurons (firing rate > 10 Hz). Grid cells in *Cx36*$^{-/-}$ mice fired later on the descending phase of the theta cycle than those in control mice (Figure 5 D, permutation test, p = 0.02). A similar trend could be seen in interneurons, but it did not reach significance level (Figure 5 G, permutation test, p = 0.13). Grid cells in *Cx36*$^{-/-}$ mice exhibited stronger theta modulation, as quantified by the theta vector length, than those in controls (Figure 5 E, Wilcoxon rank sum test, W = 828, p = 0.0012). In contrast, interneurons in *Cx36*$^{-/-}$ mice had a lower theta modulation than those in control mice (Figure 5 H, Wilcoxon rank sum test, W = 6503, $p < 10^{-6}$). The intrinsic oscillatory frequency of theta modulated grid cells and interneurons (vector length > 0.2) was significantly lower in *Cx36*$^{-/-}$ than in control mice (Figure 5 F, I, Wilcoxon rank sum test, grid cells: W = 864.5, $p < 10^{-5}$; interneurons: W = 3609, $p < 10^{-9}$), and the same holds true for putative excitatory non-grid neurons (control 8.4 $\pm$ 0.03, *Cx36*$^{-/-}$ 7.8 $\pm$ 0.03, Wilcoxon rank sum test, W = 60312, $p < 10^{-15}$„ control: n = 313; *Cx36*$^{-/-}$: n = 247 neurons). Thus, grid cells in *Cx36*$^{-/-}$ mice were more precisely phase locked to the theta oscillations of the local field potential, fired at a later phase in the theta cycle and had a lower internal frequency than controls.

18 *Cx36*$^{-/-}$ mice can solve a path integration task

To test path integration abilities of *Cx36*$^{-/-}$ mice, Dr. Mariana Gil used the L-maze assay (Allen et al., 2014). This assay was performed in complete darkness and consisted of a sample and a test trial. During the sample trial, mice had to swim and reach a submerged platform placed at the end of one of three corridors: Str (straight), L-S (long-short), and S-L (short-long), in which the platform was located at 0°, 30°, and 60° relative to the start box, respectively. During the test trial, the corridor was removed and the mice' ability to find the platform in the open tank

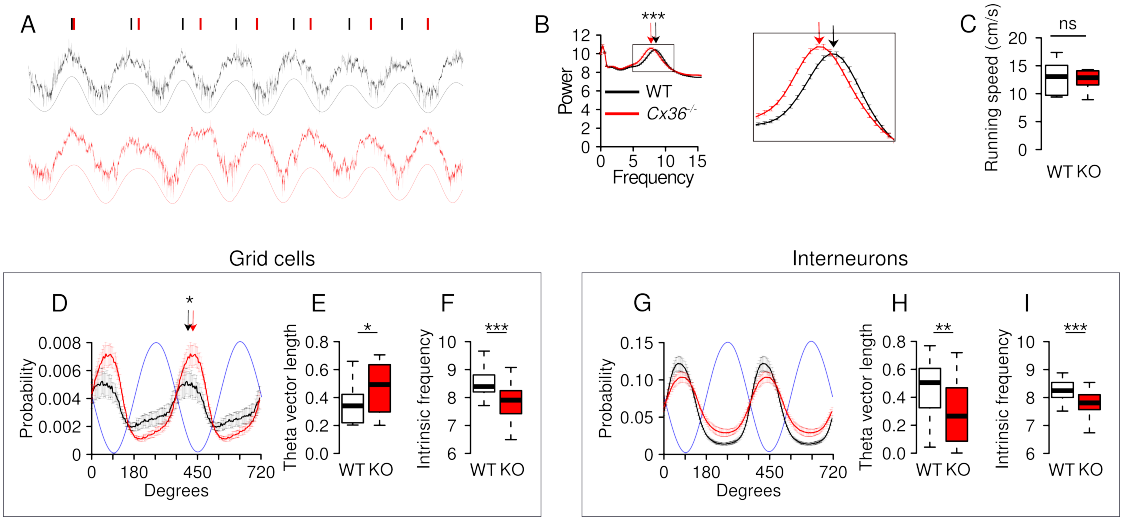

Figure 5. Theta oscillations are slower and neuronal rhythmicity is altered in *Cx36*$^{-/-}$ mice. A, Representative traces of one second local field potential during running The peaks of the filtered trace (5-14 Hz) are marked at the top of the panel. **B,** Average power spectrum of the local field potential when mice are running faster than 3 cm/s. The peak power in the theta range (6-10 Hz) was significantly shifted towards a lower frequency in *Cx36*$^{-/-}$ mice (inset). **C,** Average running speed per mouse in the two groups. Control: n = 7; *Cx36*$^{-/-}$: n = 7. **D,** Probability of firing in the theta cycle for WT and *Cx36*$^{-/-}$ grid cells with a theta vector length > 0.2. Blue trace depicts theta oscillations. Control: n = 24; *Cx36*$^{-/-}$: n = 45. **E,** Average theta vector length for all grid cells. Control: n = 42; *Cx36*$^{-/-}$: n = 63. **F,** Intrinsic oscillatory frequency of theta modulated grid cells (vector length > 0.2). **G-I,** same as **D-F**, for interneurons. Interneurons: control: n = 68; *Cx36*$^{-/-}$ n = 132. Theta modulated interneurons: control: n = 58 *Cx36*$^{-/-}$:n = 77 . In **C, E, F, H and I**, the horizontal bar, the box, and the whiskers represent the median, the interquartile range, and the range, respectively. Black = WT, red = *Cx36*$^{-/-}$.$^{*}p < 0.05$, $^{**}p < 10^{-3}$, $^{***}p < 10^{-6}$.

was tested (Figure 6 A). During the sample trial, mice using path integration build a global vector that, in its reversed form, enables them to quickly find the platform in the open tank during the test trial, thus minimizing the time spent in the water (Allen et al., 2014). Therefore, the prediction of the experiment is that the average heading relative to the long axis of the start box would approach 0°, 30°, and 60° following sample trials in the Str, L-S, and S-L corridors, respectively. The performance of both *Cx36*$^{-/-}$ and control mice matched these predictions, showing headings that approximated 0°, 30°, and 60° following Str, L-S, and S-L swims, respectively (Figure 6 B-D). In both genotypes, the heading at increasing distances from the start box following Str, L-S, and S-L swims differed significantly and no differences were found between genotypes (Figure 6 C; Two-way ANOVA with repeated measures: genotype x corridor interaction: $F_{(2,34)} = 0.05$, $p = 0.95$, effect of genotype: $F_{(1,17)} = 0.04$, $p = 0.84$, effect of corridor: $F_{(2,34)} = 19.33$, $p < 0.0001$.

Tukey's multiple comparisons tests: Control: Str vs L-S, p = 0.31, Str vs S-L, p = 0.0005, L-S vs S-L, p = 0.02; *Cx36*$^{-/-}$: Str vs L-S, p = 0.5, Str vs S-L, p = 0.0003, L-S vs S-L, p = 0.007). Moreover, in both genotypes, the relationship between the expected and observed headings could be approximated by a linear regression whose slope did not differ from one (Figure 6 D; Linear regression: Control: slope = 0.79 $\pm$ 0.13, $F_{(1,22)}$ = 36.26, p < 0.0001; *Cx36*$^{-/-}$: slope = 0.70 $\pm$ 0.09, $F_{(1,22)}$ = 52.91, p < 0.0001. Comparison of fits (H_0: slope = 1): Control: $F_{(1,25)}$ = 6.89, p = 0.23; *Cx36*$^{-/-}$: $F_{(1,28)}$ = 8.19, p = 0.21). These results indicate that *Cx36*$^{-/-}$ mice are able to perform path integration.

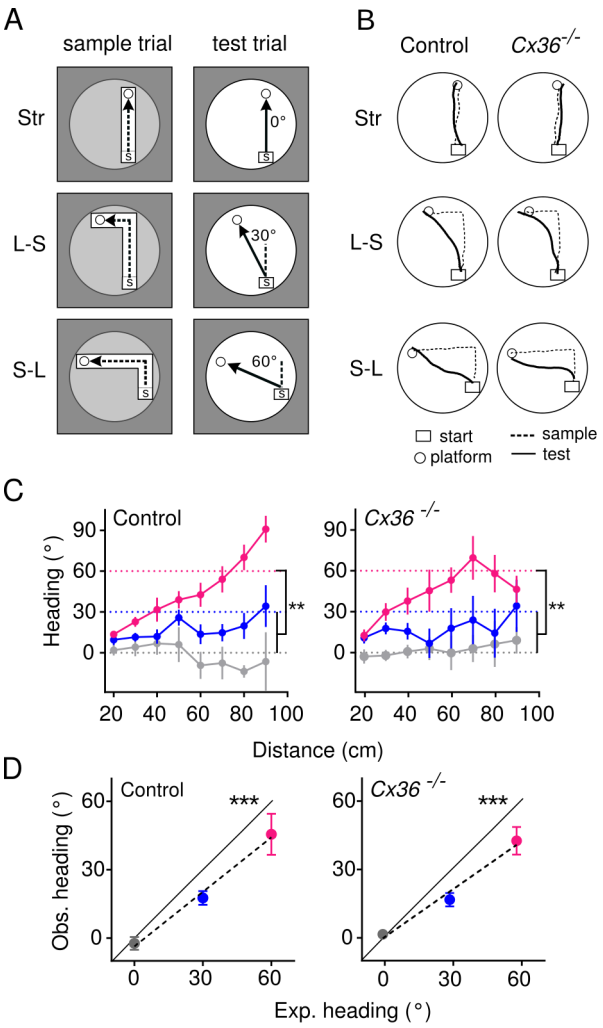

Figure 6. *Cx36*$^{-/-}$ mice exhibit normal path integration abilities on the L-maze assay. A, Schematics of the experimental design. **B,** Examples of sample and test swimming paths by control and *Cx36*$^{-/-}$ mice. **C,** Mean (± SEM) heading at different distances from the start box during test trials following Str, L-S, and S-L swims for control and *Cx36*$^{-/-}$ mice. Dashed lines indicate the expected heading if mice perform path integration (i.e., swam in a straight line to the platform). $^{**}p < 0.05$ after Tukey's multiple comparisons. **D,** Relationship between expected and observed heading (mean ± SEM) for control and *Cx36*$^{-/-}$ mice. The black diagonal line indicates a regression line of slope = 1. $^{***}p < 0.0001$ after linear regression. Str: gray, L-S: blue, S-L: magenta. Control: n = 9; *Cx36*$^{-/-}$: n = 10.

Chapter V - MEC spatial coding in *Cx36*$^{-/-}$ mice - Discussion

In this study I show that Cx36-mediated gap junctions are not essential for the emergence of the grid cell spatial firing pattern. This finding follows up on an earlier study that showed that place cell spatial selectivity is disrupted in *Cx36*$^{-/-}$ mice (Allen et al., 2011). Hence, these differential effects of Cx36 ablation in the hippocampus and the MEC might reflect different functions of these two brain regions in memory and spatial navigation.

19 The role of gap-junctions in the MEC

This study is the first to investigate the probability of interneuron coupling in the MEC. The data show that electrical coupling between FS neurons is similar to what was previously reported in other cortical brain regions (Gibson et al., 1999; Galarreta and Hestrin, 2001; Venance et al., 2000; Meyer et al., 2002), and that this coupling is dependent on Cx36. One of the roles of gap junctions appears to be the synchronization of action potentials in local interneurons at sub-millisecond scale (Gibson et al., 1999; Galarreta and Hestrin, 2001). This process is thought to lead to synchronization of entire neuronal networks, due to the pacing imposed by interneurons (Singer and Gray, 1995; Whittington et al., 1995; Galarreta and Hestrin, 2001). The output of this synchronization are high frequency oscillations (γ- 30-80 Hz, and ripples 200-250 Hz). Gap-junction dependent hippocampal oscillations have been intensely studied both *in vitro* and *in vivo* (Draguhn et al., 1998; Hormuzdi et al., 2001; Maier et al., 2002; Buhl et al., 2003; Traub et al., 2003). γ-oscillations were also detected in the MEC and were shown to be nested within theta oscillations (Chrobak and Buzsáki, 1998; Quilichini et al., 2010). In the experiments performed in our lab, γ-oscillations have a reduced power in the MEC compared to the hippocampus and therefore no reliable analysis can be

performed. Probably, this activity pattern is highly linked to the specific behavioral task. Nonetheless, I could speculate that, given their role in enhancing the effect of MEC input onto hippocampal targets (Buzsáki and Draguhn, 2004; Colgin et al., 2009; Buzsáki and Wang, 2012) and the lack of grid cell firing impairment in *Cx36*$^{-/-}$ mice, it is possible that a reduction in γ-oscillation power affects the timing of incoming MEC inputs to the hippocampus. As a consequence, place cell instability and decreased spatial information is observed, in association with working memory deficits.

20 Grid cell function in mice with impaired hippocampal function

Grid cells are intact in *Cx36*$^{-/-}$ mice, despite impaired hippocampal function. These data complement a previous study that showed that inactivation of the hippocampus produces a strong disruption in grid cell spatial firing, accompanied by a decrease in firing rate and an increase in head direction selectivity (Bonnevie et al., 2013). While the aforementioned study shows that hippocampal excitatory input is indispensable to grid cell function, my data suggest that intact hippocampal spatial coding is not essential for MEC spatial coding. These results challenge computational models proposing that spatial signals from place cells are used as input by grid cells (O'Keefe and Burgess, 2005; Burgess et al., 2007; Kropff and Treves, 2008), and favor simpler network models in which grid cells can be formed in the presence of nonspecific steady external excitatory drive (Bonnevie et al., 2013). However, I would like to emphasize that hippocampal place cells have not lost their spatial selectivity, but display reduced information content, which is a consequence of slightly bigger place fields and increased instability (Allen et al., 2011). Therefore I cannot conclude that hippocampal spatial input does not play a role in grid cell function, but rather that this input does not have to convey precise spatial information and is likely to contribute to MEC function mostly through its excitatory component, but not only.

21 Slower theta oscillations in *Cx36*$^{-/-}$ mice

In contrast to the differential effect of Cx36 ablation on place cell and grid cell firing, theta oscillations and theta modulation of neurons, present during locomotor activity, are altered both in hippocampal and MEC neurons. This finding could be explained by the fact that theta oscillations in the hippocampal - parahippocampal region are sustained by medial septum and the vertical limb of the diagonal band of Broca (MSDB) projections (Alonso and Köhler, 1984; Lawson and Bland, 1993; King et al., 1998; Dragoi et al., 1999; Morris et al., 1999; Heys et al., 2012; Vandecasteele et al., 2014). In this brain area, some neurons display rhythmic activity that correlates with hippocampal theta and sharp-wave ripples (Dragoi et al., 1999). This rhythmicity is intrinsic and relies on HCN channels (Varga et al., 2008), and it can be speculated that gap junctions might play a role in the synchronization of these neurons. This hypothesis is indirectly supported by the finding that application of gap-junction blockers onto MSDB suppresses kainate induced theta oscillations *in vitro* (Garner et al., 2005). Therefore, the lower theta frequency in both brain regions most likely reflects altered septal input.

Previous studies showed that a reduction in theta frequency correlates with an increase in grid spacing, suggesting that theta frequency and grid cell spacing are mechanistically related (Giocomo et al., 2011; Barry et al., 2012). Here, however, I found that grid cell spacing is preserved despite a significant decrease in both external theta and intrinsic cell oscillations. Moreover, the oscillatory frequency of interneurons was also decreased, as opposed to a study where the HCN1 channel was knocked out and primarily grid cells were affected (having increased spacing, decreased frequency of intrinsic oscillations and decreased speed modulation) (Giocomo et al., 2011). However, the differences might rely on mechanistic causes. In the present study, the concurrent decrease in theta frequency in the hippocampus and the MEC suggests that the medial septum is involved. Regarding the study of Giocomo and colleagues (Giocomo et al., 2011) it should be noted that the HCN1 channel is not expressed in the medial septum (Santoro et al., 2000), and no decrease in the frequency of the theta oscillation in the hippocampus of HCN1 KO mice was detected (Hussaini et al., 2011). Consequently, it could be that impairment of an intracellular oscillator (the HCN1 channel) affects the grid spacing, whereas when both extracellular and intracellular oscillators are affected, the grid spacing remains intact. Alternatively, the differences are to small to be detected within the present data set.

22 The role of the MEC in path integration

Cx36$^{-/-}$ mice are a good tool to distinguish the contribution of place and grid cells to different forms of navigation strategies. In previous work in our lab it was found that *Cx36*$^{-/-}$ mice exhibit impaired short-term spatial memory (Allen et al., 2011). Taking into account the present findings, it can be inferred that grid cell firing is not essential for the development of short-term spatial memory. In addition, *Cx36*$^{-/-}$ mice have normal path integration abilities. Earlier studies suggest that spatially selective cells in the hippocampus and the para-hippocampal region are involved in path integration (Whishaw and Maaswinkel, 1998; Maaswinkel et al., 1999; Parron and Save, 2004; Van Cauter et al., 2013; Allen et al., 2014). However, in these studies the role of place and grid cells could not be assessed separately due to the nature of the performed manipulations. Since the discovery of grid cells it has been suggested that these cells underlie path integration (Hafting et al., 2005; McNaughton et al., 2006; Moser et al., 2008). However, unequivocal evidence showing that grid cells are essential for path integration has been missing, and, in addition, the contribution of place cells to path integration has never been experimentally discarded. Here it can be ruled out that intact place cell spatial selectivity is required for successful path integration, which indirectly supports the hypothesis that grid cells underlie this process.

23 Technical limitations

One major limitation of this study is the artificial experimental setup. The square gray box where mice foraged for food pellets everyday for several weeks in a row does not pose any behavioral challenges. Therefore, although in the present paradigm grid cells show normal 60 degree symmetry, it is possible that differences in their function might be revealed by using a battery of environmental setups, like boxes of different sizes, linear track or zig-zag maze. This way, a series of other grid cell properties could be investigated, like remapping (distortion, rotation) and theta phase precession (Stensola et al., 2012). However, it is not possible to discern between the effect of Cx36 ablation and the effect of hippocampal impairment in the event that dysfunctionalities are found, which is a second limitation, inherent to global knock-out animals.

Chapter VI - Functional identity of anatomically defined MEC neurons

Defining anatomical neuronal categories is crucial to understanding neuronal network function. Various molecules can be used as markers to aid in distinguishing, for example, excitatory from inhibitory neurons (such as parvalbumin, somatostatin, glutamic acid decarboxylase, glutamate synthase) or to define groups of neurons based on a specific neurotransmitter, neuromodulator or receptor they contain (serotonin, dopamin, acetyl choline) (Cuello et al., 1983). Some categories are relevant only for specific brain regions, with neuronal types that are present in very small numbers, clustered in nuclei, while others comprise neurons that are scattered throughout the brain and express one or several known markers. By labeling these neuronal markers, various micro-structures of the brain can be highlighted, such as the cortical columns in the somatosensory cortex (called barrel cortex in rodents) or in the visual cortex (Hubel and Wiesel, 1959; Woolsey and Van der Loos, 1970; Mountcastle, 1997). Over the last decades, several proteins that highlight various degrees of cell clustering have been discovered in the MEC. These findings are summarized in the following paragraphs.

24 Grid cells are organized in modules

Several features of grid cells suggest that they may be anatomically clustered. Neurons recorded on the same tetrode (i.e. are found within a radius of 50-100 µm, see Henze et al., 2000) can be described by similar parameters like spacing and orientation (Hafting et al., 2005; Brun et al., 2008b). Moreover, the spacing of grid cells does not increase continually, but in a discrete manner, with a ratio of consecutive spacings of approximately 1.5 (Stensola et al., 2012). Grid cells recorded on the same tetrode often have similar orientation, spacing, and distortion (Hafting et al., 2005; Fyhn et al., 2007; Stensola et al., 2012). Grid

cells that have similar characteristics are said to belong to a module. However, a thorough analysis of tetrode tracks in a study where large numbers of grid cells were recorded simultaneously seems to suggest that functional grid cell modules overlap anatomically to a great extent, with the degree of overlap increasing from dorsal to ventral MEC (Stensola et al., 2012). However, as I will show in the next sections, the MEC displays various types of cell clusters, whose relation to functional modules is not known.

25 Morphological organization of the MEC

The medial entorhinal cortex is a six layered structure, with neurons present in high numbers in layers II/III and V/VI, and reduced numbers in layers I and IV (van Strien et al., 2009). At present, it is not known how anatomically defined neurons relate to function *in vivo*. Progress is being made toward direct optical access to neurons in moving mice, albeit at currently exorbitant costs (Barretto and Schnitzer, 2012; Ziv et al., 2013; Kitamura et al., 2014). Several neuronal markers have drawn the attention of researchers working in the field of grid cells, due to their specificity for certain neuronal morphologies and because of being highly expressed in the superficial layers of the MEC, where grid cells reside. These are reelin, calbindin, and Wolfram syndrome 1 (Wfs1) (Varga et al., 2010; Kitamura et al., 2014; Ray et al., 2014), with and additional marker for neuronal activity (cytochrome oxidase) (Hevner and Wong-Riley, 1992; Burgalossi et al., 2011).

25.1 Histological hallmarks of the medial entorhinal cortex

In the MEC, patches could be detected in early studies using a cytochrome oxidase staining (Hevner and Wong-Riley, 1992). These are putative high activity regions and are found in the superficial layers of the MEC. A recent study went back to these findings and showed that these patches increase in size from dorsal to ventral, are often surrounded by myelinated axons, and cells within the patches generally have dendritic arbors restricted to the patch (Burgalossi et al., 2011). It is still unclear how these confined regions correlate to grid cell modularity. Specifically, the number of cytochrome oxidase patches is very large (in the order of hundreds) (Hevner and Wong-Riley, 1992; Burgalossi et al., 2011),

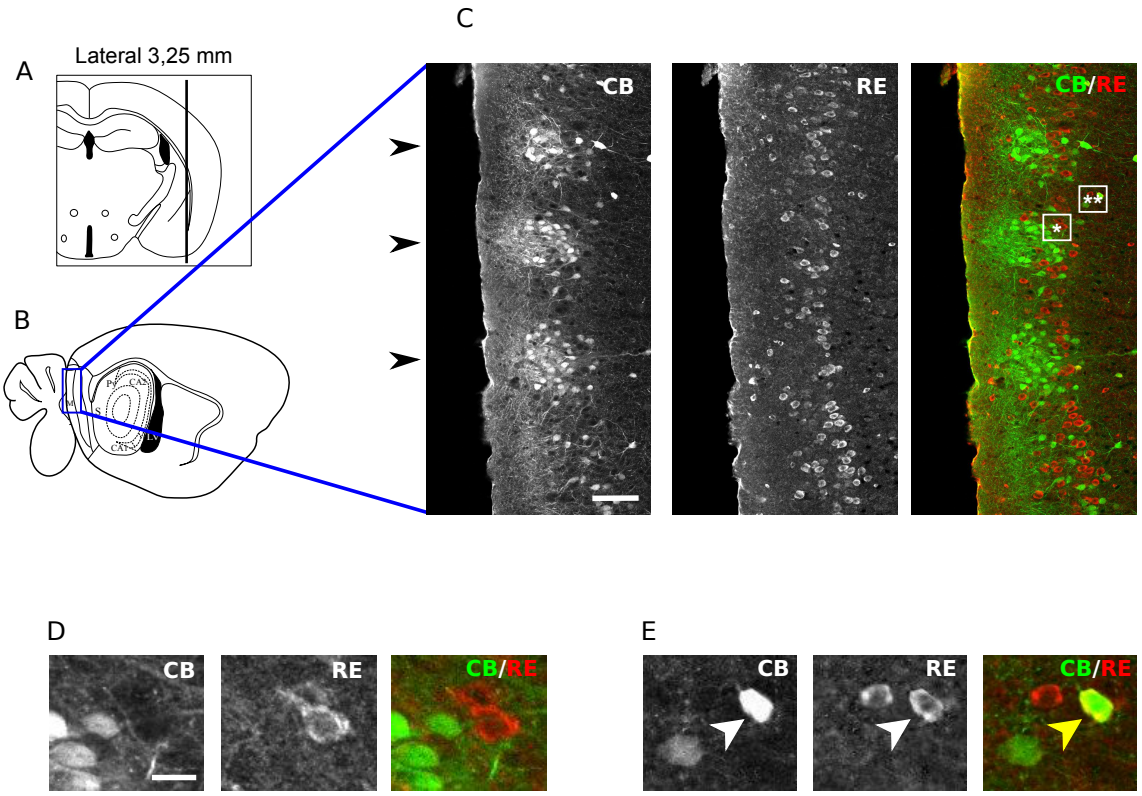

Figure 7. Anatomical organization of the major cell populations in the MEC. A,B, Schematics of the cutting plane position and localization of the structures shown in (**C**). **C,** Fluorescently labeled CB and RE neurons in the MEC. Arrows point toward CB "islands". **D,** Magnification of the inset marked with * in (**C**), showing adjacent CB^+ and RE^+ neurons. **E,** Magnification of the inset marked with ** in (**C**), showing one neuron that is CB^+/RE^+ (white and yellow arrow head). Scale bars 100 and 20 µm.

which contrasts to the number of estimated grid modules (4 - 10) (Stensola et al., 2012). This is one of the reasons why scientists have turned their attention toward $CB^+/Wfs1^+$ and RE^+ neurons (see Figure 7 C). These two neuronal populations are arranged in a distinct pattern, with $CB^+/Wfs1^+$ neurons forming clusters visible in tangential and sagittal sections of the MEC, and RE^+ cells forming a stripe of cell bodies below and around the $CB^+/Wfs1^+$ clusters (Kitamura et al., 2014; Ray et al., 2014; Fuchs et al., 2016) (Figure 7 C). Furthermore, $CB^+/Wfs1^+$ patches are present across species, which suggests an evolutionarily preserved origin (Naumann et al., 2016). $CB^+/Wfs1^+$ and RE^+ neurons are largely mutually exclusive, with only a small percentage (2 - 3%) of overlap (Varga et al., 2010; Fuchs et al., 2016) (see Figure 7 D and E). The cell populations highlighted by these two markers differ in terms of cell morphology and pattern of axonal projection, as explained below.

25.2 Neuronal sub-types and connectivity in the MEC

Initially, two main morphological types of excitatory neurons were described in the superficial layers of the MEC: pyramidal and stellate cells (Alonso and Klink, 1993). A recent study extended this knowledge, by distinguishing four cell types: stellate, intermediate-stellate, intermediate-pyramidal, and pyramidal, based on their morphology and electrophysiological properties (Fuchs et al., 2016). The stellate and intermediate-stellate neurons express RE, but not CB, while pyramidal and intermediate-pyramidal neurons express CB and Wfs1, but not RE. These four anatomical cell types differ not only in their intrinsic properties, but also in their local connectivity. It is widely accepted that recurrent inhibition is extensively present in the MEC, and is thought to be important for grid cell pattern generation (Burak and Fiete, 2009; Couey et al., 2013; Pastoll et al., 2013; Solanka et al., 2015). Interestingly, most cell types receive input from and provide input to fast spiking PV^+ and low threshold SOM inhibitory neurons. Pyramidal neurons however receive inhibition only from cholecystokinin$^+$/5$HT_3{}^+$ interneurons (Varga et al., 2010; Fuchs et al., 2016). These results have been shaping the view on putative grid cell pattern emergence mechanisms, with computational models shifting from excitatory recurrent connectivity (Fuhs and Touretzky, 2006; McNaughton et al., 2006) to inhibitory recurrent connectivity (Burak and Fiete, 2009; Couey et al., 2013; Pastoll et al., 2013). The latest models need further revision in the light of new findings, that show that although stellate-stellate and pyramidal-pyramidal excitatory connections are extremely rare (Couey et al., 2013; Fuchs et al., 2016), intermediate cell types have 5 - 10% connection probability among each other and with stellate and pyramidal cells (Fuchs et al., 2016).

25.3 Distal targets of MEC neurons

Yet another difference that reinforces the idea that pyramidal and stellate neurons (along with their intermediate types) might constitute different functional neuronal populations is their output to other brain structures. It is by now textbook knowledge that LII stellate cells give rise to the major cortical afferent of the hippocampus, namely the perforant pathway (Cajal, 1911). More recent evidence has unraveled that all MEC layers have some contribution to the perforant pathway (for a review, see (van Strien et al., 2009)). However, pyramidal cell projections are still under debate. While some groups find that these cells project to the contralat-

eral MEC and not to the ipsilateral hippocampus (Varga et al., 2010; Fuchs et al., 2016), others find an ipsilateral projection to CA1 (Kitamura et al., 2014; Sürmeli et al., 2015) and only sparse projections in the contralateral MEC (Kitamura et al., 2014). These discrepancies might arise from the use of different mouse lines and/or techniques (retrograde labeling in WT mice versus virus injection into a mutant mouse line where expression of a fluorescent marker can be restricted to a specific cell population, i.e. CB^{Cre} - Fuchs et al., 2016 and Wfs1-Cre - Kitamura et al., 2014).

26 Bridging anatomy and function in the MEC

As mentioned previously and as demonstrated by the examples provided above, there is a wealth of data describing anatomical and functional parameters of several cell types in the MEC *in vitro*. These data fueled ample speculation regarding the cellular identity of grid cells. Initially, the preferred candidates were stellate cells, due to their strong hippocampal projection and frequent recurrent inhibitory connectivity postulated to be necessary for grid cell pattern emergence (Couey et al., 2013). However, several recent *in vivo* studies showed that both pyramidal and stellate cells are likely to be grid cells.

26.1 *In vivo* patch-clamp studies of grid cells

The first evidence, albeit indirect, that grid cells can have either pyramidal or stellate morphology came from the lab of Michael Brecht (Burgalossi et al., 2011). Juxtacellular recordings in rats running on a rectangular track revealed multipeak firing in a number of cells whose morphology was subsequently reconstructed, to reveal the two cell morphologies. This activity resembles the pattern seen when recording grid cells on a linear track, but it offers no certainty that these are indeed grid cells. The debate was to some extent put to rest by a study that showed that both pyramidal and stellate cells exhibit a grid cell pattern in behaving mice (Domnisoru et al., 2013). However, the focus of that work was to test predictions of computational models for grid cell pattern emergence, and therefore no thorough histological analysis was reported. Therefore, the question whether and how pyramidal grid cells differ from stellate grid cells, and how they are distributed within the two cell populations was left open.

26.2 Optical identification of grid cells

Calcium imaging *in vivo* is a new emerging technique that allows monitoring the activity of large numbers of genetically tagged neurons (Ziv et al., 2013; Sun et al., 2015). A recent study used miniature microscopes to visualize cells expressing a calcium indicator in either $Wfs1^+$ (that were called 'island' cells) or RE^+ neurons (called 'ocean' cells) in behaving mice (Sun et al., 2015). It appears that grid cells are present in similar proportions in both cell populations, along with spatially and non-spatially selective cells. Another key finding was that $Wfs1^+/CB^+$ neurons were much more strongly correlated to the animal's running speed. The authors speculated that island cells contribute to path integration, while ocean cells confer contextual information to spatial representations.

26.3 Combining experimental data and theoretical predictions

Obtaining information about anatomical and histological characteristics of neurons *in vivo* is technically challenging. This restricts the number of identified neurons to at most a few dozens (Burgalossi et al., 2011; Domnisoru et al., 2013; Schmidt-Hieber and Häusser, 2013; Tang et al., 2014; Ray et al., 2014; Ebbesen et al., 2016). To circumvent this issue, some groups have tried to find functional hallmarks of identified neurons and extrapolate them to larger numbers of neurons (Tang et al., 2014; Sun et al., 2015; Ebbesen et al., 2016). Based on neuronal temporal discharge properties, Tang and colleagues (Tang et al., 2014) have proposed that pyramidal, CB^+ neurons in LII of the MEC are six times as likely as stellate neurons to display a grid pattern, while stellate CB^- neurons are ten times as likely as pyramidal cells to display border cell activity. Latuske and colleagues however (Latuske et al., 2015) showed that inter-spike interval can also be a good predictor of spatial selectivity and post-synaptic partners. For example, roughly two thirds of the grid cells were shown to fire preferentially bursts of action potentials *in vivo*, while one third were non-bursty. If burstiness would be a predictor of cell type (e.g. pyramidal or stellate), these numbers would be in stark contrast to the ratios reported by Tang and colleagues. Further experiments are needed to test if and how such approaches can be used to classify neurons.

26.4 Aim of the study

The studies summarized in the previous paragraphs provide information regarding anatomical and functional characteristics of neurons in the MEC. Given the small number of anatomically identified neurons in *in vivo* studies, the question whether and how RE^+ and CB^+ are functionally different remains open. I therefore probed the properties of RE^+ and CB^+ neurons in the MEC of running mice and investigated their spatial firing, speed dependence, and theta modulation, by using optogenetical tagging of the two neuronal populations combined with tetrode recordings. My approach enabled me to explore another issue, that was left so far completely untouched *in vivo*, that of the contralateral targets of projecting neurons (for a thorough *in vitro* investigation, see Fuchs et al., 2016).

Chapter VII - Functional identity of anatomically defined MEC neurons - Results

Uchl1^{Cre} and *CB*^{Cre} mouse lines were characterized previously (Fuchs et al., 2016). Briefly, in the *Uchl1*^{Cre} line, Cre recombinase overlaps with RE expression to a great extent (93%) and in the *CB*^{Cre} mouse line it is expressed in CB^{+}/Wfs1^{+} neurons. By injecting a virus containing a double floxed inverted version of ChR2 coupled to mCherry (AAV-DIO-mCherry), only cells expressing Cre recombinase will express the ChR2 gene.

27 Experimental paradigm

8 *Uchl1*^{Cre} mice and 12 *CB*^{Cre} mice received an injection with AAV-DIO-mCherry in the right MEC and were implanted with two microdrives, each containing four tetrodes and one optic fiber, bilateral in the MEC (Figure 9 A).

27.1 Localization of tetrodes and virus expression

Mice were only included in the analysis after confirming that the tetrodes and injection site were in the MEC. In order to maximize the chances of overlap between injection site and tetrodes, a large amount of virus was injected (500 nl, in comparison to 300 nl in Fuchs et al., 2016). In most mice, the expression of mCherry could be seen in the dorsal half of the MEC (see Figure 8). In some mice the injection spread more ventrally and medio-laterally and occasionally reached the lateral entorhinal cortex (LEC) or the parasubiculum (PaS). In the contralateral hemisphere, thin axons were detected in all *CB*^{Cre} mice. Surprisingly, in 4 out of 8

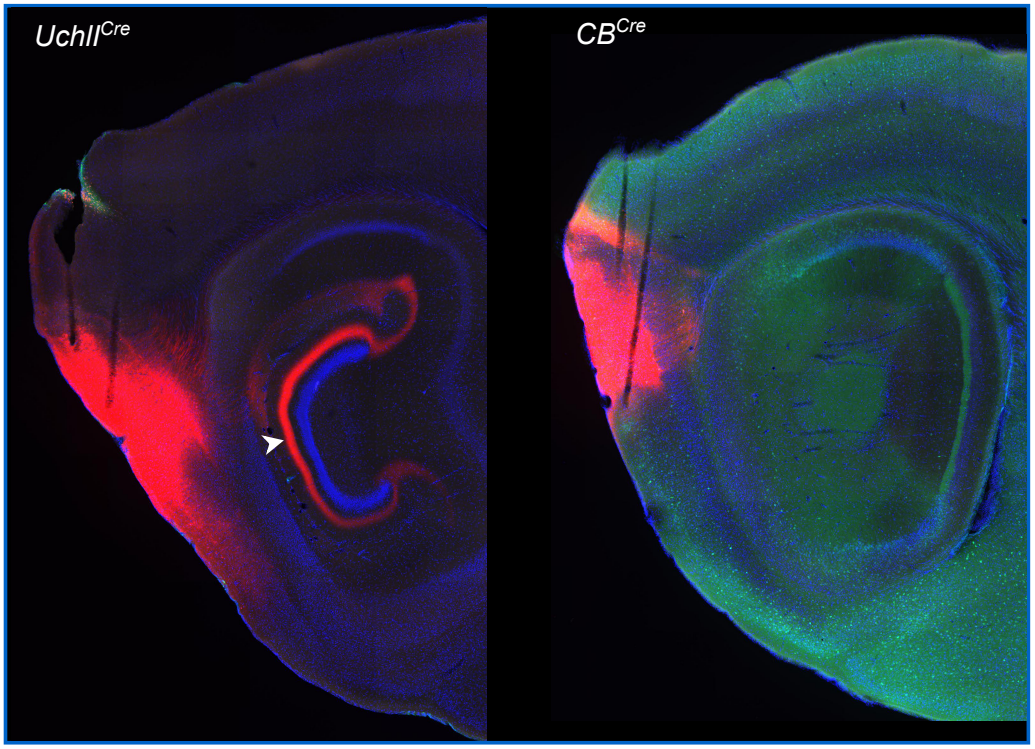

Figure 8. Placement of tetrodes and injection site. Sagital brain sections, 50 µm thick, showing expression of ChR2-mCherry in RE$^+$ neurons (in an *UchlI*^{Cre} mouse) and CB$^+$ neurons (in a *CB*^{Cre} mouse). Black traces were left after tetrodes were removed. The white arrow indicates the terminals of the perforant path in the dentate gyrus of the hippocampus, made visible through expression of mCherry in stellate cells in the MEC. The left-hand side section was stained for RE (green) and DAPI (blue), and the left-hand side section for CB (green) and DAPI (blue).

UchlI^{Cre} mice, a thick axonal plexus could be seen in LII of the contralateral MEC as well. These axons originated in the PaS, in CB$^-$/RE$^-$/Wfs1$^+$ neurons (personal communication from Roberta Pinna).

27.2 Recording protocol

Mice were trained to run in a box and forage for pellets. Each day, a recording session consisted of three or four trials. The first trial was used to obtain the natural neuronal characteristics, and the laser was switched off. This trial was followed by 10 minutes in a rest cage, which is necessary to maintain the motivation of mice to run in subsequent trials. The third trial was performed with laser stimulation. Brief 2 ms laser pulses were delivered at 2 Hz in the right hemisphere (where some cell bodies expressed ChR2). A fourth trial in the rest cage was carried on only in mice where LFP deflections were observed in the contralateral

hemisphere, which rendered likely the possibility of finding post-synaptic targets of projecting neurons (Figure 9 B).

27.3 Activation of neurons in the ipsi- and contralateral MEC

By using this experimental setup, four scenarios arise: two for laser stimulation in the injection site and two for the laser stimulation in the contralateral hemisphere. Simulation on the side with the virus injection will: i) activate ChR2$^+$ neurons (and their local targets in the MEC) at low latency (1 - 5 ms) (Figure 9 C) and ii) due to traveling action potentials to the contralateral hemisphere, will activate postsynaptic targets of projecting neurons, at longer latency (6.5 - 25 ms) (Figure 9 D). Stimulation on the contralateral side (in respect to the injection) will: i) activate post-synaptic targets of ChR2$^+$ axon terminals at low latency (Figure 9 E) and ii) will activate neurons on the injection side either via retrogradely traveling action potentials or as post-synaptic targets of ChR2$^+$ neurons at longer latency (Figure 9 F). Indeed, I observed all four scenarios in my recordings. However, due to the impossibility of establishing the origin of axon potentials traveling across hemispheres, I only performed further analysis on cells activated in the stimulation site (i.e. cells in the right hemisphere when stimulating in the right hemisphere and cells in the left hemisphere when stimulating in the left hemisphere).

28 RE$^+$ and CB$^+$ neurons comprise a variety of functional cell types

Overall, 502 neurons were recorded in *Uchl1*^{Cre} mice and 841 in *CB*^{Cre} mice in the right hemisphere, and 411 neurons in *Uchl1*^{Cre} and 786 neurons in *CB*^{Cre} mice in the left hemisphere. The majority of activated neurons in the injection site had a latency below 5 ms (Figure 10 A, B; 30.47% of total recorded neurons in *Uchl1*^{Cre} mice and 28.41% in *CB*^{Cre}). In the contralateral hemisphere, 40 and 27 neurons were activated, respectively (Figure 18 A, B). In almost all neurons, the laser induced response was followed by a period of reduced activity (Figure 10 A, B).

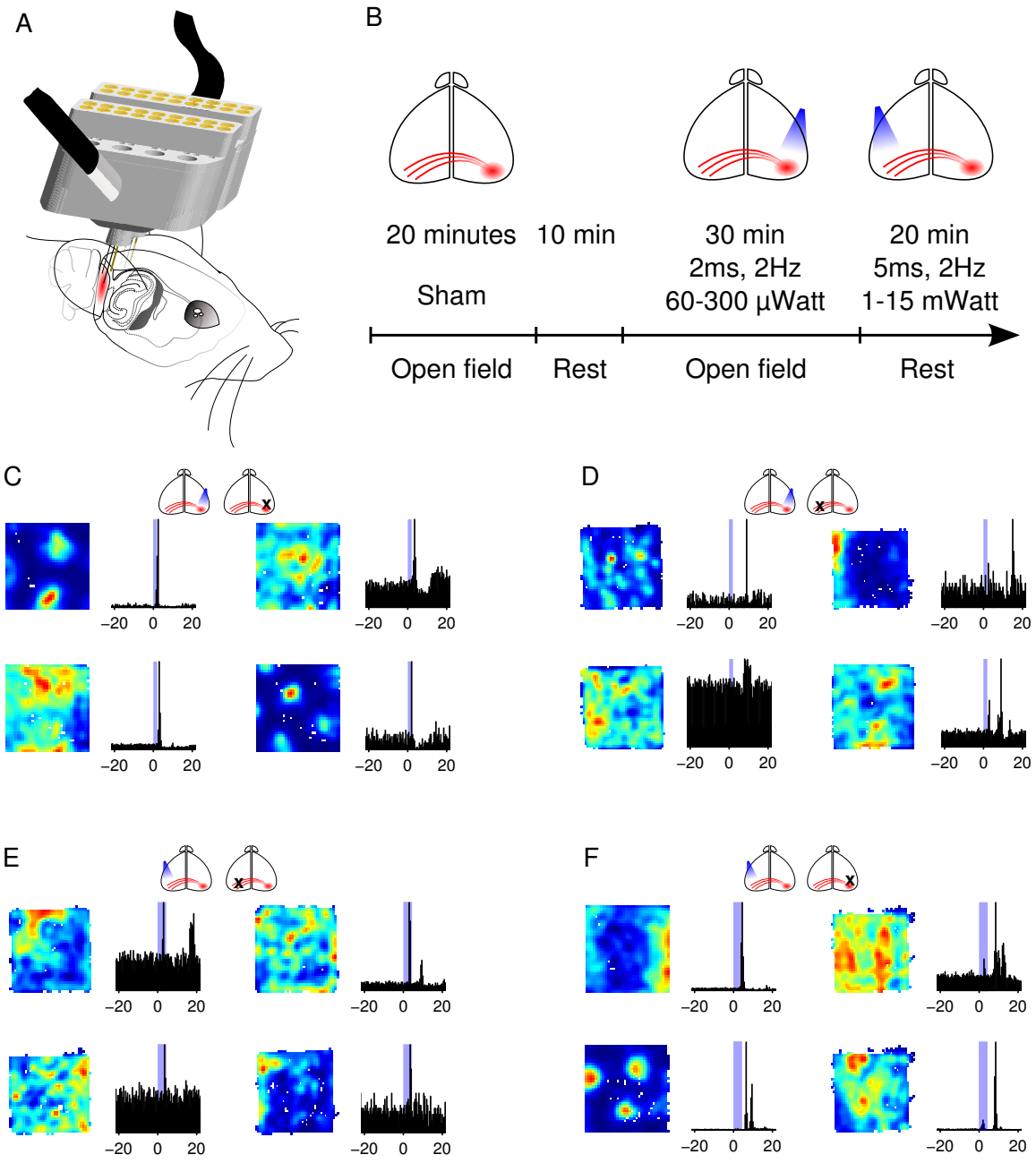

Figure 9. Placement of tetrodes and optic fiber and recording paradigm. A, Graphical representation of the mouse head and brain region in the sagittal plane where tetrodes and optic fibers were placed. The red spot represents the site of virus injection. The black tubes are detachable optical fiber patch-cords that were connected to the fiber optic ferrulae (white-gray cylinders coming out of the microdrive) during the recording session. **B,** Schematic representation of a recording session, comprising four trials, in the shown order. The last two trials were done during laser stimulation, first in the injection site, and second in the site of projection fiber terminals. **C, D, E, F,** Examples of color coded firing rate maps and spike-time versus laser onset cross-correlations ($\pm$ 20 ms) for each of the four scenarios described in the text. Blue cone depicts laser stimulation site and **x** marks the recording site.

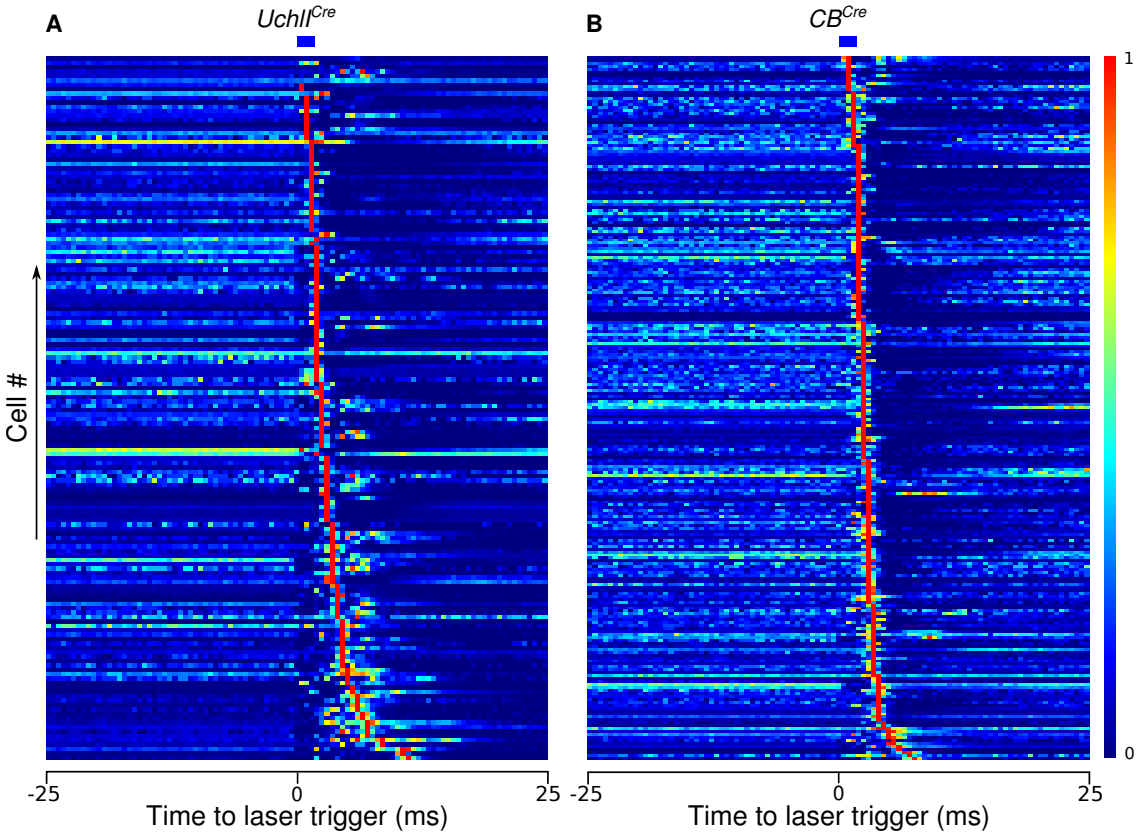

Figure 10. Color coded laser cross-correlations of cells activated on the injection side. A, Laser cross-correlations of all cells activated within 5 ms from laser onset (blue rectangle on top of the picture) in *UchlI*^{Cre} mice. Each line represents a cell, with each bin (0,5 ms) normalized to the bin with the highest number of spikes for that cell. **B,** The same representation for cells recorded in *CB*^{Cre} mice.

28.1 Functional identity of neurons activated at low latency

Neurons activated at < 5 ms latency belonged to several functional categories. As such, the first observation was that the laser led to the activation of a large number of spatially selective cells in *CB*^{Cre} mice (sparsity > 0.4), which was significantly higher than the proportion of spatially selective neurons activated in *UchlI*^{Cre} mice (Figure 11 B, middle, χ^2 test, $\chi^2 = 31.62$, $p < 10^{-7}$). Conversely, in *UchlI*^{Cre} mice a larger proportion of grid cells was activated (Figure 11 B, middle, χ^2 test, $\chi^2 = 13.24$, $p = 0.00027$). The proportion of non-spatial neurons was similar in the two groups (Figure 11 B, upper panel, χ^2 test, $\chi^2 = 2.73$, $p = 0.09$). I did not perform a quantification of head direction and conjunctive cells, due to low numbers of neurons. These differences might arise from a difference in sampled neurons. Indeed, in *CB*^{Cre} mice, significantly more spatially selective neurons were recorded overall (Figure 11 B, left, χ^2 test, $\chi^2 = 50.44$, $p < 10^{-11}$). The same was true

for grid cells recorded in *Uchl1*^{Cre} mice (Figure 11 B, left, χ^2 test, χ^2 = 20.99, p < 10^{-5}). This suggests that the two cell populations might be similar. However, these neurons cannot be assumed to be all ChR2$^+$, since the probability of excitatory connectivity within the MEC is not negligible (Fuchs et al., 2016) and latency and jitter of light activated neurons and post-synaptic neurons overlap to a great extent (Muñoz et al., 2014). Rather, they are likely a mixture of ChR2$^+$ neurons and post-synaptic targets.

28.2 Functional identity of RE$^+$ and CB$^+$ neurons

In the absence of an internal control, it would be difficult to establish criteria of selection for putative ChR2$^+$ neurons. Using previous studies as reference would be misleading, since results differ greatly between labs and across species. For example, reported latencies of optogenetic activation range from 1.5 to 10 ms (Kvitsiani et al., 2013; Zhang et al., 2013; Muñoz et al., 2014; Buetfering et al., 2014). Another parameter often used to discern directly from indirectly activated neurons is jitter (Ciocchi et al., 2015), which poses the same problems as latency. I decided to use a combination of both latency and jitter and use neurons activated in the contralateral hemisphere as reference. Since I could not observe any mCherry$^+$ neurons around tetrode tips in the contralateral hemisphere with a confocal microscope, it is safe to assume that all these neurons are at least one synapse downstream of ChR2$^+$ terminals. For this initial step I pooled all cells from both groups together, including interneurons. As seen in Figure 11 A, the two parameters overlap, with the contralateral neurons being shifted towards higher values. As threshold for neurons that are likely to be activated directly by the laser I chose the 95th percentile of each distribution, which resulted in 2.275 ms for latency and 0.7 ms for jitter (blue perpendicular lines in Figure 11 A). An additional threshold was set for neurons with low jitter, to limit the activation latency to 4 ms. After this selection, I was left with 88 putative RE$^+$ neurons and 99 CB$^+$ neurons (55 and 72, respectively, after excluding FS interneurons). In this group of cells, CB$^+$ spatially selective neurons again constituted a significantly higher proportion of all CB$^+$ neurons, than in the RE$^+$ group (Figure 11 B, right, χ^2 test, χ^2 = 4.09, p = 0.04). However, this finding only mirrored the sampling of neurons, since activated spatially selected cells constituted a similar proportion of the total activated cells, as spatially-selective cells in the population of recorded neurons (RE$^+$ χ^2 test, χ^2 = 0.69, p = 0.40, CB$^+$ χ^2 test, χ^2 = 2.64, p = 0.10). Activated

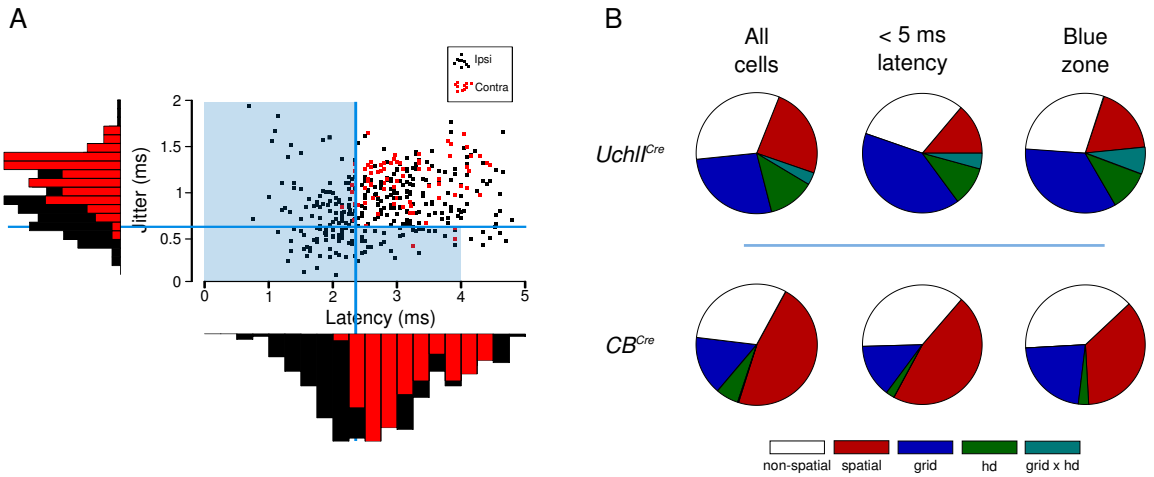

Figure 11. Activated excitatory neurons in *UchlI*^{Cre} and *CB*^{Cre} mice. A, Latency versus jitter plotted for all cells activated within 5 ms from laser onset pooled for the two groups. Blue lines show the thresholds used to select neurons directly activated by laser. **B,** Distribution of recorded putative excitatory neurons in *UchlI*^{Cre} (top row) and *CB*^{Cre} (bottom row) mice: left-hand side - all recorded neurons, middle - neurons activated at latency < 5 ms, right-hand side - putative RE$^+$ and CB$^+$ neurons, respectively (depicted in the blue shaded zone in **A**).

grid cells were similarly distributed in the two groups (Figure 11 B, lower panel, χ^2 test, $\chi^2 = 1.79$, $p = 0.18$), as were non-spatial neurons (Figure 11 B, lower panel, χ^2 test, $\chi^2 = 0.92$, $p = 0.33$). They too reflected the proportions in the sampled population (grid cells: RE$^+$ χ^2 test, $\chi^2 = 0.90$, $p = 0.34$, CB$^+$ χ^2 test, $\chi^2 = 1.57$, $p = 0.20$; non-spatial cells: RE$^+$ χ^2 test, $\chi^2 = 0.09$, $p = 0.76$, CB$^+$ χ^2 test, $\chi^2 = 1.52$, $p = 0.21$). These results suggest that RE$^+$ and CB$^+$ neurons have similar firing spatial patterns.

29 Functional characteristics of RE$^+$ and CB$^+$ neurons

Several studies have addressed differences between pyramidal and stellate cells in the MEC, directly or through predictions made based on a small sample of well characterized neurons (Burgalossi et al., 2011; Tang et al., 2014; Latuske et al., 2015; Sun et al., 2015). Results are conflicting and need further investigation.

29.1 Spatial firing properties

I first compared the mean firing rate, peak firing rate and information score of putative RE^+ and CB^+ neurons for the different functional classes. All values were similar for the three excitatory cell types (grid cells, spatially selective cells and non-spatial cells), except for the mean firing rate of grid cells and the information score of non-spatially selective neurons (Figure 12, Wilcoxon rank sum test, mean firing rate: grid cells W = 226, p = 0.013, spatial cells W = 164, p = 0.24, non-spatial W = 302, p = 0.058; peak firing rate: grid cells W = 128, p = 0.24, spatial cells W = 161, p = 0.47, non-spatial W = 293, p = 0.09; information score: grid cells W = 152, p = 1, spatial cells W = 119, p = 0.71, non-spatial W = 135, p = 0.02). The difference in information score between non-spatially selective cells does not come in conflict with their 'non-spatially selective' status, since it was shown that even fast spiking interneurons carry spatial information, albeit very low (Buetfering et al., 2014). In the total population of recorded grid cells, the mean firing rate did not differ between the two groups (Wilcoxon rank sum test, W = 6643, p = 0.31, RE^+: 2.72 ± 0.23, CB^+: 2.55 ± 0.34), which make it less likely that the difference in grid cell firing rate stems from the sampling of cells. However, it should be noted that the number of grid cells is rather small. A descriptor specific for grid cells, namely the grid score, was also similar for the two grid cell groups (Wilcoxon rank sum test, W = 180, p = 0.36, RE^+: 1.05 ± 0.05, CB^+: 0.98 ± 0.06).

29.2 Spike wave form and inter-spike intervals

It was previously reported that excitatory neurons in the MEC can be assigned to two groups, based on their spike time firing properties, i.e. bursty and non-bursty, and that they also differ in their spike wave form (Latuske et al., 2015). Furthermore, the group to which a neuron belonged could be a predictor for its spatial firing pattern and post-synaptic targets. I therefore tested whether RE and CB are more likely to be bursty or non-bursty neurons.

First, I performed the burstiness analysis on my dataset (all putative excitatory neurons recorded in both hemispheres, n = 2119) and obtained results that resemble what we previously reported (Latuske et al., 2015) (Figure 13 A, B). Namely, cells can be separated in two clusters, based on principal component analysis of the first 12 ms of their autocorrelation. These take a C-shape appearance when plotting their first three principal components. Putatively directly activated neu-

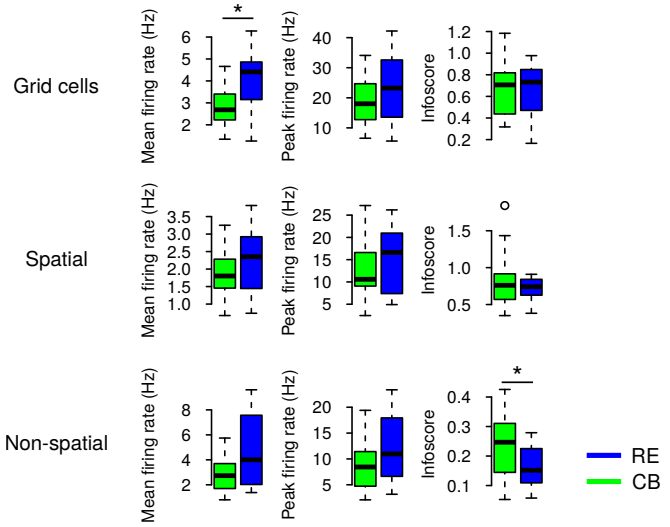

Figure 12. Firing properties of RE⁺ (blue) and CB⁺ (green) neurons. Mean firing rate, peak firing rate and information score for grid cells (top row), spatially selective cells (middle row) and cells without spatial selectivity (bottom row). The horizontal bar, the box, and the whiskers represent the median, the interquartile range, and the range, respectively. *p<0.05

rons followed the same C-shaped distribution (Figure 13 C, n = 187). However, when accounting for the marker expression, neurons were similarly distributed within the two clusters (Figure 13 D, χ^2 test, χ^2 = 0.07, p = 0.40; bursty/non-bursty: RE⁺ 31/24 neurons, CB⁺ 47/25 neurons). Within the group of grid cells, 15 RE⁺ and 13 CB⁺ were bursty, and 4 RE⁺ and 3 CB⁺ were non-bursty (Figure 13 F, χ^2 test, $\chi^2 = 4.5*10^{-31}$, p = 1; mean burstiness, Wilcoxon rank sum test, W = 180, p = 0.36). The distribution of bursty and non-bursty grid cells was reflected also in the similar spike wave form (Figure 13 E, Wilcoxon rank sum test, spike amplitude W = 124, p = 0.36; spike duration W = 92, p = 0.06; spike asymmetry W = 197, p = 0.14). I obtained similar results for spatially selective cells, with a high proportion in both RE⁺ and CB⁺ being bursty, and similarly distributed in the two groups (Figure 13 G, bursty: RE⁺ 9, CB⁺ 17; non-bursty RE⁺ 1, CB⁺ 9, χ^2 test, χ^2 = 2.18, p = 0.13, burstiness; Wilcoxon rank sum test, W = 170, p = 0.16). Again, spike wave form was similar for the two groups (Figure 13 H, Wilcoxon rank sum test, spike amplitude W = 124, p = 0.36; spike duration W = 160, p = 0.3; spike asymmetry W = 136, p = 0.84). The third category of excitatory neurons, non-spatial cells, comprised, as previously reported, similar proportions of bursty and non-bursty neurons, but here again RE and CB were no predictors for one or the other (Figure 13 J, bursty: RE⁺ 7, CB⁺ 16; non-bursty RE⁺ 9, CB⁺ 12, χ^2 test, χ^2 = 0.29, p = 0.50, burstiness; Wilcoxon rank sum test, W = 190, p = 0.29). Spike wave form did not differ for RE⁺ and CB⁺ neurons (Figure 13 I, Wilcoxon rank sum

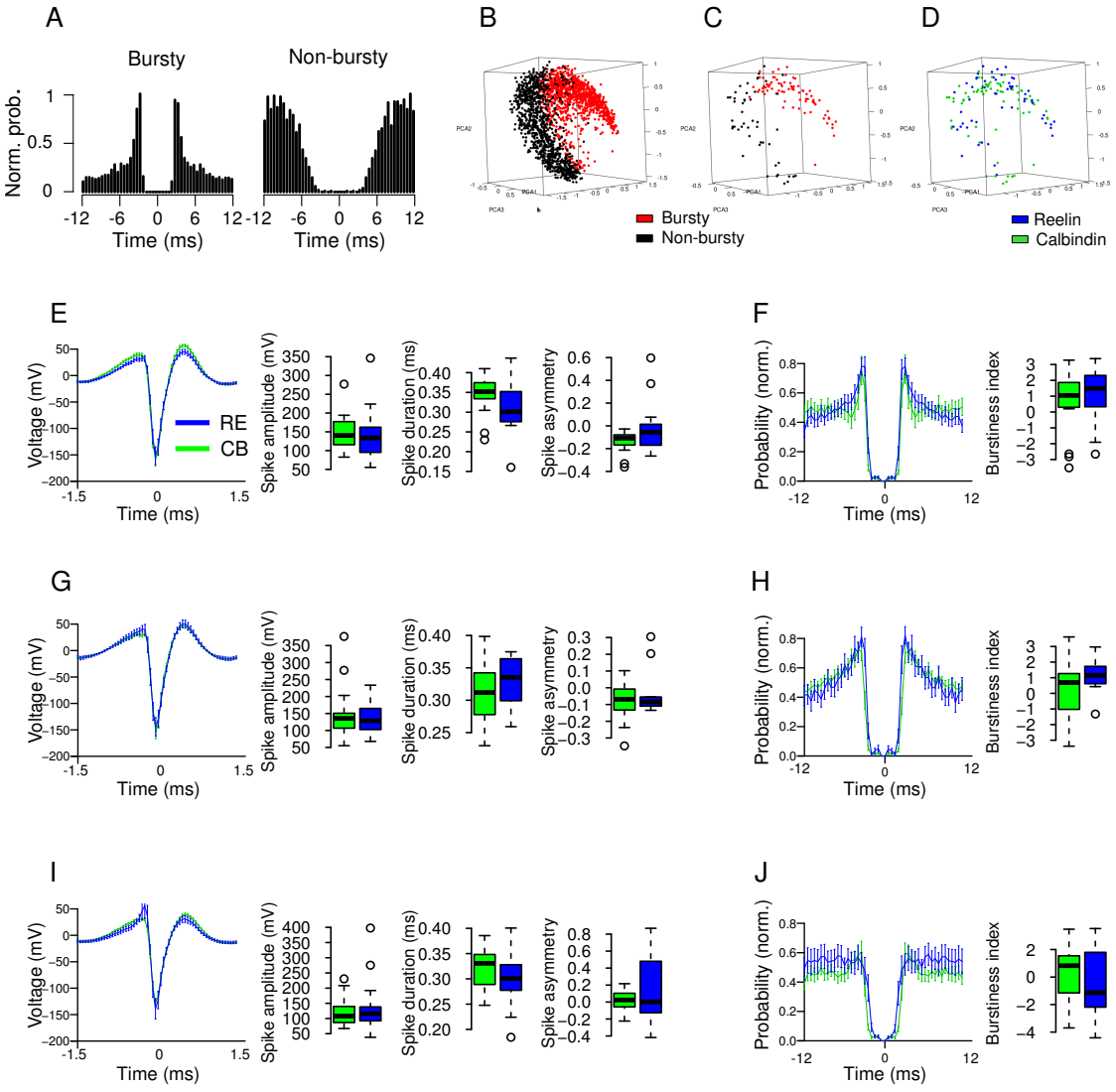

Figure 13. Burstiness, spike wave form and spiketime autocorrelation of RE⁺ and CB⁺ neurons. **A,** Example of autocorrelations for one bursty and one non-bursty neuron. **B,** 3D scatter plot of the first three principal components, with color coded cluster membership (red - bursty, black - non-bursty). **C,** Same as **B**, for all laser activated neurons. **D,** 3D scatter plot of the first three principal components, with the color corresponding to the expressed marker (blue - RE, green - CB). **E, G and I,** Average spike wave form, spike amplitude, spike duration, and spike asymmetry for grid cells, spatially selective cells and non-spatial cells, respectively. **F, H and J,** Average spike time autocorrelation and burstiness score for grid cells, spatially selective cells and non-spatial cells, respectively. In box-plots, the horizontal bar, the box, and the whiskers represent the median, the interquartile range, and the range, respectively.

test, spike amplitude W = 241, p = 0.69; spike duration W = 165, p = 0.15; spike asymmetry W = 230, p = 0.89).

These results confirm previous findings indicating that grid cells and spatially selective cells are much more likely to be bursty than non-bursty, while non-spatial cells are equally likely to be one or the other (Latuske et al., 2015), and furthermore show that RE^+ and CB^+ neurons are as likely to fire bursts of spikes at high frequency *in vivo*.

29.3 Speed modulation

It is well known that cells in the hippocampus and in the medial entorhinal cortex increase their firing rate when the animal's running speed increases (McNaughton et al., 1983; Sargolini et al., 2006; Kropff et al., 2015). A recent study showed, using calcium imaging *in vivo*, that the firing of $CB^+/Wfs1^+$ neurons is more strongly correlated to the animal's running speed than the firing of RE^+ neurons (Sun et al., 2015). I therefore wanted to test this observation on my data set. I obtained the speed scores of all cells, as the correlation coefficient of firing rate against running speed. The two grid cell groups had similar average speed correlation coefficients (Figure 14 A, RE^+ 0.12 $\pm$ 0.02, CB^+ 0.11 $\pm$ 0.01, Wilcoxon rank sum test, W = 165, p = 0.68). The same holds true for spatially selective (Figure 14 B, RE^+ 0.06 $\pm$ 0.02 , CB^+ 0.07 $\pm$ 0.01, Wilcoxon rank sum test, W = 119, p = 0.71) and for non-spatial neurons (Figure 14 C, RE^+ 0.09 $\pm$ 0.04 , CB^+ 0.03 $\pm$ 0.02, Wilcoxon rank sum test, W = 270, p = 0.27).

The above mentioned study found that the firing of a much larger proportion of $CB^+/Wfs1^+$ is significantly correlated to the running speed, when compared to RE^+ neurons. Therefore, I obtained a speed score threshold from a shuffled distribution, as the 99^{th} percentile of this distribution. This threshold was 0.07, and cells that had a score higher than the threshold were considered significantly speed modulated. 14/19 RE^+ grid cells and 13/16 CB^+ neurons passed the threshold for speed modulation, and their proportions were similar in their respective groups (χ^2 test, χ^2 = 0.016, p = 0.89). The steepness of their speed modulation slope did not differ (Figure 14 A, Wilcoxon rank sum test, W = 115, p = 0.25). The same held true for spatially selective neurons, where 4/10 RE^+ and 13/26 CB^+ neurons were significantly speed modulated (Figure 14 B, χ^2 test, χ^2 = 0.02, p = 0.86; speed slope: Wilcoxon rank sum test, W = 41, p = 0.1), and for non-spatial

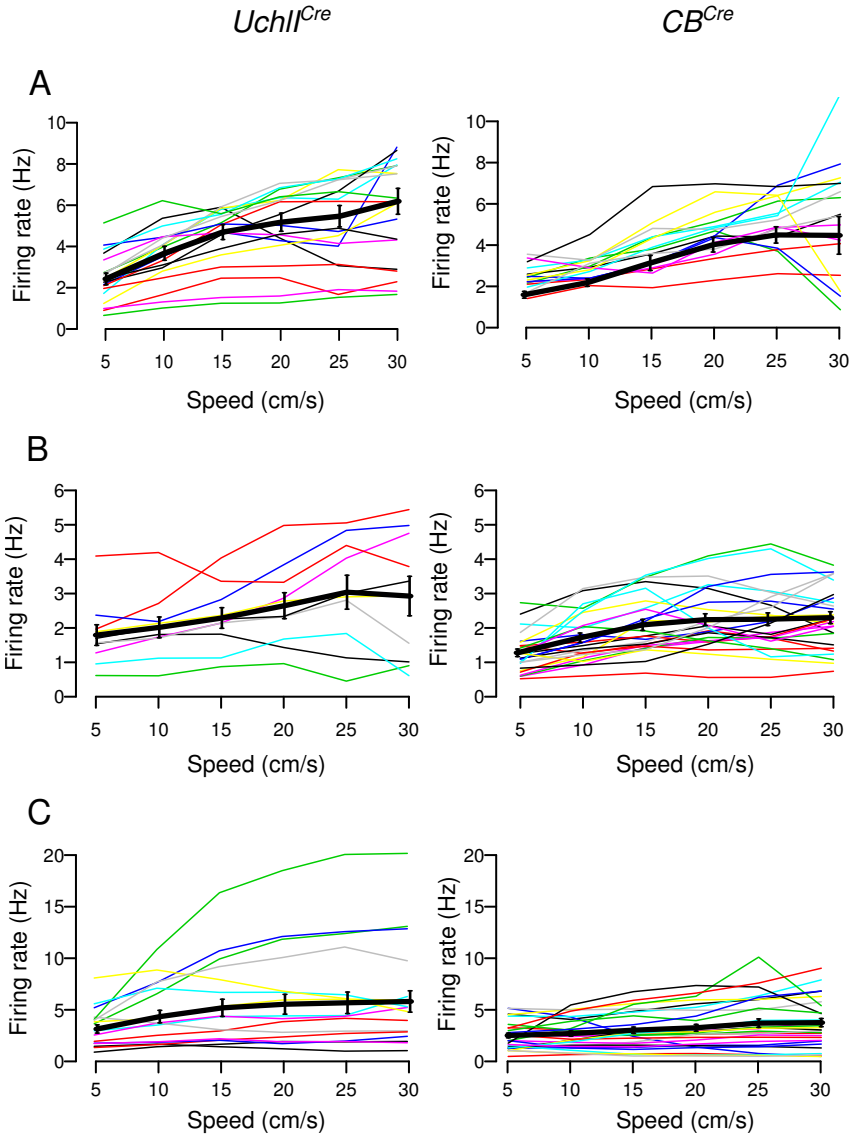

Figure 14. Speed modulation in RE⁺ (in *Uchl1*^{Cre} mice) and CB⁺ (in *CB*^{Cre}) neurons. **A,** Firing rate as a function of speed of all individual grid cells (coloured lines) and superimposed average (thick black line) for RE⁺ (lef-hand side) and CB⁺ (right-hand side) neurons. **B,** Same as (**A**), for spatially selective neurons. **C,** Same as (**A**), for non-spatial neurons.

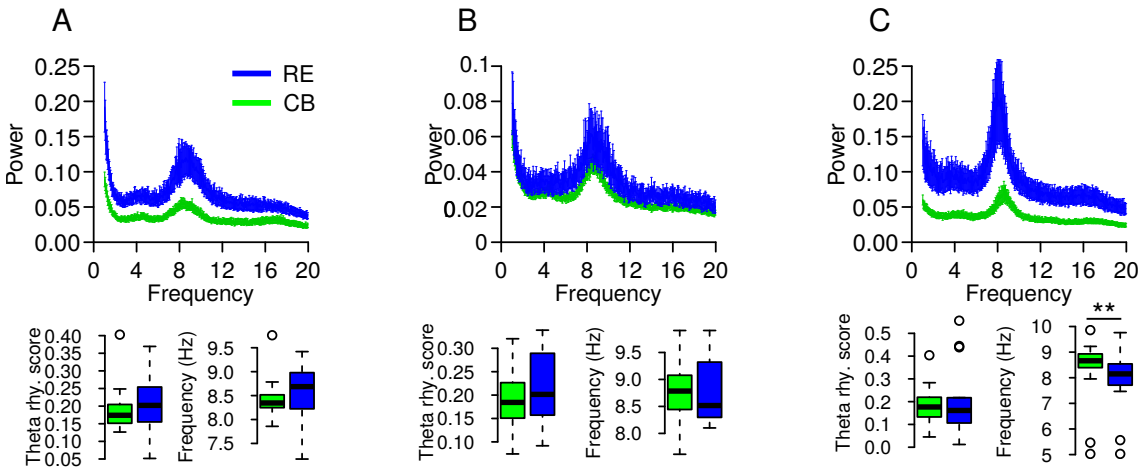

Figure 15. Intrinsic cell oscillations in RE⁺ and CB⁺ neurons. **A,** Top: averaged power spectrum of the instantaneous firing rate for grid cells. Bottom: theta rhythmicity score and peak frequency of the power spectrum shown on top. **B,** Same as (**A**), for spatially selective neurons. **C,** Same as (**A**), for non-spatial neurons. In box-plots the horizontal bar, the box, and the whiskers represent the median, the interquartile range, and the range, respectively.*p < 0.05, **p < 0.01

neurons, with 10/16 RE⁺ and 10/28 CB⁺ speed modulated cells (Figure 14 C, χ^2 test, $\chi^2 = 1.95$, $p = 0.16$; speed slope: Wilcoxon rank sum test, $W = 67$, $p = 0.21$).

29.4 Intrinsic cell oscillations

Neurons in the MEC have been shown to exhibit both sub-threshold membrane voltage potential oscillations (Giocomo and Hasselmo, 2009; Domnisoru et al., 2013) and a spike time rhythmicity, that becomes apparent in the spike-time autocorrelation as peaks roughly 125 ms apart (corresponding to 7-8 Hz theta oscillations) (Brun et al., 2008b; Mizuseki et al., 2009). These oscillations are thought to support navigation and memory (Buzsáki and Moser, 2013). It can occur that grid cells recorded on the same tetrode have very different degrees of theta modulation (Latuske et al., 2015). I tested whether cells expressing RE and CB differ in the degree of theta modulation. I calculated a theta rhythmicity score based on the power spectrum of the instantaneous firing rate. RE⁺ grid cells had a similar theta rhythmicity score to CB⁺ grid cells (Figure 15 A, Wilcoxon rank sum test, $W = 179$, $p = 0.38$). Also, the peak power was present at a similar frequency (Wilcoxon rank sum test, $W = 180$, $p = 0.36$). Spatially selective cells were similar in both the strength of theta modulation and the peak frequency (Figure 15 B, Wilcoxon rank sum test, theta rhythmicity score $W = 154$, $p = 0.41$; peak frequency of the

power spectrum of the instantaneous firing rate W = 117.5, p = 0.167), as were non-spatial neurons (Figure 15 C, Wilcoxon rank sum test, theta rhythmicity score W = 217, p = 0.87; peak frequency of the power spectrum of the instantaneous firing rate W = 108, p = 0.0047). These results suggest that RE^+ and CB^+ exhibit similar rhythmicity.

29.5 Phase locking to the LFP theta oscillations

In the MEC, the firing probability of many neurons is locked to the phase of local theta oscillations (Brun et al., 2008a; Hafting et al., 2008; Quilichini et al., 2010; Burgalossi et al., 2011; Latuske et al., 2015; Ebbesen et al., 2016). Specifically, most neurons have an increased firing probability near the trough of the theta cycle. A measure of how regular the firing of a neuron is in respect to external theta oscillations is the theta vector length. In my data set, all three cell types had similar theta phase locking strengths, and I could observe no difference between RE^+ and CB^+ neurons (Figure 16, Wilcoxon rank sum test, grid cells W = 155, p = 0.9349, spatially selective cells W = 119, p = 0.7152, non-spatial cells W = 193, p-value = 0.461).

Different neuronal classes exhibit a propensity to fire locked to a specific theta phase (Tang et al., 2014; Latuske et al., 2015). My data set is unfortunately too small to accurately perform such an analysis. Estimating the mean firing phase in a theta cycle would additionally require neurons with a large theta vector length. Nonetheless, it is possible that a strong, reliable difference could be detected also using a small sample. I calculated the circular mean of all grid cells and used a permutation test to asses the difference between means. These were not different (RE^+, n = 19, circular mean 11.84 $\pm$ 13.81°; CB^+, n = 16, 44.64 $\pm$ 36.26°, p = 0.10), even after selection of neurons with a theta vector length > 0.2 (RE^+, n = 5, 42.2 $\pm$ 12.04°; CB^+, n = 4, 50.06 $\pm$ 78.48°, p = 0.38). The mean theta phases for spatially selective cells were also similar (all neurons: RE^+, n = 10, 45.87 $\pm$ 14.43°; CB^+, n = 26, 47.66 $\pm$ 7.77°, p = 0.45; for cells with vector length > 0.2: RE^+, n = 7, 56.54 $\pm$ 15.96°; CB^+, n =21, 50.44 $\pm$ 8.09°, p = 0.60), as for non-spatial neurons (all neurons: RE^+, n = 16, 53.78 $\pm$ 14.19°; CB^+, n = 28, 64.49 $\pm$ 17.05°, p = 0.24; for cells with vector length > 0.2: RE^+, n = 10, 69.90 $\pm$ 17.84°; CB^+, n = 23, 70.60 $\pm$ 11.22°, p = 0.48). Although these values should be taken with caution, they do show a trend: most neurons fire on the descending phase of the theta cycle, close to the trough.

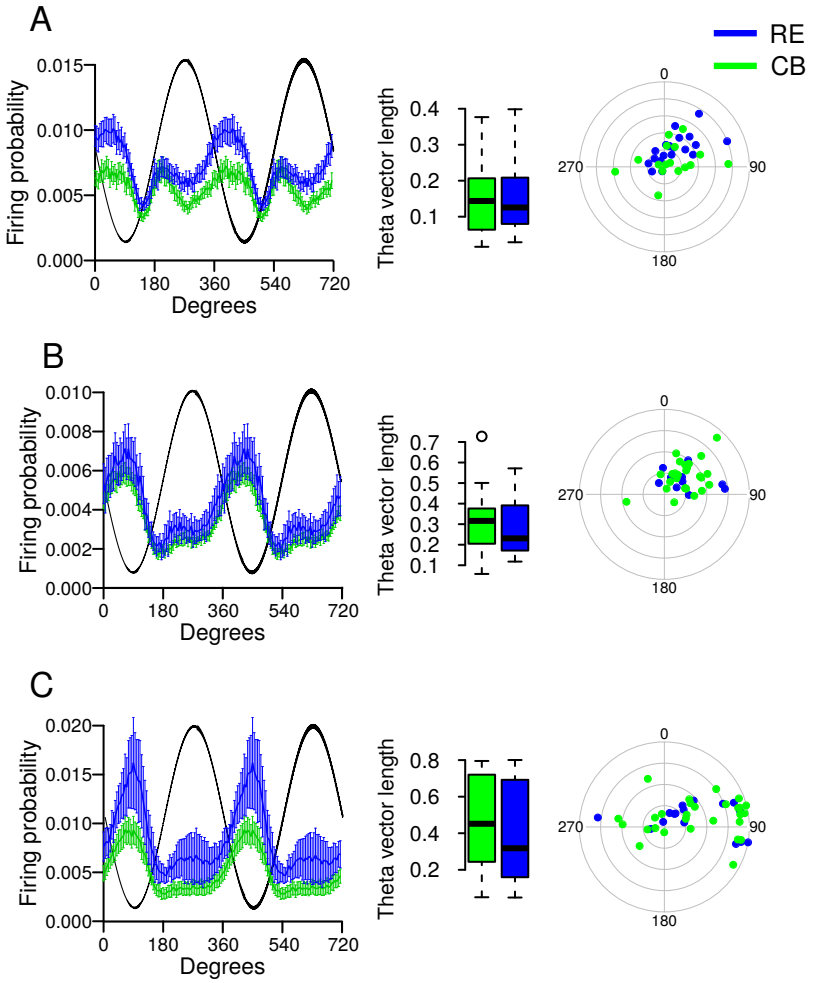

Figure 16. RE⁺ and CB⁺ neurons are locked to the external theta phase. A, Firing rate as a function of theta cycle phase, shown for grid cells, for two theta cycles. The black trace is a filtered theta oscillation. Theta vector length. Plot of the circular mean for all grid cells (preferred phase), with the distance from the center being equal to the vector length for that cell (0-0.45). **B,** Same as (**A**), for spatially selective neurons. Vector length interval was 0-0.8. **C,** Same as (**A**), for non-spatial neurons.Vector length interval was 0-0.8. In box-plots the horizontal bar, the box, and the whiskers represent the median, the interquartile range, and the range, respectively.

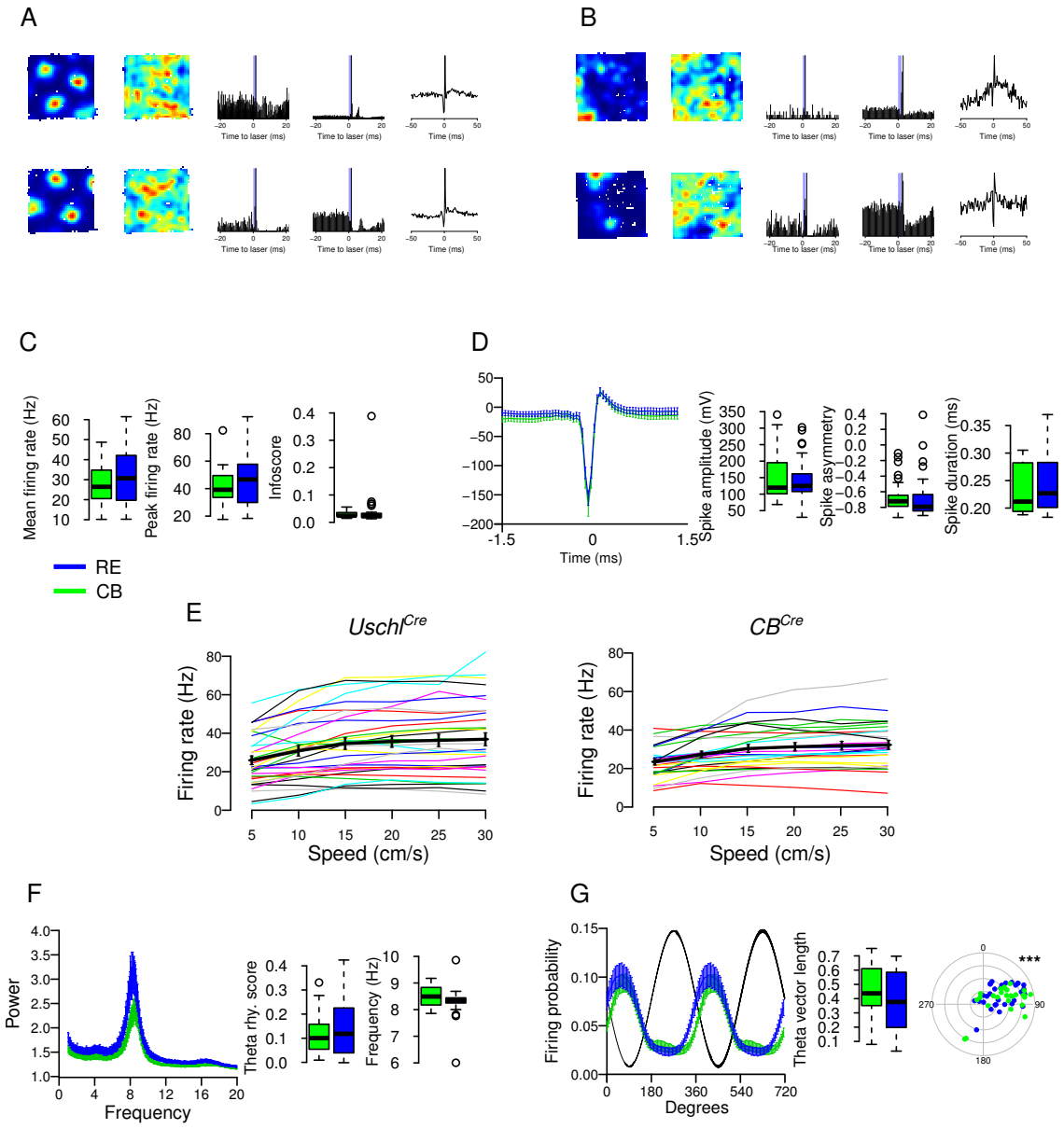

Figure 17. Interneurons activated at low latency.. **A,** Color coded firing rate maps of putative RE$^+$ neurons (in this case grid cells) and their post-synaptic targets (FS interneurons). Spike-time versus laser onset cross-correlation for the same cells, and spike-time cross-correlation of the two cells, showing a peak at low latency. Neurons were recorded in a *Uschl*^{Cre} mouse. **B,** Same as (**A**), recorded in a *CB*^{Cre} mouse. **C,** Mean firing rate, peak firing rate, and information score for the two interneuron populations. **D,** Averaged spike wave form, with quantification of spike amplitude, duration, and asymmetry. **E,** Firing rate as a function of speed of all interneurons (colored lines) and superimposed average (thick black line) in *Uschl*^{Cre} (left-hand side) and *CB*^{Cre} (right-hand side) mice. **F,** Averaged power spectrum of the instantaneous firing rate, theta rhythmicity score and peak frequency of the power spectrum shown on the right. **G,** Firing rate as a function of theta cycle phase shown for two theta cycles. The black trace is a filtered theta oscillation. Theta vector length. Plot of the circular mean for all grid cells (preferred phase), with the distance from the center being equal to the vector length of that cell (0-0.8). In box-plots the horizontal bar, the box, and the whiskers represent the median, the interquartile range, and the range, respectively. ***p<0.0001.

29.6 Interneurons activated at low latency and jitter

The vast majority (over 95%) of RE^+ and CB^+ neurons in the MEC were reported to be non-γ-aminobutyric acid (GABA)-ergic (Varga et al., 2010). Despite this fact, in my data roughly one third of the neurons that fell into the category of putatively directly activated neurons were FS neurons (33 of 88 putative RE^+ neurons and 27 out of 99 CB^+ neurons, χ^2 test, χ^2 = 1.79, p = 0.18). Therefore, I believe that the interneurons considered in this analysis are probably a mix of RE^+, CB^+ and post-synaptic targets (probably one synapse downstream) of $ChR2^+$ neurons (Figure 17 A and B). For simplicity, I will continue to refer to the two groups as RE^+ and CB^+. The populations of FS in the two groups were similar in respect to mean and peak firing rate, as well as information score (Figure 17 C, Wilcoxon rank sum test, mean firing rate W = 493, p = 0.48, peak firing rate W = 536, p = 0.18, information score W = 361, p = 0.21). The spike wave forms were similar in amplitude, duration, and asymmetry (Figure 17 D, Wilcoxon rank sum test, spike amplitude W = 460, p = 0.83, spike duration W = 491, p = 0.50, spike asymmetry W = 390, p = 0.41). On average, the speed correlation was similar in the two groups (Wilcoxon rank sum test, W = 457, p = 0.87), with 24/33 RE^+ and 18/27 CB^+ FS neurons fulfilling the criterion for speed modulated neurons (Figure 17 E, χ^2 test, χ^2 = 0.05, p = 0.82, speed slope Wilcoxon rank sum test, W = 256, p = 0.31). Both groups exhibited a clear peak in the power spectrum of the instantaneous firing rate, having similar power and at similar frequency (Figure 17 F), Wilcoxon rank sum test, theta rhythmicity score W = 461, p = 0.8249; peak frequency of the power spectrum of the instantaneous firing rate W = 331, p = 0.09). Neurons in both groups were phase locked to LFP theta oscillations (Wilcoxon rank sum test, theta vector length W = 372, p = 0.2803). The mean theta phase in the two groups was significantly different (RE^+, n = 33, circular mean 57.11 $\pm$ 8.30°; CB^+, n = 27, 68.37 $\pm$ 10.07°, p = 0.0038; neurons with a theta vector length > 0.2 RE^+, n = 24, 63.44 $\pm$ 7.25°; CB^+, n = 23, 75.10 $\pm$ 8.20°, p = 0.0006), with RE^+ interneurons firing on average ~10° earlier (~3.5 ms) than their CB^+ counterparts (Figure 17 G). These results suggest that both RE^+ and CB^+ neurons comprise of and strongly activate FS neurons that are very similar, apart from their spike timing in respect to the local theta oscillations.

30 Contralateral targets of CB^+ and CB^-/WFS^+ neurons

As mentioned in the first part of this chapter, following expression of ChR2 in neurons of the right hemisphere, neurons can be activated in the left hemisphere either through stimulation of cell bodies in the injection site, or through activation of axon terminals in the contralateral side. Only cells activated by local laser stimulation were analyzed, in order to exclude the possibility of the signal coming via a different brain region (e.g. the hippocampus). These neurons were activated on average with a latency of 3.073 ms in *Uchl1*^{Cre} mice and 3.001 ms in *CB*^{Cre} mice (Wilcoxon rank sum test, W = 277.5, p = 0.6597) and a jitter of 1.134 and 1.178 ms, respectively (Figure 18 A, Wilcoxon rank sum test W = 283, p = 0.74). In the two populations, interneurons constituted a majority of cells, with CB^+ neuron targets comprising significantly more interneurons than the parasubicular ($Wfs1^+/RE^-/CB^-$) targets (Figure 18 B, χ^2 test, χ^2 = 9.33, p = 0.0022). Non-spatial neurons were found in similar proportions (χ^2 test, χ^2 = 1.72, p = 0.18), while spatially selective neurons (including grid cells, HD cells and irregular spatially selective) made up a higher proportion of neurons within the parasubicular targets (χ^2 test, χ^2 = 4.69, p = 0.03). The target interneurons had similar firing properties (Figure 18 C, Wilcoxon rank sum test, mean firing rate W = 202, p = 0.9, peak firing rate W = 204, p = 0.92, information score W = 177, p = 0.44). Spike wave form properties were not different (Wilcoxon rank sum test, spike amplitude: *Uchl1*^{Cre} 174.70 $\pm$ 13.99 mV, *CB*^{Cre} 194.1 $\pm$ 16.21 mV, W = 188, p = 0.63; spike duration: *Uchl1*^{Cre} 0.27 $\pm$ 0.01 ms, *CB*^{Cre} 0.25 $\pm$ 0.01 ms, W = 248, p = 0.29; spike asymmetry: *Uchl1*^{Cre} -0.73 $\pm$ 0.03, *CB*^{Cre} -0.73 $\pm$ 0.04, W = 219, p = 0.76). The proportion of speed modulated interneurons was similar in the two groups (11/18 and 11/23, respectively, χ^2 test, χ^2 = 0.28, p = 0.59) and the speed slope did not differ (Wilcoxon rank sum test, *Uchl1*^{Cre} 0.42 $\pm$ 0.05, *CB*^{Cre} 0.70 $\pm$ 0.16, W = 51, p = 0.56). These results show that targeted contralateral interneurons are likely to be similar for $Wfs1^+/CB^-/RE^-$ parasubicular contralateral projections and the $CB^+/Wfs1^+$ MEC projections. Furthermore, they suggest that an important function of these projections is to inhibit the contralateral MEC.

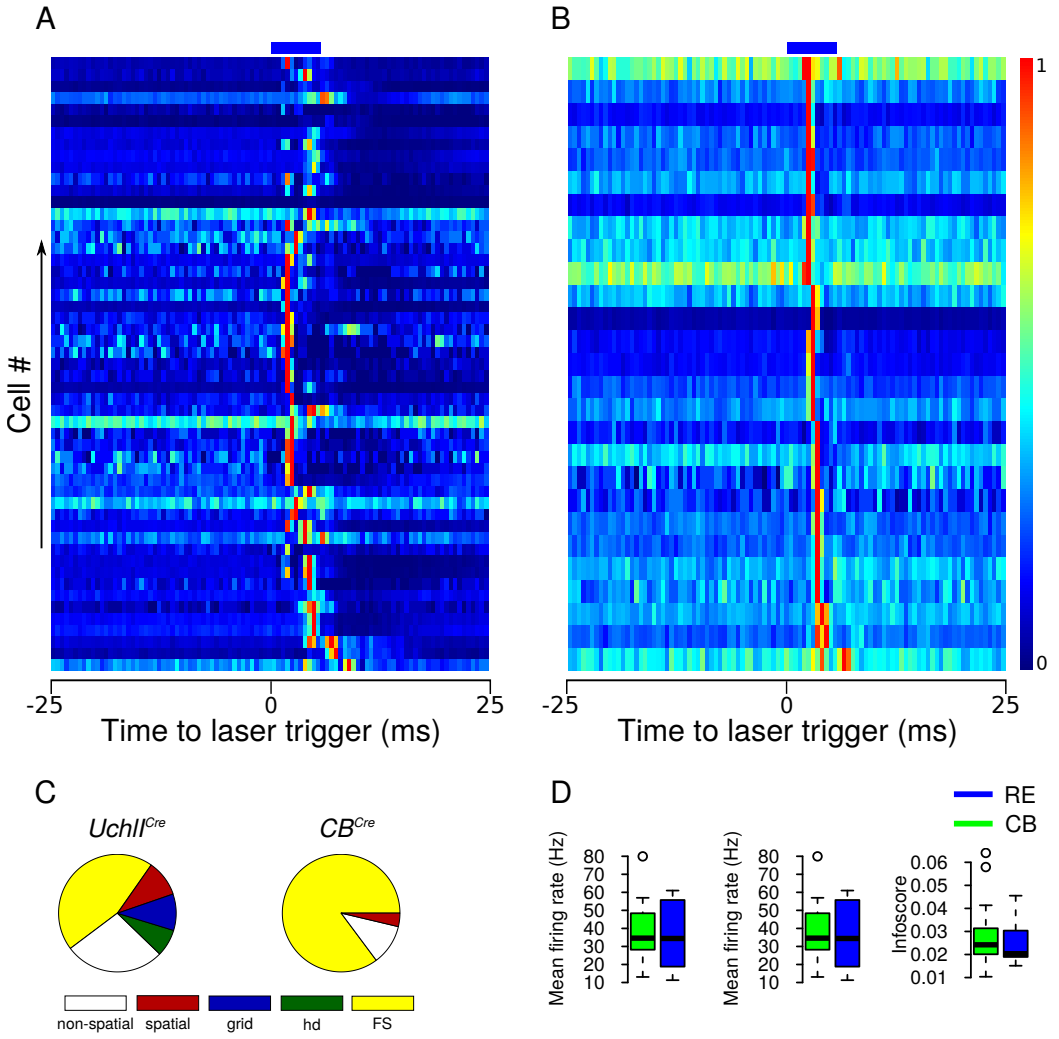

Figure 18. Neurons activated in the contralateral MEC following laser stimulation of ChR2⁺ axon terminals.. **A,** Laser cross-correlations of all cells activated within 5 ms from laser onset in the contralateral hemisphere (blue rectangle on top of the picture) in *UchlI*^{Cre} mice. Each line represents a cell, with each bin (0,5 ms) normalized to the bin with the highest number of spikes for that cell. **B,** The same representation for cells recorded in *CB*^{Cre} mice. **C,** Proportion of activated cell types. **D,** Mean firing rate, peak firing rate, and information score for the activated FS neurons. In D, the horizontal bar, the box, and the whiskers represent the median, the interquartile range, and the range, respectively.

Chapter VIII - Functional identity of anatomically defined MEC neurons - Discussion

The results I obtained using *UchlII*^{Cre} and *CB*^{Cre} suggest that the firing of stellate and pyramidal cells *in vivo* does not differ significantly with respect to firing rate and spatial selectivity. These data question previously reported results in mice and rats that suggested functional segregation of these cell types (Burgalossi et al., 2011; Sun et al., 2015; Ebbesen et al., 2016). My data also suggest that functional neuronal types do not map onto anatomically and electrophysiologically defined cell types (Alonso and Köhler, 1984; Canto and Witter, 2012; Fuchs et al., 2016).

31 RE^{+} and CB^{+} neurons belong to similar functional populations

The anatomical organization of the MEC, with its three (or five) morphologically defined cell types (stellate, pyramidal, oblique pyramidal and two intermediary types) (Canto and Witter, 2012; Fuchs et al., 2016) raises the question whether functionally different cell types correspond to these morphologies and the respective anatomical segregation within the MEC. In vitro, several electrophysiological properties (like inter-spike interval, sag potential, latency to first spike) and marker expression differ markedly between the aforementioned cell types (Alonso and Köhler, 1984; Canto and Witter, 2012; Fuchs et al., 2016). However, my data confirm the results of Sun and colleagues (Sun et al., 2015), who found that all firing spatial patterns are similarly represented in the two groups, and challenge previous results that indicate a greater prevalence of grid cells in the CB^{+} population

(Tang et al., 2014).

In the current data set, I was also not able to detect differences in spike wave form between RE^+ and CB^+ neurons, in contrast to *in vitro* features (Fuchs et al., 2016). This discrepancy might arise from the lack of tetrode recording sensitivity (the differences detected by Fuchs and colleagues were in the range of 1 - 2 mV and recorded spikes *in vivo* have an amplitude of 50 - 250 µV). Alternatively, action potential wave form reveals features under conditions of current injection *in vitro* that remain hidden *in vivo*. Yet another possibility is the presence of additional ionic components in the neurons of behaving mice, that contribute to a change in action potential shape.

In vivo patch-clamp recordings, although they enable very precise measurements of action potential timing and sub-threshold membrane voltage potential have one major drawback: they are technically challenging, which usually limits the sampling of neurons to a few dozens (Burgalossi et al., 2011; Domnisoru et al., 2013; Tang et al., 2014). Tetrode recordings, while offering the possibility to record from up to tens of neurons simultaneously (Stensola et al., 2012), have issues related to precise recording site identification and the accuracy of spike detection and sorting. Therefore, one possibility would be that extracellular, as opposed to intracellular recordings (Ebbesen et al., 2016), cannot pick up fine differences in spike wave form. The position of the tetrode tip and the noise (due to movement and nearby cells spiking) can affect spike detection accuracy. However, it was shown that tetrodes can pick up not only great differences in spike duration, like the ones between fast-spiking interneurons and pyramidal cells (Henze et al., 2000), but also finer differences in the spike wave form of excitatory neurons (Senior et al., 2008; Latuske et al., 2015). These studies support the hypothesis that the results I obtained are reliable.

32 RE^+ and CB^+ neurons are similarly modulated by running speed

It was recently reported that the firing rate of CB^+ neurons correlates stronger with running speed, than that of RE^+ neurons (Sun et al., 2015). My data do not support these results. I could not detect a difference neither in the proportion of significantly speed modulated neurons, nor a generally stronger speed

correlation in one of the groups. Also, calcium signals could, hypothetically, also stem from sub-threshold calcium fluctuations that are not correlated with the cell spiking activity, but to incoming signals that activate for example ryanodine or inositol-1,4,5-triphosphate (IP_3) receptors and lead to the release of calcium from internal stores, such as the endoplasmic reticulum) (Verkhratsky, 2002; Bardo et al., 2006; Majewski and Kuznicki, 2014). Moreover, GCaMP itself acts as a calcium buffer and can thus disrupt endogenous firing patterns. The introduction of microendoscopes, as in Sun et al., 2015, leads to a bigger lesion of the dorsal and perirhinal, entorhinal and visual cortices that the implantation of tetrodes and may thus have stronger impact on inter-cortical signaling. By chance, this damage could be different in the very small experimental sample (having three mice per group). Further investigation is needed to determine which of the two scenarios holds true.

33 Fast spiking interneurons are present in both groups

Reports from *in vitro* and *in vivo* studies indicate that a subset of fast spiking inhibitory interneurons express RE or CB (Varga et al., 2010; Zhang et al., 2013; Fuchs et al., 2016). However, the percentage of positive neurons is presumably very low. In the present study, approximately one third of laser activated neurons were fast-spikers. This result can be explained by two observations: i) the detection of neurons is more sensitive to activation of cells with high firing rate; ii) interneurons receive input from a large number of excitatory cells (Couey et al., 2013; Buetfering et al., 2014; Fuchs et al., 2016), which means that they can potentially be activated very fast and strongly within 2-3 ms after laser onset, following laser activation of pre-synaptic cells (as shown by the low latency of peaks in cross-correlations of putatively connected neurons). Based on my analysis I can conclude that RE^+ and CB^+ fast spikers are similar, except for the spike timing in relation to the local theta oscillations. The difference in spike timing could reflect either differential local input onto interneurons, or differential inputs from other brain regions, like the medial septum (Gonzalez-Sulser et al., 2014).

34 Differences in axonal projections

As already shown, RE^+ stellate MEC neurons project strongly to the dentate gyrus of the hippocampus via the perforant path (Cajal, 1911). In contrast, studies on the projections of CB^+ pyramidal cells have yielded conflicting results. Namely, some studies find a projection to the ipsilateral hippocampus (CA1 region) (Kitamura et al., 2014; Sürmeli et al., 2015) and weak projections to the contralateral MEC (Kitamura et al., 2014), while others find only contralateral MEC projections (Varga et al., 2010; Fuchs et al., 2016). These data were obtained using different Cre driver mouse lines, where Cre recombinase is expressed either under the promoter for Wfs1, or for CB, respectively. Although the two markers have a high degree of overlap (Kitamura et al., 2014; Ray et al., 2014; Fuchs et al., 2016), it is probable that some $Wfs1^+/CB^-$ neurons project to the CA1. Alternatively, differences in injection coordinates might lead to distinct neuronal populations expressing ChR2. In my study, I find only contralateral CB^+ projections, that mostly target fast spiking interneurons in the contralateral MEC. Additionally, I discovered a new projection originating in the parasubiculum and targeting as well largely fast spiking interneurons, along with spatially selective and non-spatial neurons in the contralateral MEC. It was previously shown *in vitro* that CB^+ neurons excite neurons in LII of the contralateral MEC (Fuchs et al., 2016). *In vivo* however, I detected a vast majority of excitatory responses in interneurons, which suggests that the net effect on the network will be inhibitory. The role of these cross-hemispheric connections is still unknown and their function is only starting to be investigated. Eventually, silencing these axons might be a better approach to investigate the function of cross-hemispheric connections.

35 Technical limitations

Despite having taken precautions to avoid false positives in the detection of RE^+ and CB^+ neurons, a number of possible caveats threaten the validity of this endeavor. First, like in previous studies, a virus was used to over-express a new protein. The virus alone could change cellular function by interfering with protein metabolism. Further, it could be that some cell types are more susceptible than others to metabolic imbalances. Secondly, although the light intensity used in this study was very low compared to others (Kvitsiani et al., 2013; Buetfering et al.,

2014; Ciocchi et al., 2015) to minimize large extracellular currents, it is still possible that some synaptically activated neurons might have been treated as directly activated neurons (Muñoz et al., 2014). Also, the extracellular currents that arise through the opening of ChR2 could indirectly bring a cell to the spiking threshold, by minimizing the difference between the extracellular and intracellular potential. Therefore, future studies will have to confirm these results, before we can make statements regarding these cell types.

Concluding remarks

In this dissertation I used two different approaches to investigate the function of the medial entorhinal cortex. First I used a genetic mouse model to study the involvement of the MEC and the hippocampus in spatial navigation, and disentangle the role of grid versus place cells. Thus, *Cx36*$^{-/-}$ mice, with impaired place cell function, but intact grid cell activity and preserved path integration abilities, yielded data supporting the role of the MEC in self movement guided navigation.

Secondly, I used optogenetics to study both MEC local circuits, and interhemispheric connections. In the present dissertation, I did not find differences between two anatomically defined neuronal populations, expressing RE and CB, respectively. This is surprising, given *in vitro* results that convincingly show the existence of several cell classes. Furthermore, I discovered a previously unreported projection to the contralateral hemisphere stemming from the parasubiculum, and showed for the first time that this and the projections of CB^{+} pyramidal neurons activate mostly interneurons in the contralateral MEC, thus indirectly inhibiting neurons there. It remains to be seen how silencing these projections affects spatial coding and behavior.

Acknowledgements

The work I described in this dissertation is only a part of what I achieved in the last 4 years. All of this would not have been possible without the help of many people.

First and foremost, I would like to thank Hannah Monyer, who offered me the chance to learn and grow, both scientifically and personally. Thanks to her, I achieved technically very challenging things, like mouse brain surgery (and most importantly having the mice awake and well afterwards, and ready to let me record their brain signal while they were running around), using lasers to activate neurons in their entorhinal cortices, and fancy data analysis. For this and her support inside and outside the lab, I will always be grateful.

Special thanks go to all the in vivos! For all the lunch-break talks, for bearing with me when I was unbearable and giving me the feeling that there is always someone to turn to. Firstly, I want to thank Kevin Allen, who shared with me his knowledge of everything related to in vivo recordings (and mountain biking). I would like to thank Olga and Magda from the bottom of my heart for being there for me and offering their support in these last few months. Patrick deserves extra-special thanks for help with experiments, programming and computer trouble shooting.

I would like to thank Laura Winkel for help with administrative things (and not only!), Anne Herb for organizing the mouse breeding, Antonio Caputi and Angela Neitz for help with experiments and fruitful discussion, Ella Savenkova for support, Eric for fruitful discussion, José for insightful talks on psychology, Ulla for technical help and discussion, Michi and Roberta for helping me obtain information.

My life in Heidelberg was made easy and carefree thanks to some very special people, who did not give up on me, despite my obsession for work. My dearest Cornelius and his family who almost adopted me, Wasja, Tanja, Nelly, Vero, and many others, they all reminded me that there is a life beyond the bench (or setup... or computer...).

Bibliography

Allen, K., Fuchs, E. C., Jaschonek, H., Bannerman, D. M., and Monyer, H. (2011). Gap junctions between interneurons are required for normal spatial coding in the hippocampus and short-term spatial memory. *The Journal of Neuroscience*, 31(17):6542–6552.

Allen, K., Gil, M., Resnik, E., Toader, O., Seeburg, P., and Monyer, H. (2014). Impaired Path Integration and Grid Cell Spatial Periodicity in Mice Lacking GluA1-Containing AMPA Receptors. *The Journal of Neuroscience*, 34(18):6245–59.

Alonso, A. and Klink, R. (1993). Differential electroresponsiveness of stellate and pyramidal-like cells of medial entorhinal cortex layer II. *Journal of Neurophysiology*, 70(1):128–143.

Alonso, A. and Köhler, C. (1984). A study of the reciprocal connections between the septum and the entorhinal area using anterograde and retrograde axonal transport methods in the rat brain. *The Journal of Comparative Neurology*, 225(3):327–43.

Alyan, S. and McNaughton, B. L. (1999). Hippocampectomized rats are capable of homing by path integration. *Behavioral neuroscience*, 113(1):19–31.

Annese, J., Schenker-Ahmed, N. M., Bartsch, H., Maechler, P., Sheh, C., Thomas, N., Kayano, J., Ghatan, A., Bresler, N., Frosch, M. P., Klaming, R., and Corkin, S. (2014). Postmortem examination of patient H.M.'s brain based on histological sectioning and digital 3D reconstruction. *Nature Communications*, 5:3122.

Bardo, S., Cavazzini, M. G., and Emptage, N. (2006). The role of the endoplasmic reticulum Ca2+ store in the plasticity of central neurons.

Barretto, R. P. J. and Schnitzer, M. J. (2012). In vivo microendoscopy of the hippocampus. *Cold Spring Harbor Protocols*, 7(10):1092–1099.

Barry, C., Ginzberg, L. L., O'Keefe, J., and Burgess, N. (2012). Grid cell firing patterns signal environmental novelty by expansion. *Proceedings of the National Academy of Sciences*, 109(43):17687–92.

Beed, P., Bendels, M. H. K., Wiegand, H. F., Leibold, C., Johenning, F. W., and Schmitz, D. (2010). Analysis of Excitatory Microcircuitry in the Medial Entorhinal Cortex Reveals Cell-Type-Specific Differences. *Neuron*, 68(6):1059–1066.

Belousov, A. B. and Fontes, J. D. (2012). Neuronal gap junctions: making and breaking connections during development and injury. *Trends in Neurosciences*, 36(4):227–236.

Blair, H. T., Cho, J., and Sharp, P. E. (1998). Role of the lateral mammillary nucleus in the rat head direction circuit: A combined single unit recording and lesion study. *Neuron*, 21(6):1387–1397.

Blair, H. T. and Sharp, P. E. (1995). Anticipatory head direction signals in anterior thalamus: evidence for a thalamocortical circuit that integrates angular head motion to compute head direction. *The Journal of Neuroscience*, 15(9):6260–6270.

Boccara, C. N., Sargolini, F., Thoresen, V. H., Solstad, T., Witter, M. P., Moser, E. I., and Moser, M.-B. (2010). Grid cells in pre- and parasubiculum. *Nature Neuroscience*, 13(8):987–994.

Bonnevie, T., Dunn, B., Fyhn, M., Hafting, T., Derdikman, D., Kubie, J. L., Roudi, Y., Moser, E. I., and Moser, M.-B. B. (2013). Grid cells require excitatory drive from the hippocampus. *Nature Neuroscience*, 16(3):309–17.

Bostock, E., Muller, R. U., and Kubie, J. L. (1991). Experience-dependent modifications of hippocampal place cell firing. *Hippocampus*, 1(2):193–205.

Bragin, A., Jandó, G., Nádasdy, Z., Hetke, J., Wise, K., and Buzsáki, G. (1995). Gamma (40-100 Hz) oscillation in the hippocampus of the behaving rat. *The Journal of Neuroscience*, 15(1 Pt 1):47–60.

Brandon, M. P., Bogaard, A. R., Libby, C. P., Connerney, M. A., Gupta, K., Hasselmo, M. E., Christopher, P., Michael, A., Gupta, K., and Hasse, M. E. (2011). Reduction of Theta Rhythm Dissociates Grid Cell Spatial Periodicity from Directional Tuning Mark. *Science*, 332(6029):595–599.

Brandon, M. P., Koenig, J., Leutgeb, J. K., and Leutgeb, S. (2014). New and distinct hippocampal place codes are generated in a new environment during septal inactivation. *Neuron*, 82(4):789–796.

Brun, V. H., Leutgeb, S., Wu, H. Q., Schwarcz, R., Witter, M. P., Moser, E. I., and Moser, M. B. (2008a). Impaired Spatial Representation in CA1 after Lesion of Direct Input from Entorhinal Cortex. *Neuron*, 57(2):290–302.

Brun, V. H., Solstad, T., Kjelstrup, K. B., Fyhn, M., Witter, M. P., Moser, E. I., and Moser, M. B. (2008b). Progressive increase in grid scale from dorsal to ventral medial entorhinal cortex. *Hippocampus*, 18(12):1200–1212.

Buetfering, C., Allen, K., and Monyer, H. (2014). Parvalbumin interneurons provide grid cell-driven recurrent inhibition in the medial entorhinal cortex. *Nature Neuroscience*, 17(5):710–8.

Buhl, D. L., Harris, K. D., Hormuzdi, S. G., Monyer, H., and Buzsáki, G. (2003). Selective impairment of hippocampal gamma oscillations in connexin-36 knock-out mouse in vivo. *The Journal of Neuroscience*, 23(3):1013–1018.

Burak, Y. and Fiete, I. R. (2009). Accurate path integration in continuous attractor network models of grid cells. *PLoS Computational Biology*, 5(2).

Burgalossi, A., Herfst, L., von Heimendahl, M., F??rste, H., Haskic, K., Schmidt, M., and Brecht, M. (2011). Microcircuits of Functionally Identified Neurons in the Rat Medial Entorhinal Cortex. *Neuron*, 70(4):773–786.

Burgess, N., Barry, C., and O'Keefe, J. (2007). An oscillatory interference model of grid cell firing. *Hippocampus*, 17(9):801–812.

Buzsáki, G. and Draguhn, A. (2004). Neuronal oscillations in cortical networks. *Science*, 304(5679):1926–9.

Buzsáki, G. and Moser, E. I. (2013). Memory, navigation and theta rhythm in the hippocampal-entorhinal system. *Nature Neuroscience*, 16(2):130–138.

Buzsáki, G. and Wang, X.-J. (2012). Mechanisms of Gamma Oscillations. *Annual review of neuroscience*, (March):203–225.

Cajal, S. R. (1911). Histologie du système nerveux de l'homme et des vertébrés. *Volume 2. Paris: Maloine*, pages 891–942.

Canto, C. B. and Witter, M. P. (2012). Cellular properties of principal neurons in the rat entorhinal cortex. II. The medial entorhinal cortex. *Hippocampus*, 22(6):1277–1299.

Cardin, J. A., Carlén, M., Meletis, K., Knoblich, U., Zhang, F., Deisseroth, K., Tsai, L.-H., and Moore, C. I. (2010). Targeted optogenetic stimulation and recording of neurons in vivo using cell-type-specific expression of Channelrhodopsin-2. *Nature Protocols*, 5(2):247–254.

Carr, M. F., Jadhav, S. P., and Frank, L. M. (2011). Hippocampal replay in the awake state: a potential substrate for memory consolidation and retrieval. *Nature Neuroscience*, 14(2):147–53.

Chen, L. L., Lin, L. H., Green, E. J., Barnes, C. A., and McNaughton, B. L. (1994). Head-direction cells in the rat posterior cortex - I. anatomical distribution and behavioral modulation. *Experimental Brain Research*, 101(1):8–23.

Cho, J. and Sharp, P. E. (2001). Head direction, place, and movement correlates for cells in the rat retrosplenial cortex. *Behavioral neuroscience*, 115(1):3–25.

Chrobak, J. J. and Buzsáki, G. (1998). Gamma oscillations in the entorhinal cortex of the freely behaving rat. *The Journal of Neuroscience*, 18(1):388–98.

Ciocchi, S., Passecker, J., Malagon-Vina, H., Mikus, N., and Klausberger, T. (2015). Brain computation. Selective information routing by ventral hippocampal CA1 projection neurons. *Science*, 348(6234):560–563.

Cohen, N. J. and Squire, L. R. (1980). Preserved learning and retention of pattern-analyzing skill in amnesia: dissociation of knowing how and knowing that. *Science*, 210(4466):207–10.

Colgin, L. L., Denninger, T., Fyhn, M., Hafting, T., Bonnevie, T., Jensen, O., Moser, M.-B., and Moser, E. I. (2009). Frequency of gamma oscillations routes flow of information in the hippocampus. *Nature*, 462(7271):353–357.

Colgin, L. L., Moser, E. I., and Moser, M. B. (2008). Understanding memory through hippocampal remapping.

Condorelli, D. F., Belluardo, N., Trovato-Salinaro, A., and Mud??, G. (2000). Expression of Cx36 in mammalian neurons.

Condorelli, D. F., Parenti, R., Spinella, F., Salinaro, A. T., Belluardo, N., Cardile, V., and Cicirata, F. (1998). Cloning of a new gap junction gene (Cx36) highly expressed in mammalian brain neurons. *European Journal of Neuroscience*, 10(September 1997):1202–1208.

Connors, B. W. and Long, M. A. (2004). Electrical Synapses in the Mammalian Brain. *Annual review of neuroscience*, 27(1):393–418.

Couey, J. J., Witoelar, A., Zhang, S.-J., Zheng, K., Ye, J., Dunn, B., Czajkowski, R., Moser, M.-B., Moser, E. I., Roudi, Y., and Witter, M. P. (2013). Recurrent inhibitory circuitry as a mechanism for grid formation. *Nature Neuroscience*, 16(3):318–324.

Csicsvari, J., Hirase, H., Czurkó, A., Mamiya, A., and Buzsáki, G. (1999). Oscillatory coupling of hippocampal pyramidal cells and interneurons in the behaving Rat. *The Journal of Neuroscience*, 19(1):274–287.

Cuello, A. C., Priestley, J. V., and Sofroniew, M. V. (1983). Immunocytochemistry and neurobiology. *Quarterly journal of experimental physiology*, 68(4):545–578.

Dermietzel, R., Traub, O., Hwang, T. K., Beyer, E., Bennett, M. V., Spray, D. C., and Willecke, K. (1989). Differential expression of three gap junction proteins in developing and mature brain tissues. *Proceedings of the National Academy of Sciences*, 86(December):10148–10152.

Dhillon, A. and Jones, R. S. G. (2000). Laminar differences in recurrent excitatory transmission in the rat entorhinal cortex in vitro. *Neuroscience*, 99(3):413–422.

Domnisoru, C., Kinkhabwala, A. A., and Tank, D. W. (2013). Membrane potential dynamics of grid cells. *Nature*, 495(7440):199–204.

Dragoi, G., Carpi, D., Recce, M., Csicsvari, J., and Buzsáki, G. (1999). Interactions between hippocampus and medial septum during sharp waves and theta oscillation in the behaving rat. *The Journal of Neuroscience*, 19(14):6191–6199.

Draguhn, A., Traub, R. D., Schmitz, D., and Jefferys, J. G. (1998). Electrical coupling underlies high-frequency oscillations in the hippocampus in vitro. *Nature*, 394(6689):189–192.

Ebbesen, C. L., Reifenstein, E. T., Tang, Q., Burgalossi, A., Ray, S., Schreiber, S., Kempter, R., and Brecht, M. (2016). Cell Type-Specific Differences in Spike Timing and Spike Shape in the Rat Parasubiculum and Superficial Medial Entorhinal Cortex. *Cell Reports*, 16(4):1005–1015.

Etienne, A. S. and Jeffery, K. J. (2004). Path integration in mammals.

Fuchs, E. C., Neitz, A., Pinna, R., Melzer, S., Caputi, A., and Monyer, H. (2016). Local and Distant Input Controlling Excitation in Layer II of the Medial Entorhinal Cortex. *Neuron*, 89(1):194–208.

Fuhs, M. C. and Touretzky, D. S. (2006). A Spin Glass Model of Path Integration in Rat Medial Entorhinal Cortex. *The Journal of Neuroscience*, 26(16):4266–4276.

Fujimaru, Y. and Kosaka, T. (1996). The distribution of two calcium binding proteins, calbindin D-28K and parvalbumin, in the entorhinal cortex of the adult mouse. *Neuroscience Research*, 24(4):329–343.

Fyhn, M., Hafting, T., Treves, A., Moser, M.-B., and Moser, E. I. (2007). Hippocampal remapping and grid realignment in entorhinal cortex. *Nature*, 446(7132):190–4.

Fyhn, M., Hafting, T., Witter, M. P., Moser, E. I., and Moser, M. B. (2008). Grid cells in mice. *Hippocampus*, 18(12):1230–1238.

Fyhn, M., Molden, S., Witter, M. P., Moser, E. I., and Moser, M.-B. (2004). Spatial Representation in the Entorhinal Cortex. *Science*, 305(5688):1258–1264.

Galarreta, M. and Hestrin, S. (2001). Electrical synapses between GABA-releasing interneurons. *Nature reviews. Neuroscience*, 2(6):425–433.

Garner, H. L., Whittington, M. A., and Henderson, Z. (2005). Induction by kainate of theta frequency rhythmic activity in the rat medial septum-diagonal band complex in vitro. *Journal of Physiology*, 564(Pt 1):83–102.

Gauss, R. and Seifert, R. (2000). Pacemaker oscillations in heart and brain: a key role for hyperpolarization-activated cation channels. *Chronobiol Int*, 17(4):453–469.

Gibson, J. R., Beierlein, M., and Connors, B. W. (1999). Two networks of electrically coupled inhibitory neurons in neocortex. *Nature*, 402(6757):75–79.

Giocomo, L. M. and Hasselmo, M. E. (2009). Knock-Out of HCN1 Subunit Flattens Dorsal – Ventral Frequency Gradient of Medial Entorhinal Neurons in Adult Mice. *The Journal of Neuroscience*, 29(23):7625–7630.

Giocomo, L. M., Hussaini, S. A., Zheng, F., Kandel, E. R., Moser, M. B., and Moser, E. I. (2011). Grid cells use HCN1 channels for spatial scaling. *Cell*, 147(5):1159–1170.

Givens, B. and Olton, D. S. (1994). Local modulation of basal forebrain: effects on working and reference memory. *The Journal of Neurosciencee*, 14(6):3578–3587.

Gonzalez-Sulser, A., Parthier, D., Candela, A., McClure, C., Pastoll, H., Garden, D., Sürmeli, G., and Nolan, M. F. (2014). GABAergic projections from the medial septum selectively inhibit interneurons in the medial entorhinal cortex. *The Journal of Neuroscience*, 34(50):16739–43.

Güldenagel, M., Ammermüller, J., Feigenspan, A., Teubner, B., Degen, J., Söhl, G., Willecke, K., and Weiler, R. (2001). Visual transmission deficits in mice with targeted disruption of the gap junction gene connexin36. *The Journal of Neuroscience*, 21(16):6036–44.

Hafting, T., Fyhn, M., Bonnevie, T., Moser, M. B., and Moser, E. I. (2008). Hippocampus-independent phase precession in entorhinal grid cells. *Nature*, 453(7199):1248–1252.

Hafting, T., Fyhn, M., Molden, S., Moser, M.-B., and Moser, E. I. (2005). Microstructure of a spatial map in the entorhinal cortex. *Nature*, 436(7052):801–806.

Hales, J. B., Schlesiger, M. I., Leutgeb, J. K., Squire, L. R., Leutgeb, S., and Clark, R. E. (2014). Medial entorhinal cortex lesions only partially disrupt hippocampal place cells and hippocampus- dependent place memory. *Cell Reports*, 9(3):893–901.

Hardcastle, K., Ganguli, S., and Giocomo, L. M. (2015). Environmental Boundaries as an Error Correction Mechanism for Grid Cells. *Neuron*, 86(3):827–839.

Henze, D. a., Borhegyi, Z., Csicsvari, J., Mamiya, A., Harris, K. D., and Buzsáki, G. (2000). Intracellular features predicted by extracellular recordings in the hippocampus in vivo. *Journal of neurophysiology*, 84(1):390–400.

Hevner, R. F. and Wong-Riley, M. T. T. (1992). Entorhinal cortex of the human, monkey, and rat: Metabolic map as revealed by cytochrome oxidase. *Journal of Comparative Neurology*, 326(3):451–469.

Heys, J. G., Schultheiss, N. W., Shay, C. F., Tsuno, Y., and Hasselmo, M. E. (2012). Effects of acetylcholine on neuronal properties in entorhinal cortex. *Frontiers in behavioral neuroscience*, 6(July):32.

Hormuzdi, S. G., Pais, I., LeBeau, F. E. N., Towers, S. K., Rozov, A., Buhl, E. H., Whittington, M. A., and Monyer, H. (2001). Impaired electrical signaling disrupts gamma frequency oscillations in connexin 36-deficient mice. *Neuron*, 31(3):487–495.

Hubel, D. H. and Wiesel, T. N. (1959). Receptive fields of single neurones in the cat's striate cortex. *Journal of Physiology*, 148:574–591.

Hussaini, S. A., Kempadoo, K. A., Thuault, S. J., Siegelbaum, S. A., and Kandel, E. R. (2011). Increased Size and Stability of CA1 and CA3 Place Fields in HCN1 Knockout Mice. *Neuron*, 72(4):643–653.

Jung, M. W., Wiener, S. I., and McNaughton, B. L. (1994). Comparison of spatial firing characteristics of units in dorsal and ventral hippocampus of the rat. *The Journal of Neuroscience*, 14(12):7347–7356.

King, C., Recce, M., and O'Keefe, J. (1998). The rhythmicity of cells of the medial septum/diagonal band of Broca in the awake freely moving rat: Relationships with behaviour and hippocampal theta. *European Journal of Neuroscience*, 10(2):464–477.

Kitamura, T., Pignatelli, M., Suh, J., Kohara, K., Yoshiki, A., Abe, K., and Tonegawa, S. (2014). Island Cell Control Temporal Association Memory. *Science*, 343(6173):896–901.

Kjelstrup, K. B., Solstad, T., Brun, V. H., Hafting, T., Leutgeb, S., Witter, M. P., Moser, E. I., and Moser, M.-B. (2008). Finite Scale of Spatial Representation in the Hippocampus. *Science*, 321:2–5.

Klinkenberg, I., Sambeth, A., and Blokland, A. (2011). Acetylcholine and attention.

Koenig, J., Linder, A. N., Leutgeb, J. K., and Leutgeb, S. (2011). The spatial periodicity of grid cells is not sustained during reduced theta oscillations. *Science*, 332(6029):592–595.

Kropff, E., Carmichael, J. E., Moser, M.-B., and Moser, E. I. (2015). Speed cells in the medial entorhinal cortex. *Nature*, 523:419–424.

Kropff, E. and Treves, A. (2008). The emergence of grid cells: Intelligent design or just adaptation? *Hippocampus*, 18(12):1256–1269.

Kumar, S. S., Jin, X., Buckmaster, P. S., and Huguenard, J. R. (2007). Recurrent circuits in layer II of medial entorhinal cortex in a model of temporal lobe epilepsy. *The Journal of Neuroscience*, 27(6):1239–1246.

Kvitsiani, D., Ranade, S., Hangya, B., Taniguchi, H., Huang, J. Z., and Kepecs, A. (2013). Distinct behavioural and network correlates of two interneuron types in prefrontal cortex. *Nature*, 498(7454):363–366.

Latuske, P., Toader, O., and Allen, K. (2015). Interspike Intervals Reveal Functionally Distinct Cell Populations in the Medial Entorhinal Cortex. *The Journal of Neuroscience*, 35(31):10963–10976.

Lawson, V. H. and Bland, B. H. (1993). The role of the septohippocampal pathway in the regulation of hippocampal field activity and behavior: analysis by the intraseptal microinfusion of carbachol, atropine, and procaine.

Leutgeb, S., Leutgeb, J. K., Treves, A., Moser, M. B., and Moser, E. I. (2004). Distinct Ensemble Codes in Hippocampal Areas CA3 and CA1. *Science*, 305(5688):1295–1298.

Lu, L., Leutgeb, J. K., Tsao, A., Henriksen, E. J., Leutgeb, S., Barnes, C. a., Witter, M. P., Moser, M.-B., and Moser, E. I. (2013). Impaired hippocampal rate coding after lesions of the lateral entorhinal cortex. *Nature Neuroscience*, 16(8):1085–93.

Maaswinkel, H., Jarrard, L. E., and Whishaw, I. Q. (1999). Hippocampectomized rats are impaired in homing by path integration. *Hippocampus*, 9(5):553–561.

Maier, N., Güldenagel, M., Söhl, G., Siegmund, H., Willecke, K., and Draguhn, A. (2002). Reduction of high-frequency network oscillations (ripples) and pathological network discharges in hippocampal slices from connexin 36-deficient mice. *The Journal of Physiology*, 541(Pt 2):521–528.

Majewski, L. and Kuznicki, J. (2014). SOCE in neurons: Signaling or just refilling?

Mathis, A., Herz, A. V. M., and Stemmler, M. (2012). Optimal Population Codes for Space: Grid Cells Outperform Place Cells. *Neural Computation*, 24(9):2280–317.

Maurer, A. P., VanRhoads, S. R., Sutherland, G. R., Lipa, P., and McNaughton, B. L. (2005). Self-motion and the origin of differential spatial scaling along the septo-temporal axis of the hippocampus. *Hippocampus*, 15(7):841–852.

McNaughton, B. L., Barnes, C. A., and O'Keefe, J. (1983). The contributions of position, direction, and velocity to single unit activity in the hippocampus of freely-moving rats. *Experimental Brain Research*, 52(1):41–49.

McNaughton, B. L., Battaglia, F. P., Jensen, O., Moser, E. I., and Moser, M.-B. (2006). Path integration and the neural basis of the 'cognitive map'. *Nature Reviews Neuroscience*, 7(8):663–678.

Meyer, A. H., Katona, I., Blatow, M., Rozov, A., and Monyer, H. (2002). In vivo labeling of parvalbumin-positive interneurons and analysis of electrical coupling in identified neurons. *The Journal of Neuroscience*, 22(16):7055–7064.

Milner, B. (1965). Visually-guided maze learning in man: Effects of bilateral hippocampal, bilateral frontal, and unilateral cerebral lesions. *Neuropsychologia*, 3(4):317–338.

Mitchell, S. J., Rawlins, J. N., Steward, O., and Olton, D. S. (1982). Medial septal area lesions disrupt theta rhythm and cholinergic staining in medial entorhinal cortex and produce impaired radial arm maze behavior in rats. *The Journal of Neuroscience*, 2(3):292–302.

Mittelstaedt, M. L. and Mittelstaedt, H. (1980). Homing by path integration in a mammal. *Naturwissenschaften*, 67(11):566–567.

Mizuseki, K., Sirota, A., Pastalkova, E., and Buzsáki, G. (2009). Theta Oscillations Provide Temporal Windows for Local Circuit Computation in the Entorhinal-Hippocampal Loop. *Neuron*, 64(2):267–280.

Morris, N. P., Harris, S. J., and Henderson, Z. (1999). Parvalbumin-immunoreactive, fast-spiking neurons in the medial septum/diagonal band complex of the rat: Intracellular recordings in vitro. *Neuroscience*, 92(2):589–600.

Morris, R. G. M., Schenk, F., Tweedie, F., and Jarrard, L. E. (1990). Ibotenate lesions of hippocampus and/or subiculum: Dissociating components of allocentric spatial learning. *European Journal of Neuroscience*, 2(12):1016–1028.

Moser, E. I., Kropff, E., and Moser, M.-B. (2008). Place cells, grid cells, and the brain's spatial representation system. *Annual review of neuroscience*, 31:69–89.

Mountcastle, V. B. (1997). The columnar organization of the neocortex.

Muller, R. U., Kubie, J. L., and Ranck, J. B. (1987). Spatial firing patterns of hippocampal complex-spike cells in a fixed environment. *The Journal of Neuroscience*, 7(7):1935–1950.

Muñoz, W., Tremblay, R., and Rudy, B. (2014). Channelrhodopsin-Assisted Patching: InVivo Recording of Genetically and Morphologically Identified Neurons throughout the Brain. *Cell Reports*, 9(6):2304–2316.

Nadarajah, B., Jones, A. M., Evans, W. H., and Parnavelas, J. G. (1997). Differential expression of connexins during neocortical development and neuronal circuit formation. *The Journal of Neuroscience*, 17(9):3096–3111.

Naumann, R. K., Ray, S., Prokop, S., Las, L., Heppner, F. L., and Brecht, M. (2016). Conserved size and periodicity of pyramidal patches in layer 2 of medial/caudal entorhinal cortex. *Journal of Comparative Neurology*, 524(4):783–806.

Navratilova, Z. and McNaughton, B. L. (2014). Models of Path Integration in the Hippocampal Complex. In *Space,Time and Memory in the Hippocampal Formation*, pages 191–224. Springer Vienna, Vienna.

Nolan, M. F., Malleret, G., Lee, K. H., Gibbs, E., Dudman, J. T., Santoro, B., Yin, D., Thompson, R. F., Siegelbaum, S. A., Kandel, E. R., and Morozov, A. (2003). The Hyperpolarization-Activated HCN1 Channel Is Important for Motor Learning and Neuronal Integration by Cerebellar Purkinje Cells. *Cell*, 115(5):551–564.

Notomi, T. and Shigemoto, R. (2004). Immunohistochemical Localization of Ih Channel Subunits, HCN1-4, in the Rat Brain. *Journal of Comparative Neurology*, 471(3):241–276.

O'Keefe, J. and Burgess, N. (2005). Dual phase and rate coding in hippocampal place cells: Theoretical significance and relationship to entorhinal grid cells. *Hippocampus*, 15(7):853–866.

O'Keefe, J. and Dostrovsky, J. (1971). The hippocampus as a spatial map. Preliminary evidence from unit activity in the freely-moving rat. *Brain Research*, 34(1):171–175.

O'Keefe, J. and Nadel, L. (1987). *The Hippocampus as a Cognitive Map*. Oxford University Press, Oxford.

O'Keefe, J. and Speakman, A. (1987). Single unit activity in the rat hippocampus during a spatial memory task. *Experimental brain research. Experimentelle Hirnforschung. Experimentation cerebrale*, 68(1):1–27.

Parron, C., Poucet, B., and Save, E. (2006). Cooperation between the hippocampus and the entorhinal cortex in spatial memory: A disconnection study. *Behavioural Brain Research*, 170(1):99–109.

Parron, C. and Save, E. (2004). Evidence for entorhinal and parietal cortices involvement in path integration in the rat. *Experimental Brain Research*, 159(3):349–359.

Pastoll, H., Ramsden, H. L., and Nolan, M. F. (2012). Intrinsic electrophysiological properties of entorhinal cortex stellate cells and their contribution to grid cell firing fields. *Frontiers in Neural Circuits*, 6(April):1–21.

Pastoll, H., Solanka, L., van Rossum, M. C. W., and Nolan, M. F. (2013). Feedback Inhibition Enables Theta-Nested Gamma Oscillations and Grid Firing Fields. *Neuron*, 77(1):141–154.

Petrides, M. (1985). Deficits on Conditional Associative-Learning Tasks After Frontal-and Temporal-Lobe Lesions in Man. *Neuropsychologia*, 23(5):601–614.

Quilichini, P., Sirota, A., and Buzsáki, G. (2010). Intrinsic circuit organization and theta-gamma oscillation dynamics in the entorhinal cortex of the rat. *The Journal of Neuroscience*, 30(33):11128–42.

Ray, S., Naumann, R., Burgalossi, A., Tang, Q., Schmidt, H., and Brecht, M. (2014). Grid-Layout and Theta-Modulation of Layer 2 Pyramidal Neurons in Medial Entorhinal Cortex. *Science*, 13(8):987–94.

Reisel, D., Bannerman, D. M., Schmitt, W. B., Deacon, R. M. J., Flint, J., Borchardt, T., Seeburg, P. H., and Rawlins, J. N. P. (2002). Spatial memory dissociations in mice lacking GluR1. *Nature neuroscience*, 5(9):868–873.

Resnik, E., McFarland, J. M., Sprengel, R., Sakmann, B., and Mehta, M. R. (2012). The effects of GluA1 deletion on the hippocampal population code for position. *The Journal of Neuroscience*, 32(26):8952–68.

Santoro, B., Chen, S., Luthi, A., Pavlidis, P., Shumyatsky, G. P., Tibbs, G. R., and Siegelbaum, S. a. (2000). Molecular and functional heterogeneity of hyperpolarization-activated pacemaker channels in the mouse CNS. *The Journal of Neuroscience*, 20(14):5264–5275.

Sargolini, F., Fyhn, M., Hafting, T., McNaughton, B. B. L., Witter, M. P., Moser, M.-B., and Moser, E. I. (2006). Conjunctive Representation of Position, Direction, and Velocity in Entorhinal Cortex. *Science*, 312:758–763.

Schlesiger, M. I., Cannova, C. C., Boublil, B. L., Hales, J. B., Mankin, E. A., Brandon, M. P., Leutgeb, J. K., Leibold, C., and Leutgeb, S. (2015). The medial entorhinal cortex is necessary for temporal organization of hippocampal neuronal activity. *Nature Neuroscience*, 18(8):1123–1132.

Schmidt-Hieber, C. and Häusser, M. (2013). Cellular mechanisms of spatial navigation in the medial entorhinal cortex. *Nature Neuroscience*, 16(3):325–31.

Scoville, W. B. and Milner, B. (1957). Loss of recent memory after bilateral hippocampal lesions. *Journal of Neurology, Neurosurgery & Psychiatry*, 20(11).

Senior, T. J., Huxter, J. R., Allen, K., O'Neill, J., and Csicsvari, J. (2008). Gamma oscillatory firing reveals distinct populations of pyramidal cells in the CA1 region of the hippocampus. *The Journal of Neuroscience*, 28(9):2274–86.

Sharp, P. E., Blair, H. T., and Cho, J. (2001). The anatomical and computational basis of the rat head-direction cell signal.

Singer, W. and Gray, C. (1995). Visual feature integration and the temporal correlation hypothesis. *Annual review of neuroscience*, 18:555–586.

Skaggs, W. E. and McNaughton, B. L. (1996). Replay of neuronal firing sequences in rat hippocampus during sleep following spatial experience. *Science*, 271(5257):1870–1873.

Skaggs, W. E., McNaughton, B. L., Wilson, M. A., and Barnes, C. A. (1996). Theta phase precession in hippocampal neuronal populations and the compression of temporal sequences. *Hippocampus*, 6(2):149–172.

Solanka, L., van Rossum, M. C. W., and Nolan, M. F. (2015). Noise promotes independent control of gamma oscillations and grid firing within recurrent attractor networks. *eLife*, 4:e06444.

Solstad, T., Solstad, T., Boccara, C. N., Boccara, C. N., Kropff, E., Kropff, E., Moser, M.-B., Moser, M.-B., Moser, E. I., and Moser, E. I. (2008). Representation of Geometric Borders in the Entorhinal Cortex. *Science*, 322:17–20.

Sommer, S. and Wehner, R. (2004). The ant's estimation of distance travelled: Experiments with desert ants, Cataglyphis fortis. *Journal of Comparative Physiology*, 190(1):1–6.

Stackman, R. W. and Taube, J. S. (1998). Firing properties of rat lateral mammillary single units: head direction, head pitch, and angular head velocity. *The Journal of Neuroscience*, 18(21):9020–37.

Steffenach, H. A., Witter, M., Moser, M. B., and Moser, E. I. (2005). Spatial memory in the rat requires the dorsolateral band of the entorhinal cortex. *Neuron*, 45(2):301–313.

Stensola, H., Stensola, T., Solstad, T., Frøland, K., Moser, M.-B., and Moser, E. I. (2012). The entorhinal grid map is discretized. *Nature*, 492:72–8.

Sun, C., Kitamura, T., Yamamoto, J., Martin, J., Pignatelli, M., Kitch, L. J., Schnitzer, M. J., and Tonegawa, S. (2015). Distinct speed dependence of entorhinal island and ocean cells, including respective grid cells. *Proceedings of the National Academy of Sciences*, 112(30):9466–9471.

Sürmeli, G., Marcu, D. C., McClure, C., Garden, D. L. F., Pastoll, H., and Nolan, M. F. (2015). Molecularly Defined Circuitry Reveals Input-Output Segregation in Deep Layers of the Medial Entorhinal Cortex. *Neuron*, 88(5):1040–1053.

Tamamaki, N., Yanagawa, Y., Tomioka, R., Miyazaki, J. I., Obata, K., and Kaneko, T. (2003). Green Fluorescent Protein Expression and Colocalization with Calretinin, Parvalbumin, and Somatostatin in the GAD67-GFP Knock-In Mouse. *Journal of Comparative Neurology*, 467(1):60–79.

Tang, Q., Burgalossi, A., Ebbesen, C. L., Ray, S., Naumann, R., Schmidt, H., Spicher, D., and Brecht, M. (2014). Pyramidal and stellate cell specificity of grid and border representations in layer 2 of medial entorhinal cortex. *Neuron*, 84(6):1191–1197.

Taube, J. S., Muller, R. U., and Ranck, J. B. (1990a). Head-direction cells recorded from the postsubiculum in freely moving rats. I. Description and quantitative analysis. *The Journal of Neuroscience*, 10(2):420–435.

Taube, J. S., Muller, R. U., and Ranck, J. B. (1990b). Head-direction cells recorded from the postsubiculum in freely moving rats. II. Effects of environmental manipulations. *The Journal of Neuroscience*, 10(2):436–447.

Touretzky, D. S. and Redish, A. D. (1996). Theory of rodent navigation based on interacting representations of space. *Hippocampus*, 6(3):247–270.

Traub, R. D., Draguhn, A., Whittington, M. a., Baldeweg, T., Bibbig, A., Buhl, E. H., and Schmitz, D. (2002). Axonal gap junctions between principal neurons: a novel source of network oscillations, and perhaps epileptogenesis. *Reviews in the neurosciences*, 13(1):1–30.

Traub, R. D., Pais, I., Bibbig, A., LeBeau, F. E. N., Buhl, E. H., Hormuzdi, S. G., Monyer, H., and Whittington, M. a. (2003). Contrasting roles of axonal (pyramidal cell) and dendritic (interneuron) electrical coupling in the generation of neuronal network oscillations. *Proceedings of the National Academy of Sciences*, 100(3):1370–1374.

Tsanov, M., Chah, E., Vann, S. D., Reilly, R. B., Erichsen, J. T., Aggleton, J. P., and O'Mara, S. M. (2011). Theta-modulated head direction cells in the rat anterior thalamus. *The Journal of Neuroscience*, 31(26):9489–502.

Valerio, S. and Taube, J. S. (2016). Head Direction Cell Activity Is Absent in Mice without the Horizontal Semicircular Canals. *The Journal of Neuroscience*, 36(3):741–754.

Van Cauter, T., Camon, J., Alvernhe, A., Elduayen, C., Sargolini, F., and Save, E. (2013). Distinct roles of medial and lateral entorhinal cortex in spatial cognition. *Cerebral cortex*, 23(2):451–9.

van Strien, N. M., Cappaert, N. L. M., and Witter, M. P. (2009). The anatomy of memory: an interactive overview of the parahippocampal-hippocampal network. *Nature reviews. Neuroscience*, 10(4):272–82.

Vandecasteele, M., Varga, V., Berényi, A., Papp, E., Barthó, P., Venance, L., Freund, T. F., and Buzsáki, G. (2014). Optogenetic activation of septal cholinergic neurons suppresses sharp wave ripples and enhances theta oscillations in the hippocampus. *Proceedings of the National Academy of Sciences*, 111(37):13535–13540.

Varga, C., Lee, S. Y., and Soltesz, I. (2010). Target-selective GABAergic control of entorhinal cortex output. *Nature Neuroscience*, 13(7):822–824.

Varga, V., Hangya, B., Kránitz, K., Ludányi, A., Zemankovics, R., Katona, I., Shigemoto, R., Freund, T. F., and Borhegyi, Z. (2008). The presence of pacemaker HCN channels identifies theta rhythmic GABAergic neurons in the medial septum. *The Journal of physiology*, 586(16):3893–3915.

Venance, L., Rozov, A., Blatow, M., Burnashev, N., Feldmeyer, D., and Monyer, H. (2000). Connexin expression in electrically coupled postnatal rat brain neurons. *Proceedings of the National Academy of Sciences*, 97(18):10260–10265.

Verkhratsky, A. (2002). The endoplasmic reticulum and neuronal calcium signalling. *Cell Calcium*, 32(5-6):393–404.

Vinogradova, O. S. (1995). Expression, control, and probable functional significance of the neuronal theta-rhythm.

Whishaw, I. Q. and Maaswinkel, H. (1998). Rats with fimbria-fornix lesions are impaired in path integration: A role for the hippocampus in "sense of direction". *The Journal of Neuroscience*, 18(8):3050–3058.

Whittington, M. a., Traub, R. D., and Jefferys, J. G. (1995). Synchronized oscillations in interneuron networks driven by metabotropic glutamate receptor activation.

Winter, S. S., Clark, B. J., and Taube, J. S. (2015). Disruption of the head direction cell network impairs the parahippocampal grid cell signal. *Science*, 347(6224):870–4.

Wittlinger, M., Wolf, H., and Wehner, R. (2007). Hair plate mechanoreceptors associated with body segments are not necessary for three-dimensional path integration in desert ants, Cataglyphis fortis. *The Journal of Experimental Biology*, 210(Pt 3):375–82.

Woolsey, T. A. and Van der Loos, H. (1970). The structural organization of layer IV in the somatosensory region (S I) of mouse cerebral cortex. The description of a cortical field composed of discrete cytoarchitectonic units. *Brain Research*, 17(2):205–242.

Yartsev, M. M., Witter, M. P., and Ulanovsky, N. (2011). Grid cells without theta oscillations in the entorhinal cortex of bats. *Nature*, 479(7371):103–107.

Yasuda, M. and Mayford, M. R. (2006). CaMKII Activation in the Entorhinal Cortex Disrupts Previously Encoded Spatial Memory. *Neuron*, 50(2):309–318.

Zamanillo, D., Sprengel, R., Hvalby, O., Jensen, V., Burnashev, N., Rozov, A., Kaiser, K. M., Köster, H. J., Borchardt, T., Worley, P., Lübke, J., Frotscher, M., Kelly, P. H., Sommer, B., Andersen, P., Seeburg, P. H., and Sakmann, B. (1999). Importance of AMPA receptors for hippocampal synaptic plasticity but not for spatial learning. *Science*, 284(5421):1805–1811.

Zhang, S.-J., Ye, J., Miao, C., Tsao, A., Cerniauskas, I., Ledergerber, D., Moser, M.-B., and Moser, E. I. (2013). Optogenetic Dissection of Entorhinal-Hippocampal Functional Connectivity. *Science*, 340(6128):1232627–1232627.

Ziv, Y., Burns, L. D., Cocker, E. D., Hamel, E. O., Ghosh, K. K., Kitch, L. J., El Gamal, A., and Schnitzer, M. J. (2013). Long-term dynamics of CA1 hippocampal place codes. *Nature Neuroscience*, 16(3):264–6.

List of Abbreviations

AB antibody

AMPA α-amino-3-hydroxy-5-methyl-4-isoxazolepropionic acid

ATN anterior thalamic nuclei

BSA bovine serum albumin

CB Calbindin

ChR2 Channelrhodopsin-2

Cx36 connexin 36

CA1 Cornu Ammonis region 1

DAPI 4',6-diamidin-2-phenylindol

EGFP enhanced green fluorescent protein

FS fast-spiking

$GABA_AR$ γ-aminobutyric acid receptor type A

GluA1 glutamate receptor 1

HCN hyperpolarization-activated cyclic nucleotide-gated

HD head direction

KO knock-out

LII Layer II

LFP local field potential

MEC medial entorhinal cortex

MS medial septum

MSDB medial septum and the vertical limb of the diagonal band of Broca

PFA paraformaldehyde

PaS parasubiculum

PV parvalbumin

PBS phosphate buffered saline

RE Reelin

SEM standard error of the mean

SOM somatostatin

Wfs1 Wolfram syndrome 1

WT wild-type

AMPA α-amino-3-hydroxy-5-methyl-4-isoxazolepropionic acid

GABA γ-aminobutyric acid

List of Figures

Appendix

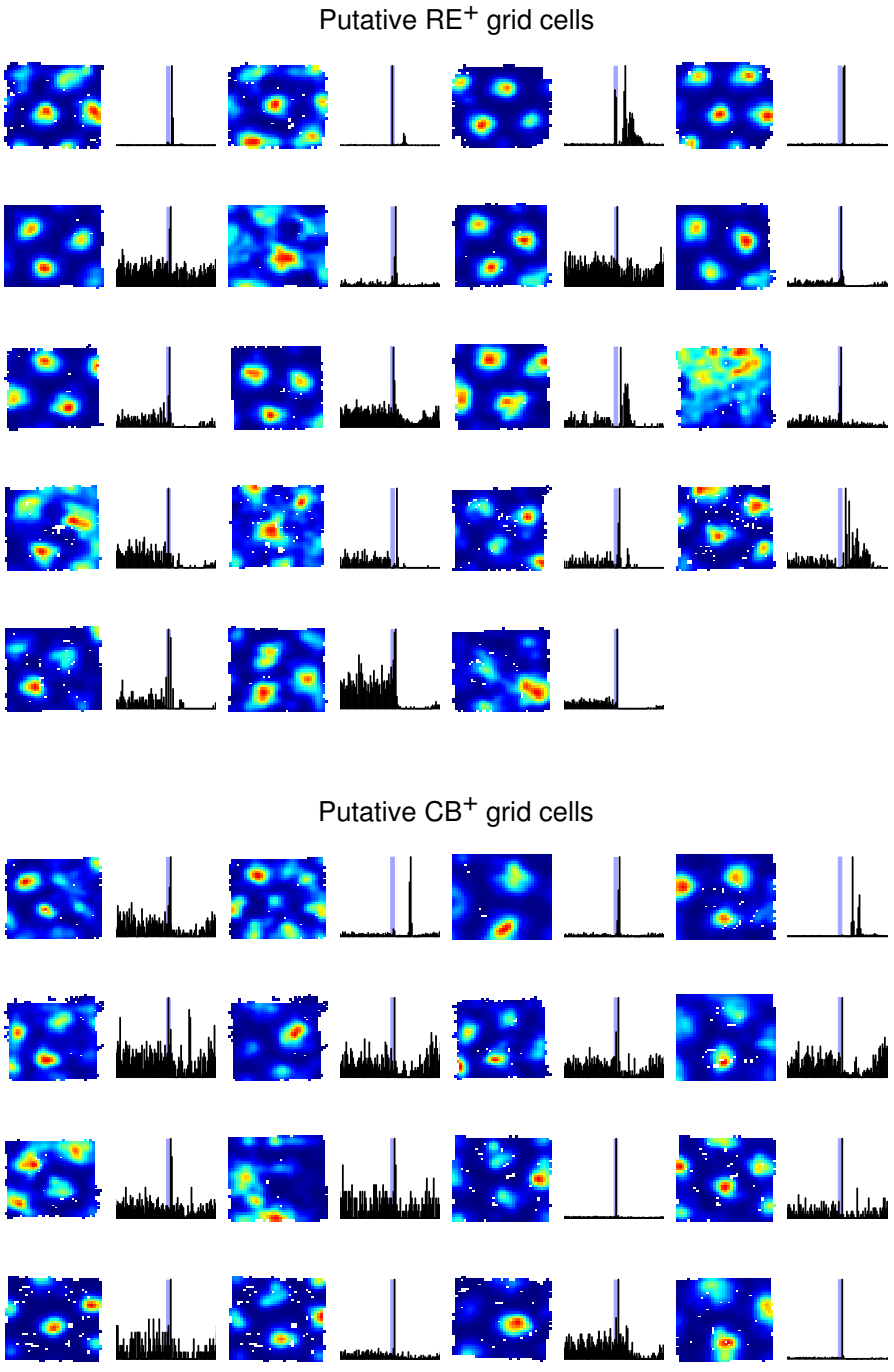

Figure 19. All grid cells directly activated through laser stimulation. Firing rate maps and corresponding laser cross-correlations.

List of publications

Toader, O., Gil, M.„ Neitz, A., Allen, K., and Monyer, H. Intact spatial coding in the medial entorhinal cortex of mice with impaired hippocampal function. *In revision* at Journal of Neuroscience

Latuske, P., **Toader, O.**, and Allen, K. (2015). Interspike Intervals Reveal Functionally Distinct Cell Populations in the Medial Entorhinal Cortex. Journal of Neuroscience, 35(31):10963–10976.

Allen, K., Gil, M., Resnik, E., **Toader, O.**, Seeburg, P., and Monyer, H. (2014). Impaired Path Integration and Grid Cell Spatial Periodicity in Mice Lacking GluA1-Containing AMPA Receptors. The Journal of Neuroscience, 34(18):6245–59.